THE UNIVERSITY *of* EDINBURGH

Probing SMM behaviour in Heterometallic 3/4*d*-4*f* Complexes

Robbie McNab

A Thesis Submitted for the Degree of Doctor of Philosophy

School of Chemistry

Faculty of Science and Engineering

The University of Edinburgh

September 2019

Abstract

In recent years the field of molecular magnetism has focused its attention on creating novel magnetic molecules that can retain their magnetisation in the absence of a magnetic field, below a blocking temperature. These complexes are known as Single-Molecule Magnets (SMMs). Initial focus on the use of transition metal ions swiftly moved on to lanthanide metal ions on account of their larger anisotropies and larger spin values. The latter have now shown barriers to magnetization reversal far superior to the former. Recent studies have proved that coordination chemistry and structural modification can be exploited to manipulate magnetic properties of Ln species to maximise energy barrier heights and minimising under barrier relaxation processes such as Quantum Tunnelling of the Magnetisation (QTM). QTM, which represents a loss of magnetisation through degenerate Ms levels, is a limiting factor in designing Ln containing SMMs with larger barriers to magnetisation reversal.

The complexity of the energy level spectrum of individual Ln ions is further convoluted by the addition of exchange interactions between neighbouring metals. These create low lying excited states which are easily accessible from the ground state, and result in thermally activated QTM (TA-QTM). Extensive research in the field has shown that these problems can be overcome and the SMM properties can be optimised with careful modification of the geometry of the lanthanide ions, the topology of the molecule and the nature of the exchange interactions. However, even with these recent insights it remains a challenge to correlate magnetic behaviour with structural properties.

Each chapter of this thesis aims to elucidate the correlation between the structure and magnetic properties of novel lanthanide containing molecular systems exploiting the pro-ligands 2-(hydroxymethyl)pyridine (hmpH) and 6-methyl-2-(hydroxymethyl)pyridine (mhmpH).

Chapter 2 describes the structural and magnetic studies of six analogous, highly symmetric triangle-in-triangle 3*d*-4*f* molecules with general formula $[Ni^{II}_3Ln^{III}_3(hmp)_{12}](ClO_4)_3 \cdot 3MeCN$ (where Ln = Gd, Tb, Dy, Ho, Er, Y). Magnetic susceptibility measurements reveal that they do not act as SMMs. Fitting of experimental susceptibility data for the $[Ni_3Gd_3]$ analogue afforded J_{GdGd} = -0.02 cm^{-1} and J_{GdNi} = -0.32 cm^{-1}; the antiferromagnetic exchange interactions leading to a vast increase in the number of potential relaxation pathways through the presence of low-lying excited states.

Chapter 3 describes the structural and magnetic studies of two structurally similar, butterfly-like molecules, namely $[M^{II}_2Ln^{III}_2(hmp)_6(NO_3)_4(MeCN)_2]\cdot MeOH$ (*BF1*) and $[M^{II}_2Ln^{III}_2(mhmp)_6(NO_3)_4]\cdot MeCN$ (*BF2*); where M = Ni, Zn; Ln = Gd, Tb, Dy, Y; hmpH = 2-(hydroxymethyl)pyridine and mhmpH = 6-methyl-2-pyridinemethanol. The subtle changes in the molecular structure and lanthanide geometry results in a change in the 3*d*-4*f* exchange interaction which in turn affect the SMM properties. Fitting of the susceptibility data of the $[Ni_2Gd_2]$ complex afforded J_{NiNi} = 1.09 cm^{-1} and J_{NiLn} = 0.7325 cm^{-1} for *BF1* and J_{NiNi} = -0.32 cm^{-1} and J_{NiLn} = 0.52 cm^{-1} for *BF2*. The $[Zn_2Dy_2]$ analogue of *BF1* and *BF2* exhibits SMM behaviour with U_{eff} = 38.58 cm^{-1} and 72.45 cm^{-1}, respectively. The $[Ni_2Dy_2]$ analogue of *BF2* possesses a U_{eff} = 11.96 cm^{-1} whereas the analogue in *BF1* displays no SMM behaviour. The improvement in SMM behaviour in *BF2* is due to the improvement of single-ion behaviour of the lanthanide ions, paired with a weaker J_{NiLn} value.

Chapter 4 describes the structural and magnetic studies of the heptanuclear disc-like structure $[Cd^{II}_4(Dy^{III}_{(3-n)}Y^{III}_n)(hmp)_{12}(NO_3)_3](ClO_4)_2\cdot 3MeCN$ (where n = 0, 1, 2 or 3), in which the diamagnetic Cd^{II} act as a spacer between the Dy^{III} ions thereby removing J_{DyDy} interactions. The $[Cd_4Dy_3]$ analogue shows a U_{eff} = 295.87 cm^{-1} and butterfly hysteresis loops at $T \gtrapprox 2$ K. Simulation of the experimental data shows that J_{DyDy} (J_{total}) = -0.13 cm^{-1}. Site dilution (replacing paramagnetic Dy^{III} with diamagnetic Y^{III}) further decreases the J_{DyDy} interactions, increasing the coercivity of the hysteresis loops by decreasing QTM and TA-QTM processes.

Lay Summary

The projects described in this thesis aim to combine magnetically interesting positively charged building blocks with negatively charged building blocks that can link these blocks together. The positively charged building blocks are metals, some of which have unpaired electrons which makes them magnetic and this behaviour depends in part on which metals they are, their orientation and their environment. These building blocks combine to create discrete structures that will have distinct magnetic behaviour, influenced by the composition and shape of the structure. The metal building blocks can influence each other's magnetic behaviour depending on their proximity to one another and how they are connected. By creating a number of these discrete structures we can begin to understand and modify them to create magnetic systems that can be used in real world applications.

Table of Contents

Acknowledgements

An immeasurable debt of gratitude to my parents, Debbie and Alan, for supporting me through my whole university career. It has been a long road and I will be forever grateful.

Huge thanks to Effie for supporting me in my final year where I had to finish writing up my thesis and complete my PGDE.

Big thanks to Ross for giving me the opportunity to work in his group and carry out the research. To both Ross and Euan for their continued support throughout the PhD. Thank you to the whole Brechin group throughout the years for their help and fruitful discussion. Special thanks to Hector for keeping me (in)sane throughout the years, providing support sandwiched between quality roasts. His giraffe like stature combined with his navigational skills made him the perfect tour guide on our trips to Japan and Copenhagen/Malmo. Thank you also to Anders, the three of us had a great time in Japan.

I am very grateful to Gary Nichol for the crystallography service and going beyond to help me refine my crystallographic knowledge and allowing me to occasionally use his diffractometer.

Thank you to the SQUID for not completely dying on us and allowing me to get some good data before I finished.

Declaration

I hereby declare that except where specific reference is made to other sources, the work contained in this thesis is the original work of the author. It has been composed by the candidate and has not been submitted, in whole or in part, for any other degree, diploma, or qualification.

Robbie McNab

List of Complexes

The following table provides a quick reference for all complexes presented in the thesis per chapter. Solvent molecules of crystallisation have been removed for clarity.

Chapter	Number	Complex
2	**1**	$[Ni^{II}_3Gd^{III}_3(hmp)_{12}](ClO_4)_3$
2	**2**	$[Ni^{II}_3Tb^{III}_3(hmp)_{12}](ClO_4)_3$
2	**3**	$[Ni^{II}_3Dy^{III}_3(hmp)_{12}](ClO_4)_3$
2	**4**	$[Ni^{II}_3Ho^{III}_3(hmp)_{12}](ClO_4)_3$
2	**5**	$[Ni^{II}_3Er^{III}_3(hmp)_{12}](ClO_4)_3$
2	**6**	$[Ni^{II}_3Y^{III}_3(hmp)_{12}](ClO_4)_3$
3	**1**	$[Ni^{II}_2Gd^{III}_2(hmp)_6(NO_3)_4(MeCN)_2]$
3	**2**	$[Ni^{II}_2Tb^{III}_2(hmp)_6(NO_3)_4(MeCN)_2]$
3	**3**	$[Ni^{II}_2Dy^{III}_2(hmp)_6(NO_3)_4(MeCN)_2]$
3	**4**	$[Ni^{II}_2Y^{III}_2(hmp)_6(NO_3)_4(MeCN)_2]$
3	**5**	$[Zn^{II}_2Gd^{III}_2(hmp)_6(NO_3)_4(MeCN)_2]$
3	**6**	$[Zn^{II}_2Tb^{III}_2(hmp)_6(NO_3)_4(MeCN)_2]$
3	**7**	$[Zn^{II}_2Dy^{III}_2(hmp)_6(NO_3)_4(MeCN)_2]$
3	**8**	$[Ni^{II}_2Gd^{III}_2(mhmp)_6(NO_3)_4]$
3	**9**	$[Ni^{II}_2Dy^{III}_2(mhmp)_6(NO_3)_4]$
3	**10**	$[Ni^{II}_2Y^{III}_2(mhmp)_6(NO_3)_4]$
3	**11**	$[Zn^{II}_2Dy^{III}_2(mhmp)_6(NO_3)_4]$
4	**1**	$[Cd^{II}_4Dy^{III}_3(hmp)_{12}(NO_3)_3](ClO_4)_2$
4	**2**	$[Cd^{II}_4Dy^{III}_2Y^{III}(hmp)_{12}(NO_3)_3](ClO_4)_2$
4	**3**	$[Cd^{II}_4Dy^{III}Y^{III}_2(hmp)_{12}(NO_3)_3](ClO_4)_2$
4	**4**	$[Cd^{II}_4Y^{III}_3(hmp)_{12}(NO_3)_3](ClO_4)_2$

External Contributors

Ab initio computational analysis: Gopalan Rajaraman

Conferences Attended

2018

4th Annual Joseph Black Conference, The University of Edinburgh, UK – 26th May 2018

Participation: Oral Presentation

2017

4th EuCheMS Inorganic Chemistry Conference (EICC), Copenhagen, Denmark – 2nd-5th July 2017

Participation: Poster Presentation

Universities of Scotland Inorganic Conference (USIC), University of St Andrews, UK – 29th and 30th August 2017

Participation: Poster Presentation

3rd Annual Joseph Black Conference, The University of Edinburgh, UK – 26th May 2017

Participation: Poster Presentation

2016

15th International Conference on Molecule-Based Magnets (ICMM), Sendai, Japan – 4th-8th September 2016

Participation: Poster Presentation

Universities of Scotland Inorganic Conference (USIC), University of Strathclyde, UK – 11th and 12th August 2016

Participation: Poster Presentation

2nd Annual Joseph Black Conference, The University of Edinburgh, UK – 26th May 2016

Participation: Poster Presentation

Abbreviatetions

BF1 = butterfly 1

BF2 = butterfly 2

D = Zero field splitting parameter

g = g-factor

J = Total angular momentum

K_b = Boltzmann constant

L = Orbital angular momentum

Ln = lanthanide

QTM = quantum tunnelling of magnetisation

S = Spin angular momentum

SIM = single ion magnet

SMM = single molecule magnet

TA-QTM = thermally activated quantum tunnelling of magnetisation

TM = transition metal

U = energy barrier

U_{eff} = effective energy barrier

Chapter 1: Introduction

This thesis investigates a number of heterometallic, lanthanide-based single molecule magnet systems and aims to analyse their magnetic properties and make correlations between their magnetic behaviour and molecular structure. The theory of magnetism relevant in both transition metal and lanthanide containing compounds is examined in the following introduction with pertinent examples preceding discussion of the systems investigated in this thesis.

1.1 Molecular magnetism

Molecular magnetism has been a prosperous field for a number of decades, with potential in developing wide ranging applications that could expand our technological capabilities.[1] Molecular magnetism is the study of the magnetic properties of molecular systems that contain ions with unpaired electrons. Molecule based magnets have the intrinsic value of being many orders of magnitude smaller than conventional bulk magnets. The field has expanded into a number of sub-disciplines encompassing a variety of interesting magnetic phenomena, including magnetic refrigeration, quantum computing, spintronics, data storage, and even biomedical application such as MRI contrast agents.[2-8] This multidisciplinary approach requires a breadth of expertise (and collaboration) to synthesise and fully characterise novel physical properties, since the field straddles the border between organic, inorganic, physical and theoretical chemistry, materials science and condensed matter physics. Historically the major focus has been on homometallic molecules containing 3*d* metals but has more recently expanded to the study of 4*d*, 5*d*, 4*f* and 5*f* metals, including heterometallic complexes thereof.[9-12]

1.1.2 Single-Molecule Magnets

Molecules that retain their magnetisation in zero field are known as single-molecule magnets (SMMs). If magnetisation is retained on a molecular level, these systems can be used as a means of storing data, with potential to increase data storage density by several orders of magnitude. Conventional silicon based data storage systems are approaching the limit of classical mechanics as they are becoming small enough to be perturbed by quantum effects such as quantum tunnelling of magnetisation (QTM). [13-18] Therefore, it will be necessary to switch to molecule based systems where QTM can be controlled/manipulated by molecular chemistry.

The understanding of these systems began in the early 1990s with the discovery of the archetypal SMM, $[Mn^{IV}_4Mn^{III}_8O_{12}(O_2CR)_{16}(H_2O)_4]$, also known as Mn_{12} (**figure 1** shows the

benzoate derivative).[19-26] The original acetate derivative, $[Mn^{IV}_4Mn^{III}_8O_{12}(O_2CCH_3)_{16}(H_2O)_4]$, was shown through SQUID magnetometry and high-frequency electron paramagnetic resonance (HFEPR) spectroscopy, to have an S = 10 ground state arising from the antiferromagnetic interactions between the four Mn^{IV} ions (each with S = 3/2) and the eight Mn^{III} ions (each with S = 2), possessing an axial zero-field splitting parameter (D) of -0.5 cm^{-1}.[27] Through careful analysis of the Mn_{12} system a model of the mechanism of the retention/relaxation of magnetisation was realised. It was discovered that the requirement of systems to exhibit these properties was the combination of a large (or non-zero) total spin number S and a large and negative axial zero-field splitting of that S state; with the barrier to magnetization reversal being $S^2|D|$ and $(S^2\text{-}1/4)|D|$ for integer and half-integer spin states, respectively.

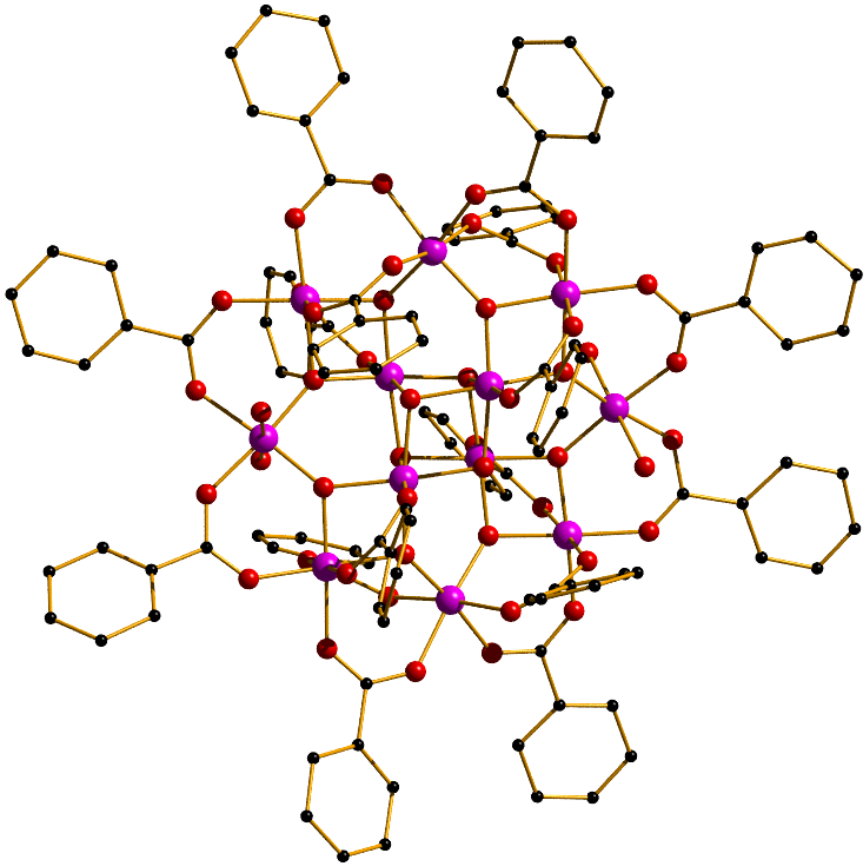

Figure 1 Structure of the benzoate derivative of Mn_{12}, $[Mn^{IV}_4Mn^{III}_8O_{12}(O_2CPh)_{16}(H_2O)_4]$. Colour scheme: Mn, pink; O, red; C, black (hydrogen atoms removed for clarity).[27]

When *D* is negative, the 2*S*+1 M_s levels are split such that the largest M_s levels are lowest in energy, and the smallest M_s levels highest in energy. This creates a barrier (*U*) between the ±*S* states (*i.e.* 'spin-up' and 'spin-down') (**fig**. **2**).

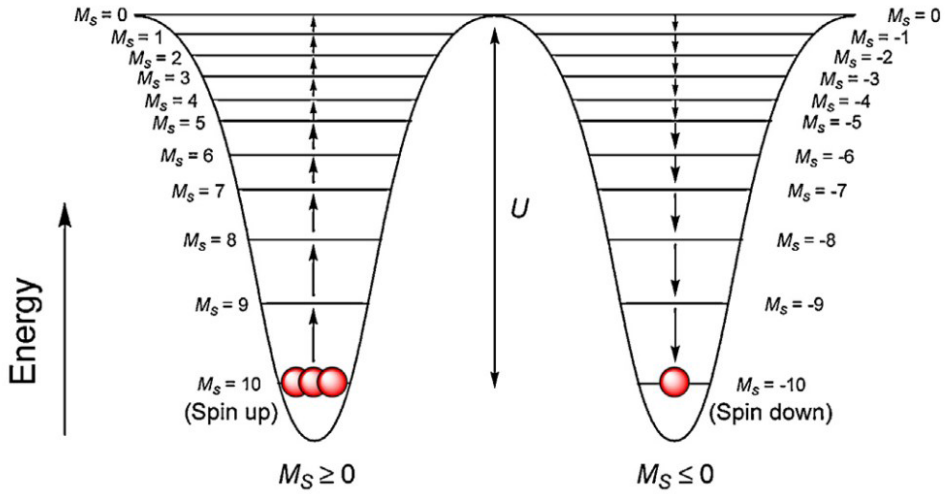

Figure 2 Schematic representation of the potential energy diagram showing the negative axial zero-field splitting of the M_s states of an *S* = 10 ground state. The red balls represent the occupation of spins in the spin-state.

These properties result in the Mn_{12} system displaying magnetic hysteresis in magnetization versus field measurements below 3.5 K with *U* = 50 cm^{-1} (71.94 K). Hysteresis is the classic signature of any magnet; those for a molecule (*cf*. a bulk magnet) being both temperature and frequency dependent. The temperature at which the hysteresis remains open at zero field is known as the blocking temperature (T_b) for the field sweep rate employed. **Fig**. **3** shows the hysteresis loops of $[Mn^{IV}_4Mn^{III}_8O_{12}(O_2CCH_3)_{16}(H_2O)_4]$ at 2.1 K.[21, 27]

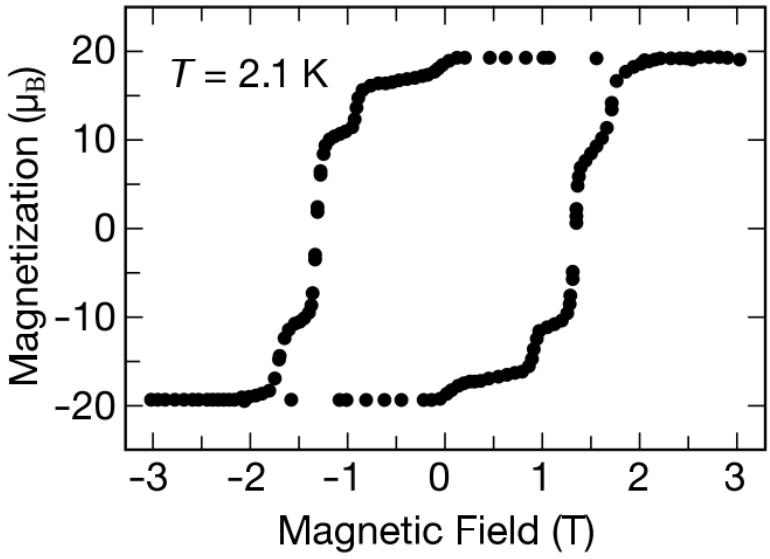

Figure 3 Magnetic hysteresis of $[Mn^{IV}_4Mn^{III}_8O_{12}(O_2CCH_3)_{16}(H_2O)_4]$ at 2.1K.[21, 27]

As well as this 'over-the-barrier' (Orbach) relaxation, the magnetisation can also relax through 'under-barrier' mechanisms such as quantum tunnelling of magnetisation (QTM).[27] This can occur between any two degenerate M_s sub-levels. Upon sweeping the magnetic field the field at which the energy levels become degenerate is evident with the observation of step-like features in the hysteresis loop (**fig**. **3**). A schematic showing the effect of applied field on the energy levels of a potential energy diagram and where QTM can occur is shown in **fig**. **4**. These relaxation processes are unfavourable for data storage as they represent a loss of information, and pose an additional complication in constructing a system that can retain its magnetisation at zero field with only an 'over-the-barrier' relaxation mechanism. The consequence of QTM is that the experimentally observed energy barrier to magnetization reversal (U_{eff}) is always smaller than that expected theoretically from the values of S and D. For the various derivatives of the Mn_{12} compound shown above, U_{eff} = 41.7-44.5 cm^{-1}.

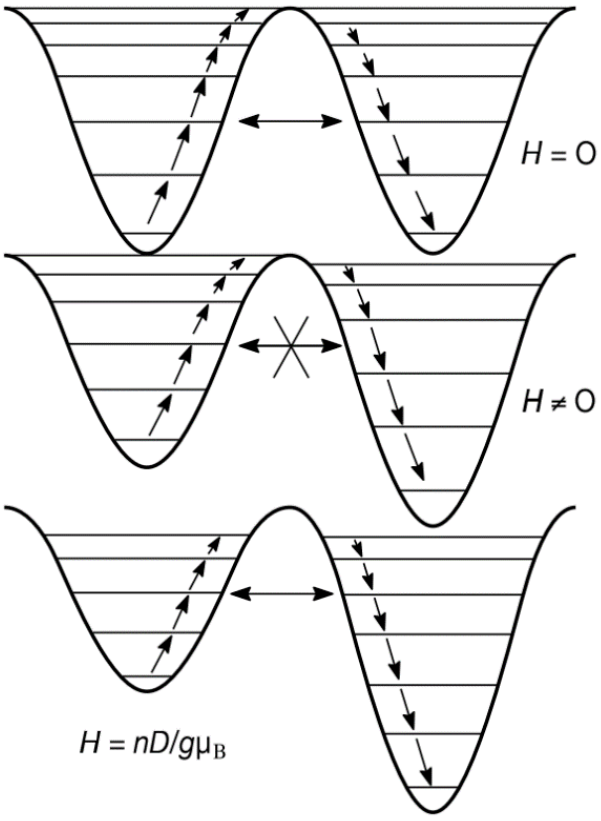

Figure 4 Diagram showing how the potential-energy diagram of an SMM changes as a magnetic field is swept from H = 0 to $H = nD/g\mu_B$. QTM occurs when the energy levels are aligned between the two halves of the diagram.[27]

The Mn_{12} family of complexes retained the largest U_{eff} values for more than a decade, before Milios and co-workers synthesised the complex $[Mn^{III}_6O_2(Et\text{-}sao)_6(O_2CPH(Me)_2)_2(EtOH)_6]$ (**fig**.

5) in 2007 built with phenolic oxime ligands (where Et-SaoH_2 = 2-hydroxyphenylpropanone oxime). This system contains two triangular [Mn_3] subunits that are bridged to one another through the Mn-N-O-Mn moieties of the oxime linkage. To date, this species still displays the record magnetization reversal energy barrier for 3*d* metal based polynuclear SMMs.[28] Ferromagnetic exchange interactions between the Mn(III) ions lead to an $S = 12$ ground state and an axial zero-field splitting, $D = -0.43$ cm^{-1}. This culminates in a U_{eff} value of 60 cm^{-1} (86.4 K) and open hysteresis loops to 5 K. The decisive component of this system being an SMM is the high spin ground-state combined with the axial anisotropy.[29-31]

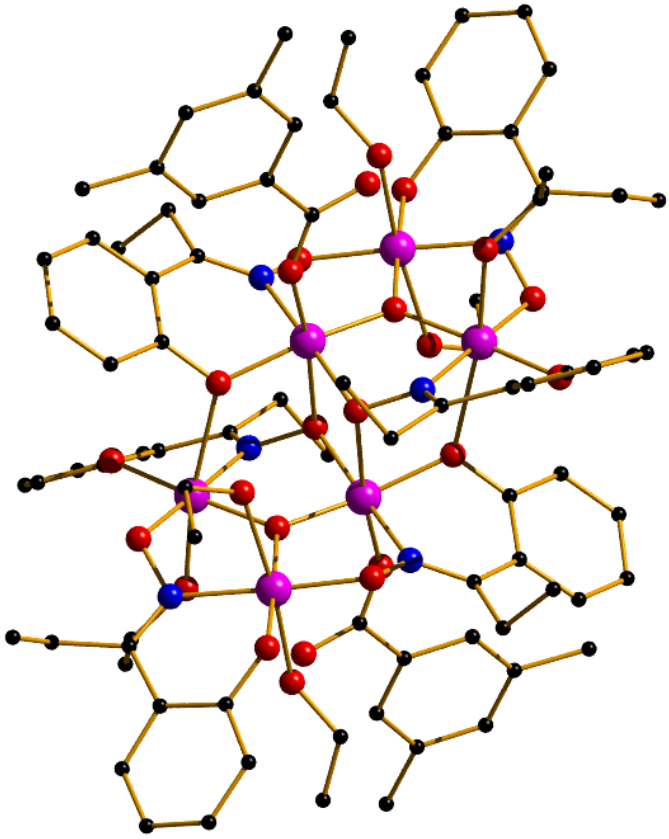

Figure 5 Structure of [$Mn^{III}_6O_2$(Et-sao)$_6$(O_2CPH(Me)$_2$)$_2$(EtOH)$_6$].[28] Colour scheme: Mn, pink; O, red; N, nitrogen; C, black (hydrogen atoms removed for clarity).

Despite much effort, and the synthesis of a very large number of high nuclearity complexes, the combination of very large *S* and very large *D* remained elusive, and indeed it was later shown that increasing *S* intrinsically leads to a decrease in *D*, limiting this methodology.[32-36] These include the [Mn_{84}] torus complex with the sum of the individual spins being 168, however even with this high *S* value, hysteresis is only shown below 1.5 K with a sweep rate of 0.035 T/s.[35]

This prompted a shift in the direction of the field, focussing on increasing *D* whilst maintaining a non-zero *S*. Thus, attention moved towards examining the effect of highly anisotropic (single) metal ions, with the 4*f* ions (the lanthanide series) appearing to be ideal candidates.[9, 37] However, they pose their own challenges due to their vastly more complex physical nature resulting from the core-like 4*f* orbitals, *i.e.* electrostatic bonding, highly distorted coordination geometries, weak magnetic exchange, non-trivial spin-orbit coupling and crystal field effects.

1.2 Lanthanide based single-molecule magnets

The chemistry of lanthanides is significantly different to transition metal chemistry owing to the contracted, core-like nature of 4*f* electrons. This results in the weak interaction between the 4*f* orbitals and the ligand *p* orbitals. This affects both the coordination chemistry and the electronic properties of the resultant complexes.

The origin of SMM behaviour in 4*f* systems is significantly more complicated due to several factors. Lanthanide ions have unquenched orbital angular momentum (*L*) which couples with the spin angular momentum (*S*) to describe the total angular momentum (*J*), *i.e.* $J = L + S$. Thus relatively simple, spin-only arguments, which assume $L = 0$ are not valid and the magnetic behaviour of any 4*f* system must be described in terms of *J* states., where the ground and excited state term symbols, *via* Russell-Saunders coupling, are described by $^{2S+1}L_J$. In generally these *J* multiplets are well separated with respect to each other with only the lowest energy state being occupied at room temperature. The ligand field, however weak, splits the $^{2S+1}L_J$ ground state multiplet into $2J+1$ 'Stark levels' which can either be singlets or doublets, depending if the metal is a Kramers or non-Kramers ion. Kramers ions are those that have an odd number of unpaired electrons, *e.g.* Dy^{III}, and non-Kramers ions are those which have an even number of unpaired electrons, *e.g.* Tb^{III}.[38, 39] **Fig**. **6** illustrates the energy scale of the electronic structure of a 4*f* ion.

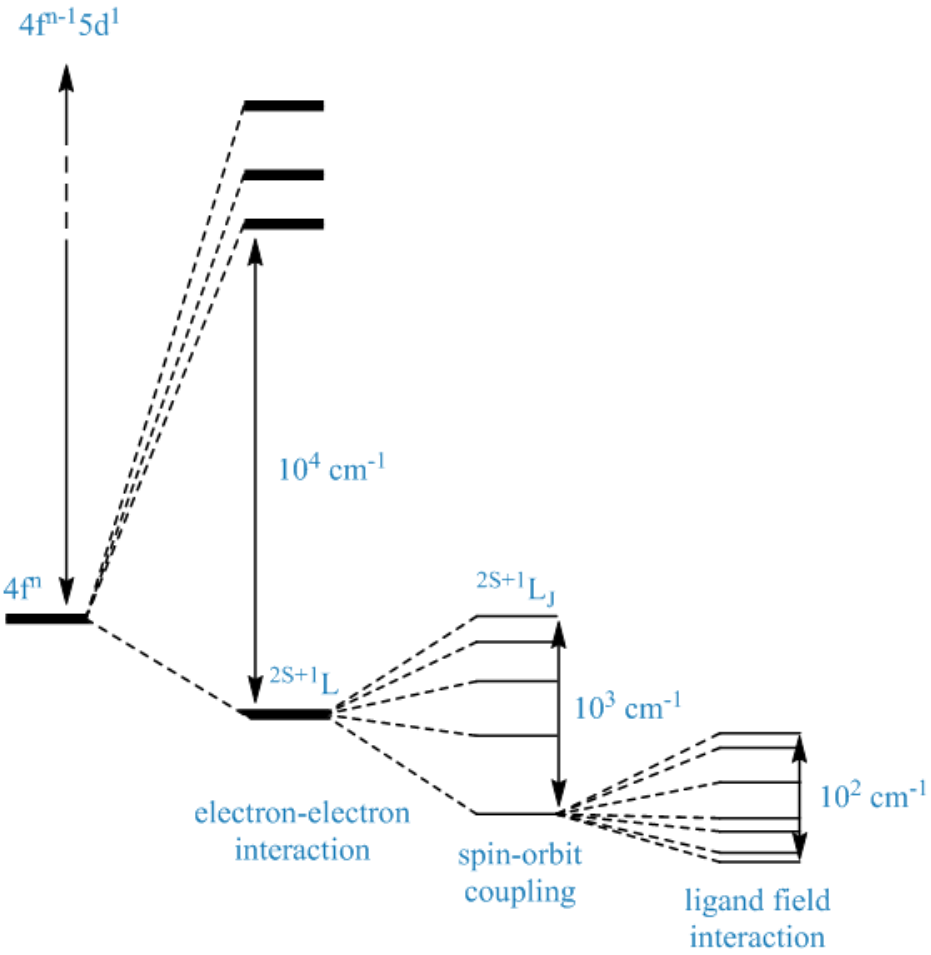

Figure 6 Schematic representation of the energy scale of the electronic structure of a lanthanide ion.

For polynuclear complexes, weak exchange interactions between the metal centres further complicates this picture as this can lead to the splitting of low lying energy states. The main challenge of developing SMMs with 4*f* ions is the fast QTM rate at zero field. An array of different methods have been employed to understand and reduce this QTM so that hysteresis can be achieved at higher temperatures.[9]

1.2.1 Development of 4*f* based SMMs

In 2003 the first mononuclear Ln^{III} system to exhibit SMM behaviour was found in two bis(phthalocyaninato)lanthanide complexes, $[(Pc)Ln(Pc)]^{-}\cdot TBA^{+}$ (where Pc = dianion of phthalocyanine ; Ln = Tb^{III} or Dy^{III}; $TBA^{+} = N(C_4H_9)_4^{+}$).[40-42] The Pc ligand is shown in **fig**. **7** (**a**) and the double decker arrangement formed by the complex is shown in **fig**. **7** (**b**).

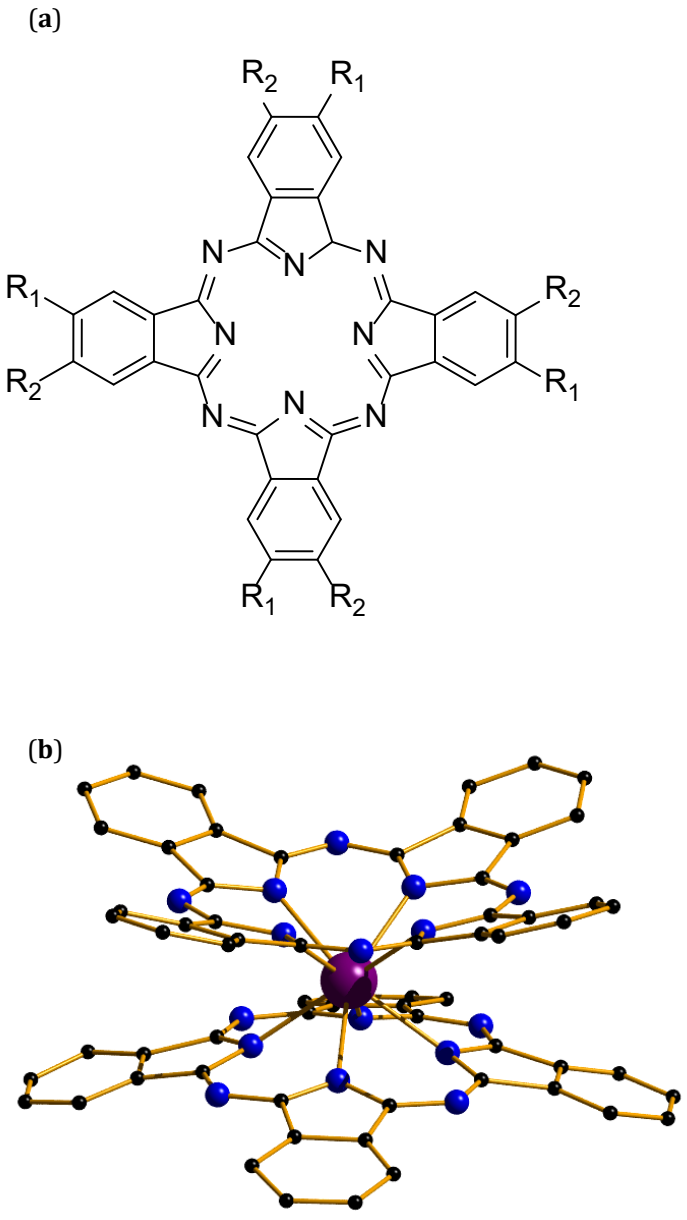

Figure 7 (**a**) Structure of the phthalocyanine ligand, Pc, where R_1 and R_2 are H. (**b**) Crystal structure of $[(Pc)Ln(Pc)]^{-}$ (Ln = Tb or Dy). Colour scheme: Dy, purple; N, nitrogen; C, carbon (hydrogen atoms removed for clarity).[40]

For the Tb^{III} complex, temperature dependent out-of-phase (χ_M'') ac susceptibility maxima were observed at 15, 32 and 40 K with frequencies 10, 100 and 997 Hz, respectively (**fig**. **8**). For the analogous Dy^{III} complex, they were observed at 4.5, 7 and 11.5 K at the same frequencies.[41, 43, 44]

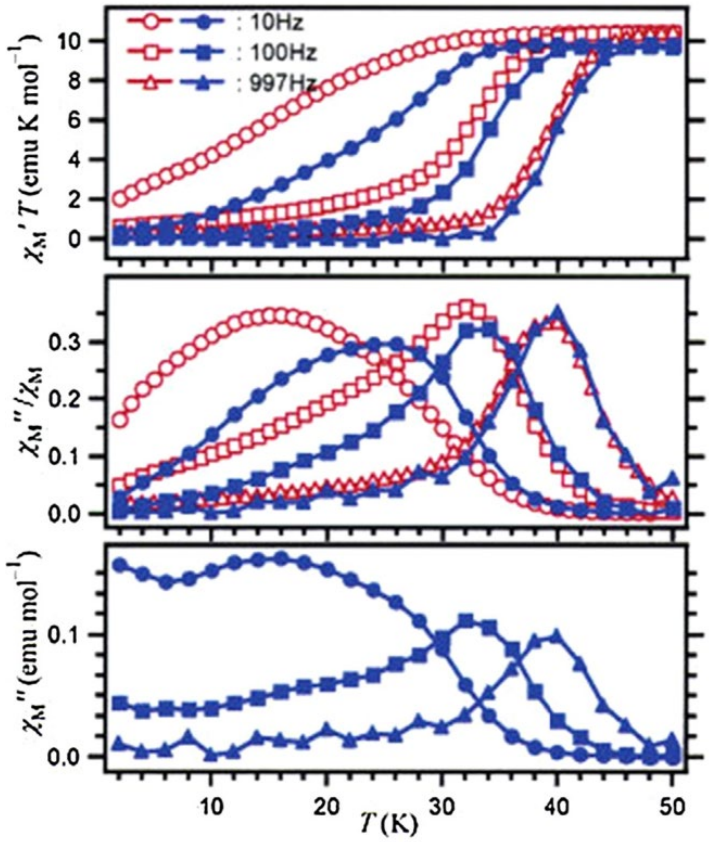

Figure 8 Plots of $\chi_M'T$ (top), χ_M''/χ_M (middle), and χ_M'' (bottom) against T for a powder sample of the $[(Pc)Tb(Pc)]^-\cdot TBA^+$ (open) and $[(Pc)Dy(Pc)]^-\cdot TBA^+$ (solid).[40]

When samples were diluted with the diamagnetic Yttrium complex $[(Pc)Y^{III}(Pc)]^-\cdot TBA^+$ in a 1:4 ratio, both systems showed a shift in the maxima of the ac peaks to a higher temperature, more so in the Dy^{III} system. This illustrates the SMM behaviour is intrinsic to the molecule and not a product of the extended lattice system. When the χ_M'' data was fitted to the Arrhenius law, the best fit parameters yielded U_{eff} = 230 cm^{-1} (331 K) and 28 cm^{-1} (40.3 K), with τ_0 = 1.6 x 10^{-7} s and 1.6 x 10^{-5} s for the Tb^{III} and Dy^{III} systems, respectively. These systems clearly illustrated that the energy barriers to magnetization relaxation in 4*f* species have the potential to be far higher than in 3*d* systems. This prompted further investigation into the use of Pc ligands by modifying the peripheral substituents (R_1 and R_2) with different charges in an attempt to improve the barrier heights.[45-49]

A detailed study reported in 2013 confirmed that neutral Tb^{III} bis(phthalocyaninates) molecules lead to higher effective barriers than their corresponding anionic species.[48] This investigation systematically modified Pc rings and analysed molecules in which both rings (**fig**. **7** (**a**)) were substituted with *tert*-butyl groups (^{t}Bu) (homoleptic), and where only one ring was substituted with ^{t}Bu (heteroleptic), with the second ring unsubstituted. The authors demonstrated that the bulky R-groups isolate the molecules from each other, which increasing the U_{eff} value, even when only one of the Pc rings had been modified. Substituting with electron-donating groups on just one of the Pc rings resulted in the N – Tb distance of the substituted ring increasing, 'pushing' the metal ion towards the unsubstituted (second) Pc ring. This method lead to what at the time was the record U_{eff} for a 4*f* system with the heteroleptic *tert*-butylphenoxy-substituted (R_1 and R_2) derivative recording a U_{eff} = 652 cm^{-1} (938 K) with τ_0 = 1 x 10^{-11} s, and frequency dependent maxima in ac susceptibility observed up to 58 K at 1000 Hz.[48] However, open hysteresis loops in zero dc field were not seen due to QTM, a problem that has permeated the field of 4*f* based molecular magnets. **Fig**. **9** shows the hysteresis measurement from a heteroleptic molecule where one Pc ring is substituted with a ^{t}Bu at the R_1 position. This system has U_{eff} = 642 cm^{-1} (923 K) and τ_0 = 2.2 x 10^{-11} s with frequency dependent maxima in ac susceptibility observed up to 52 K at 1000 Hz.

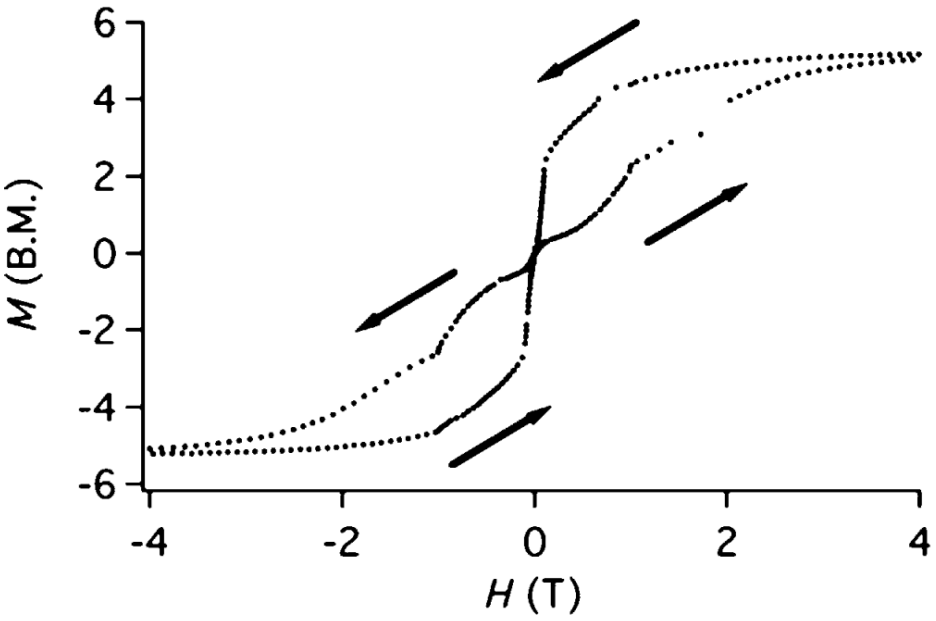

Figure 9 Plot of *M* versus *H* of [(Pc*)Tb(Pc*)] (* where R_1 = ^{t}Bu and R_2 = H) at *T* = 2 K illustrating 'butterfly hysteresis'.[48] The closing of the hysteresis loop at zero field is due to the presence of significant QTM.

Despite the high U_{eff} barriers, these systems cannot strictly be classed as SMMs as they cannot retain their magnetisation at zero field. This led to the investigation of higher

nuclearity systems in which the effect of additional (*d*, *f*) metal ions, and the subsequent exchange interactions, had on ground-state QTM.

In 2009 the polynuclear complex $[Dy_4(\mu_3\text{-}OH)_2(bmh)_2(msh)_4Cl_2]$ (**fig**. **10**) was reported with open hysteresis up to 7 K (**fig**. **11** (**a**)).[50] The structure of this complex has a commonly observed topology often referred to as a 'butterfly' and is composed of the deprotonated forms of 1,2-bis(2-hydroxy-3-methoxybenzylidene) hydrazone (H_2bmh) and 3-methoxysalicylaldehyde hydrazone (Hmsh).

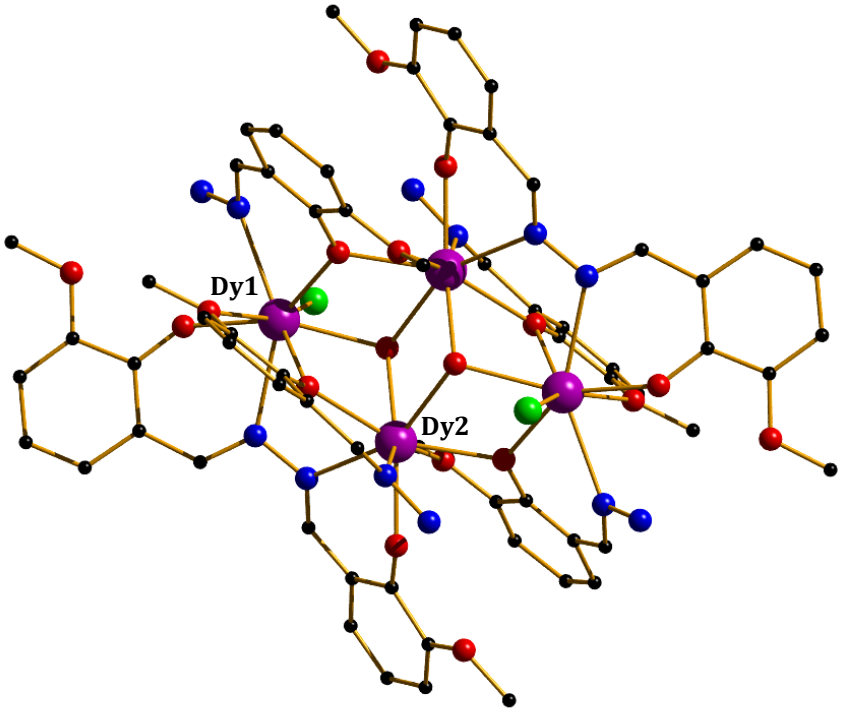

Figure 10 Structure of $[Dy_4(\mu_3\text{-}OH)_2(bmh)_2(msh)_4Cl_2]$. Colour scheme: Dy, purple; Cl, green; O, red; N, blue; C, black (hydrogen atoms removed for clarity).

Temperature dependent out-of-phase (χ_M'') ac susceptibility measurements carried out at 1500 Hz showed two peaks at 9 and 30 K (**fig**. **11** (**b**)), indicating the presence of two relaxation processes. It was deduced from *ab initio* studies that these two processes are a result of two unique Dy^{III} environments, with the Dy1 and Dy2 sites having first excited Kramers doublets lying 57.69 and 138.3 cm^{-1} (83 and 199 K) above the ground state, respectively. It was suggested that these differences between Dy1 and Dy2 are due to the changes in bond lengths, bridging angles, and/or the different orientations of the anisotropy

axes. Arrhenius plots constructed from the χ_M'' data afforded U_{eff} = 6.74 cm^{-1} and 118.2 cm^{-1} (9.7 and 170 K) and τ_0 = 3.2 x 10^{-5} and 4 x 10^{-7} s, respectively.[50]

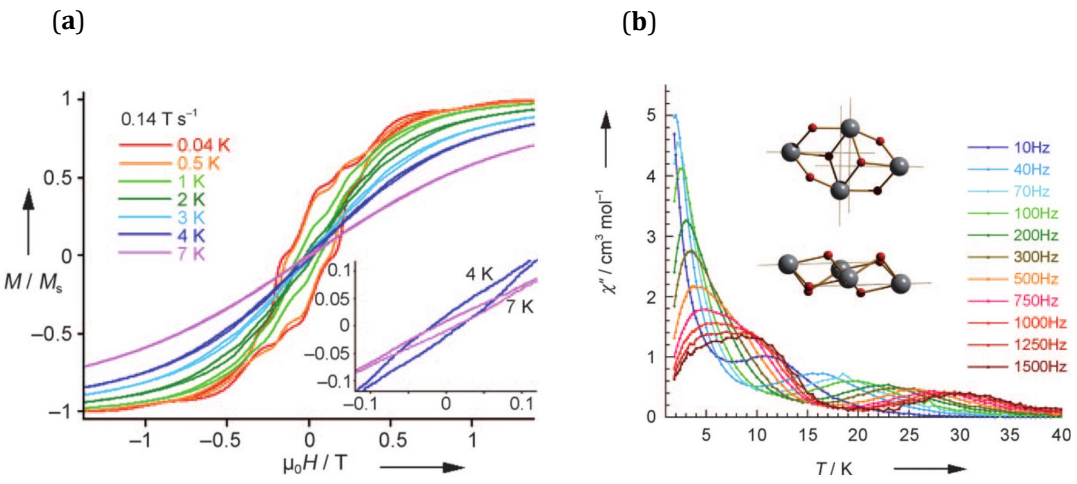

Figure 11 (**a**) Magnetisation (*M*) vs. applied dc field at the indicated sweep rates and temperatures. Inset: Zoomed-in section of the hysteresis loops showing an opening at 7 K. (**b**) Out-of-phase (χ_M'') ac susceptibility measurements of $[Dy_4(\mu_3\text{-}OH)_2(bmh)_2(msh)_4Cl_2]$, inset shows the anisotropy axis of each Dy^{III} ion.[50]

Although the system exhibits hysteresis up to 7 K, very high sweep rates of 0.14 T s^{-1} (1400 Oe s^{-1}) were required to remove the QTM. In fact, they are only slightly open with very small coercive fields above 1 K. This system does however highlight the importance/prominence of the highly anisotropic Dy^{III} ion. The problems associated with fully uncovering a quantitative picture of the slow relaxation of the magnetization in 4*f* complexes prompted the development of detailed theoretical work, which has since proved invaluable in the design, construction and quantitative modelling of new lanthanide-based molecular magnets.[50]

In 2013, a study of the isostructural $[Ln^{III}_4K^{I}_2O(O^tBu)_{12}]\cdot C_6H_{14}$ family of complexes (where Ln = Gd, Tb, Dy, Ho, Er, Y) (**fig. 12**) helped elucidate the role of the local environment of the Dy^{III} ions.[51] The Dy^{III} sites in $[Dy^{III}_4K^{I}_2O(O^tBu)_{12}]\cdot C_6H_{14}$ are six coordinate with distorted octahedral geometries. The four Dy^{III} and K^{I} ions form an oxo-centred octahedron with a *cis* arrangement of the two K^{I} ions. The Dy1,2 and Dy3,4 centres have statistically significant differences in the Dy-(μ_6-O) bond length with the latter being 0.06 Å shorter than the former.

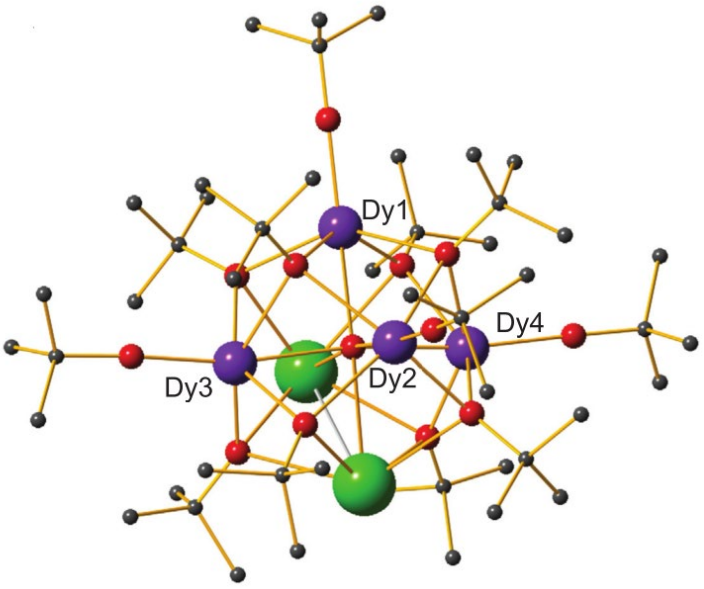

Figure 12 Crystal structure of $[Dy_4K_2O(O^tBu)_{12}]\cdot C_6H_{14}$. Colour scheme: Dy, purple; K, green; O, red; C, grey (hydrogen atoms removed for clarity).[51]

Ac susceptibility measurements of $[Dy^{III}_4K^{I}_2O(O^tBu)_{12}]\cdot C_6H_{14}$ revealed complex dynamic behaviour showing two distinct frequency dependent thermal relaxation processes in the χ'' plots. These two relaxation processes found maxima at 30 and 47 K at 1200 Hz. The Arrhenius data gave U_{eff} = 481 and 220 cm^{-1} (692 and 316 K) with τ_0 = 6.6 x 10^{-11} and 2.6 x 10^{-9} s, respectively. The $[Y^{III}_4K^{I}_2O(O^tBu)_{12}]\cdot C_6H_{14}$ analogue was synthesised to facilitate study of a diluted Dy^{III} sample; in the synthetic procedure ~5% of a Dy^{III} salt was added in place of the Y^{III} salt. This gave a system consisting of $[DyY_3K_2]$ in a $[Y_4K_2]$ matrix. Analysis of the ac susceptibility measurements afforded U_{eff} = 585 cm^{-1} (842 K).[51]

Electronic structure calculations revealed that the first and second excited states (labelled 2± and 3± in **fig**. **13**) of each Dy^{III} centre has an average energy gap of 373 and 617 cm^{-1} (536 and 888 K) from the ground state (1±). This suggests that the U_{eff} barrier of the diluted sample is too high to correspond with relaxation via the 2± state and therefore must be associated with relaxation via the 3±. Therefore, relaxation via the 2± state is quenched or uncompetitive. The 1± state corresponds to a pure m_J = ±15/2 ground state with $g_z \approx 20$ and $g_{x,y} \approx 0$ and is therefore an ideal Ising state. The 2± state corresponds to an almost pure Ising m_J = ±13/2 with g values of $g_z \approx 17$ and $g_{x,y} < 0.5$. The 3± state has a substantial transverse magnetic moment with $g_z \approx$ 12-16 and $g_{x,y} < 4$.[51]

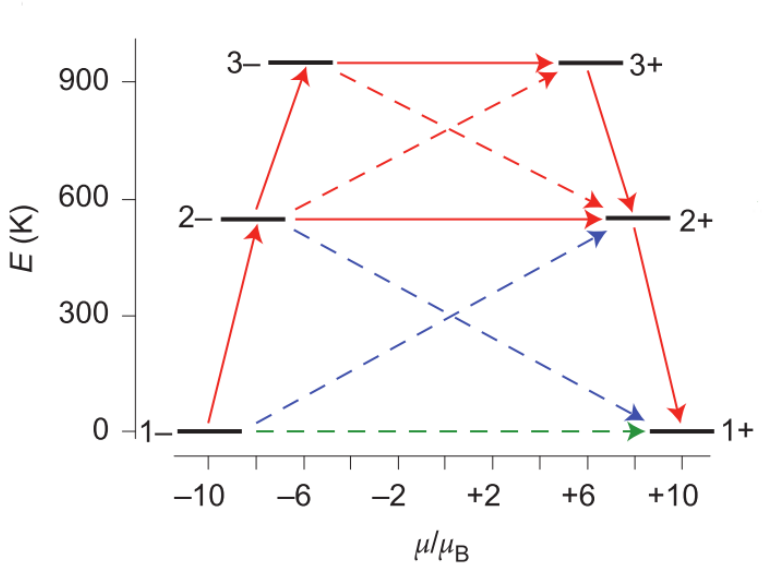

Figure 13 Lowest three Kramers doublets for the individual Dy sites in $[Dy^{III}_4K^{I}_2O(O^tBu)_{12}]\cdot C_6H_{14}$, with possible relaxation paths. The thick black lines represent the Kramers doublets as a function of their magnetic moment along the main anisotropy axis. The green dashed line corresponds to ground-state QTM, the solid red lines to TA-QTM via the first and second excited Kramers doublets. Dashed red and blue lines show possible Orbach processes.[51]

The different behaviour of the pure Dy^{III} sample and the diluted sample is a consequence of intramolecular interactions between neighbouring Dy^{III} atoms in the former species, which create local fluctuating transverse magnetic fields. There are two possible explanations for the differences observed. (1) The transverse magnetic field is the field created by spins orthogonal ($g_{x,y}$) to the principle axis (g_z). If these $g_{x,y}$ values are large, the electrons are unlikely to stay aligned with the principle axis (g_z) and can result in the spins flipping – this is the origin of QTM. To avoid QTM, the $g_{x,y}$ values of each state should be as close to zero as possible. Bearing this in mind, the undiluted sample has very small transverse g values in the 2± state and therefore thermally-activated QTM (TA-QTM) cannot occur. (2) The g_z of the 1± and 2± states are almost parallel which disfavours relaxation via the 2± state. The intramolecular interactions also result in the tunnel splitting within the $\pm m_J$ Kramer doublets being larger which makes TA-QTM more competitive via the 2± states. Ground state QTM will also become more competitive and therefore the corresponding U_{eff} values of the thermal relaxation pathways will be lower than predicted, as observed.[51]

1.2.2 4*f* Triangles

As it has been shown that even weak exchange interactions can have a profound impact on the magnetic behaviour of 4*f* systems it becomes clear that this exchange, in combination with certain structural motifs, can result in novel magnetic phenomena. In 2006 the triangular dysprosium complexes of general formula $[Dy^{III}_3(\mu_3\text{-}OH)_2L_3Cl_2(H_2O)_4][Dy_3(\mu_3\text{-}OH)_2L_3Cl(H_2O)_5]Cl_5$ were synthesised, where HL = *o*-Vanillin (2-hydroxy-3-methoxy-benzaldehyde) (**fig**. **14**).[52] Initial measurements showed anomalous behaviour - even with the Dy^{III} ions having an odd number of unpaired electrons, a vanishing susceptibility at low temperature ($\chi_M T$ approaches 0) was observed. Despite this, SMM behaviour is observed with U_{eff} = 42.9 cm^{-1} (61.7 K) and τ_0 = 2.2 x 10^{-8} s. This was a highly significant discovery as it illustrates conclusively that a large value of the ground state is not a necessary condition to observe slow magnetization relaxation.

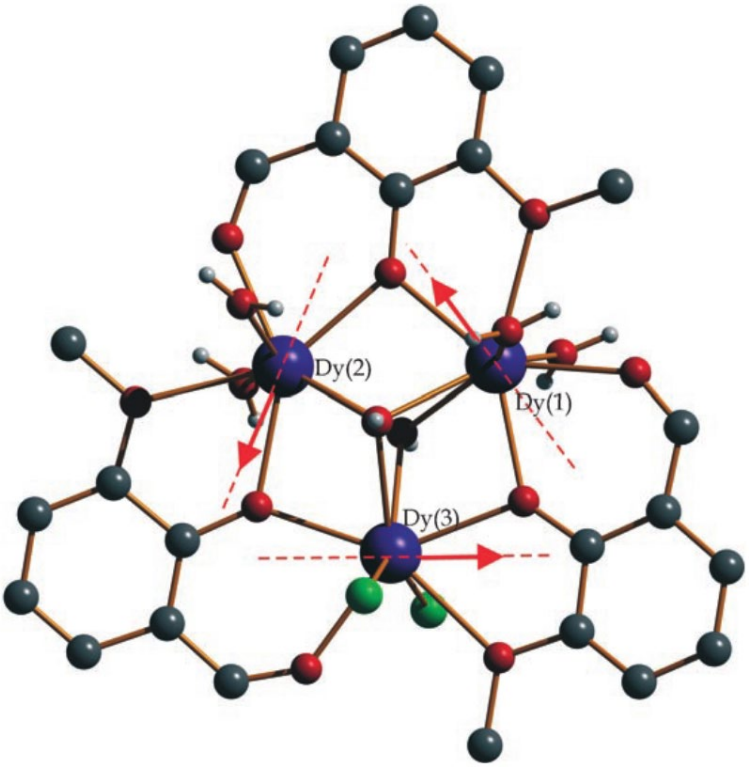

Figure 14 Structure of $[Dy^{III}_3(\mu_3\text{-}OH)_2L_3Cl_2(H_2O)_4]$. Colour scheme: Dy, blue; Cl, green; O, red; C, dark grey; H, light grey. The dashed red lines show the calculated anisotropy axes and the arrows show the ordering of local magnetisation in the ground state.[53]

Theoretical work, including *ab initio* calculations, showed that the non-magnetic ground state is a result of a toroidal arrangement of the magnetic moments of the Dy^{III} sites (**fig**. **14** – red arrows).[53-55] Toroidal moments are unaffected by external magnetic fields, as illustrated

in the magnetisation (*M*) versus field (*H*) plots where there is a lag in the magnetisation of the sample up to approximately 0.75 T (**fig**. **15**). A simulation of the powder magnetic susceptibility and magnetisation data using *ab initio* methodology revealed an exchange interaction of J = -0.6 cm^{-1}.[53]

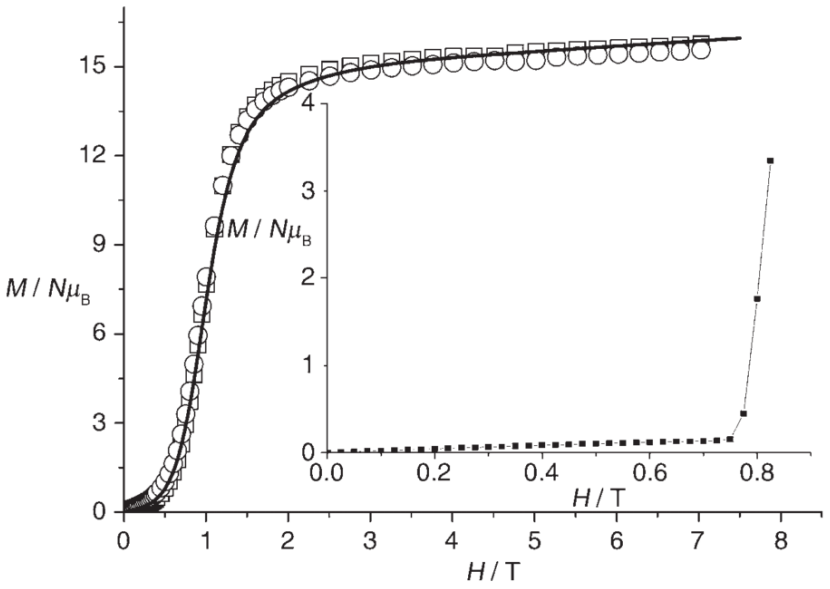

Figure 15 *M* versus *H* calculated for J = 0.6 cm^{-1} (solid lines) for a polycrystalline sample, and the experimental powder magnetisation, for $[Dy^{III}_3(\mu_3\text{-}OH)_2L_3Cl_2(H_2O)_4]Cl_5\cdot 19H_2O$ (empty squares) and $[Dy^{III}_3(\mu_3\text{-}OH)_2L_3Cl_2(H_2O)_4]Cl_3\cdot 4H_2O$ (empty circles) at T = 1.8 K. Inset: the same simulations for T = 0.1 K.[53]

The toroidal moment arises from specific magnetic interactions between the metal sites. Therefore, these moments can be influenced by molecular symmetry, local magnetic moments, dipole interactions and exchange interactions between metal sites.[55-58]

1.2.3 3*d*-4*f* SMMs

One method that has been employed in an attempt to improve the SMM behaviour of 4*f* systems is to construct heterometallic complexes, by combining 4*f* metal ions with 3*d* metal ions. This blends the large anisotropy of the 4*f* metals with the promotion of stronger exchange interactions seen in 3*d* metals.[59, 60] The first example of a 3*d*-4*f* SMM was reported in 2005 with the complex $[NMe_4]_2[Mn^{III}_2Dy^{III}_2(tmp)_2(O_2CCMe_3)_4(NO_3)_4]\cdot 2MeCN\cdot 0.5H_2O$ (where H_3tmp is the tripodal alcohol 1, 1, 1-tris(hydroxymethyl)ethane).[61] The structure of this complex again comprises a 'butterfly' motif where the Mn^{III} ions form the 'body' and the Dy^{III} ions form the 'wings' (**fig**. **16**). Frequency dependent behaviour was shown in the out-of-phase ac susceptibility measurements at zero field. Fitting the data to the Arrhenius equation revealed U_{eff} = 10.43 cm^{-1} (15 K) and τ_0 = 3.31 x 10^{-7} s.

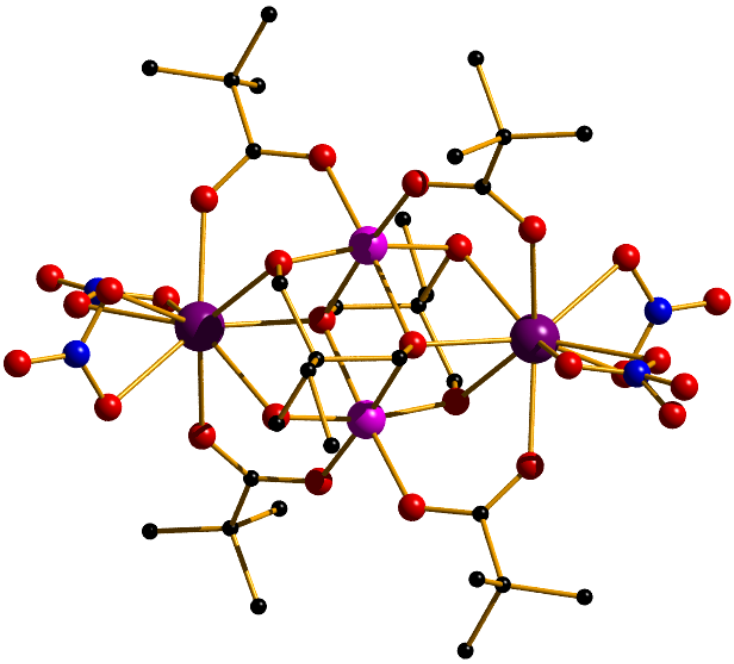

Figure 16 Molecular structure of $[NMe_4]_2[Mn^{III}_2Ln^{III}_2(tmp)_2(O_2CMe_3)_4(NO_3)_4]$. Colour scheme: Dy, purple; Mn, pink; O, red; C, black (hydrogen atoms omitted for clarity).[61]

Hysteresis loops were shown up to 1 K, however there was no significant coercive field present (**fig**. **17** (**a**)). By reducing the temperature to 0.04 K the hysteresis loops were opened at zero field with scan rates of 0.002 – 0.070 T s^{-1} (**fig**. **17** (**b**)).

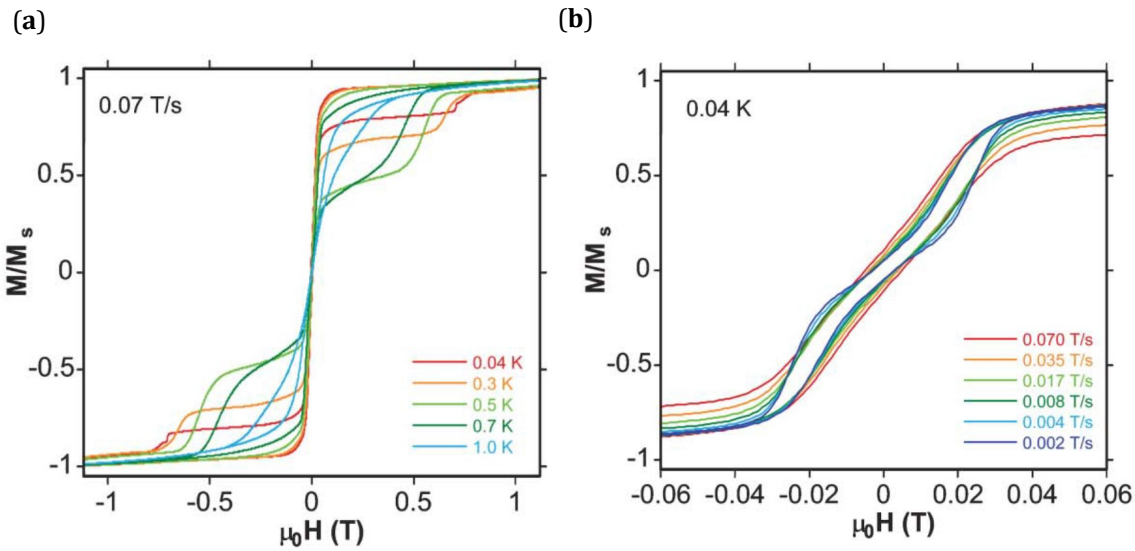

Figure 17 Hysteresis loops for $[Mn_2Dy_2]$ measured at (a) T = 0.04 – 1.0 K with a sweep rate of 0.070 T s^{-1} and (b) T = 0.04 K with sweep rates of 0.002 T s^{-1} – 0.070 T s^{-1}.[46]

The closing of the hysteresis loops is a result of QTM (or TA-QTM) of the ground (or excited) states, but the roles played by the Mn^{III} or Dy^{III} ions could not be deduced due to the complexity of the system. It is important to note that in systems containing (multiple) anisotropic 3*d* and 4*f* ions, the number of parameters that govern the magnetic behaviour is so extensive that meta-analysis is very challenging. By effectively swapping out paramagnetic 3*d* metals with diamagnetic alternatives, the effect of the 3*d*-4*f* and 4*f*-4*f* exchange interactions (J_{3d4f}, J_{4f4f}) on the dynamic properties can be probed more closely. Employing the same strategy for the paramagnetic 4*f* ions highlights the role of the 3*d*-3*d* exchange interactions (J_{3d3d}). Although there will be some structural differences due to the difference in ionic radii and coordination environment of the ions between the structures, describing them as isostructural is a good first approximation.

In 2015 a study of a family of butterfly structures $[M^{II}_2Ln^{III}_2(\mu_3\text{-}OH)_2(O_2C^tBu)_{10}]^{2-}$ (where M = Mg^{II}, Mn^{II}, Co^{II}, Ni^{II} and Cu^{II}; Ln = Y^{III}, Gd^{III}, Tb^{III}, Dy^{III}, Ho^{III} and Er^{III}) containing 27 isostructural members began to elucidate these roles.[62] **Fig**. **18** shows the crystal structure of the $[Mg_2Dy_2]$ analogue. The 3*d* ions (M^{II}) occupy the 'body', and the 4*f* ions (Ln^{III}) occupy the 'wings' of a butterfly structure. The M^{II} and Ln^{III} ions are bridged through the O-atoms of the carboxylate ligands and hydroxide ions.

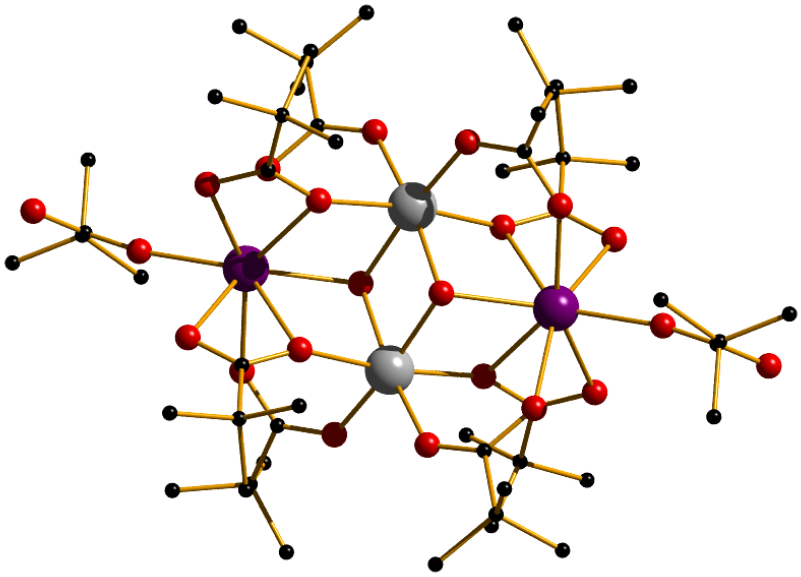

Figure 18 Crystal structure of $[Mg^{II}_2Dy^{III}_2(\mu_3\text{-}OH)_2(O_2C^tBu)_{10}]^{2-}$ anion. Colour scheme: Dy, purple; Mg, grey; O, red; C, black (hydrogen atoms omitted for clarity).[62]

The metallic core in **fig**. **19** highlights the possible exchange pathways, where $J_1 = J_{MM}$, $J_2 = J_{MLn}$, $J_3 = J_{LnLn}$. In this case, diamagnetic Mg^{II} was used in place of the paramagnetic 3*d* metals and Y^{III} was used as the diamagnetic lanthanide. Due to the large anisotropy of the 3*d* and 4*f* metals the $\chi_M T$ data could not be modelled directly to quantify the exchange interactions. By adding the $\chi_M T$ data of $[Mg_2Dy_2]$ to $[Ni_2Y_2]$ and comparing the data obtained directly to that of the $[Ni_2Dy_2]$ complex, the J_{NiDy} interaction can be classified qualitatively.

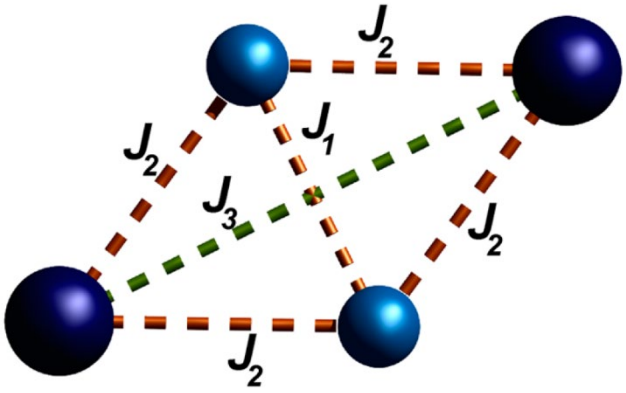

Figure 19 Exchange scheme of $[M_2Ln_2]$ highlighting the magnetic exchange pathways with dashed lines. Colour scheme: M, light blue; Ln, dark blue.[62]

The $[Mg_2Dy_2]$, $[Mn_2Dy_2]$, $[Ni_2Dy_2]$, $[Mg_2Er_2]$ and $[Ni_2Er_2]$ clusters all show frequency dependent peaks in out-of-phase ac susceptibility measurements. The $[Mg_2Dy_2]$ analogue revealed U_{eff} = 30.58 cm^{-1} (44 K), the $[Mn_2Dy_2]$ and $[Ni_2Dy_2]$ analogues have U_{eff} = 20.16 cm^{-1}

(29 K) and 13.9 cm^{-1} (20 K), respectively. A similar trend is seen in the Er complexes where $[Mg_2Er_2]$ and $[Ni_2Er_2]$ have U_{eff} = 15.99 cm^{-1} (23 K) and 8.34 cm^{-1} (12 K), respectively. As none of the $[M_2Y_2]$ samples showed any signals in the out-of-phase AC susceptibility measurements, the SMM behaviour is clearly due to the lanthanide ions in the molecule. *Ab initio* calculations also suggest that there is little electronic difference between the Dy^{III} and Er^{III} sites in the various compounds, suggesting the small structural changes are not at the origin of the differences in dynamic behaviour. Stronger exchange interactions are observed in the $[Co_2Ln_2]$ and $[Cu_2Ln_2]$ samples which coincided with no observable dynamic behaviour as in the $[Co_2Dy_2]$ and $[Cu_2Dy_2]$ samples. Therefore, in both the Dy and Er cases the addition of a J_{MLn} interaction in the system reduces the U_{eff} value, regardless if the interaction is ferromagnetic (F) or antiferromagnetic (AF).

1.2.3 Radical Bridged 4*f* SMMs

In 2011, it was shown that radicals provide exceptionally strong magnetic exchange coupling with 4*f* ions, potentially solving the problems associated with the "de-activating" QTM and promoting only thermally activated relaxation mechanisms. For example, the N_2^{3-} radical-bridged dilanthanide complexes $[[(Me_3Si)_2N]_2(THF)Tb]_2(\mu\text{-}\eta^2\text{:}\eta^2\text{-}N_2)^-$ (**fig**. **20** (**a**)) show magnetic hysteresis up to 14 K (**fig**. **20** (**b**)).[63]

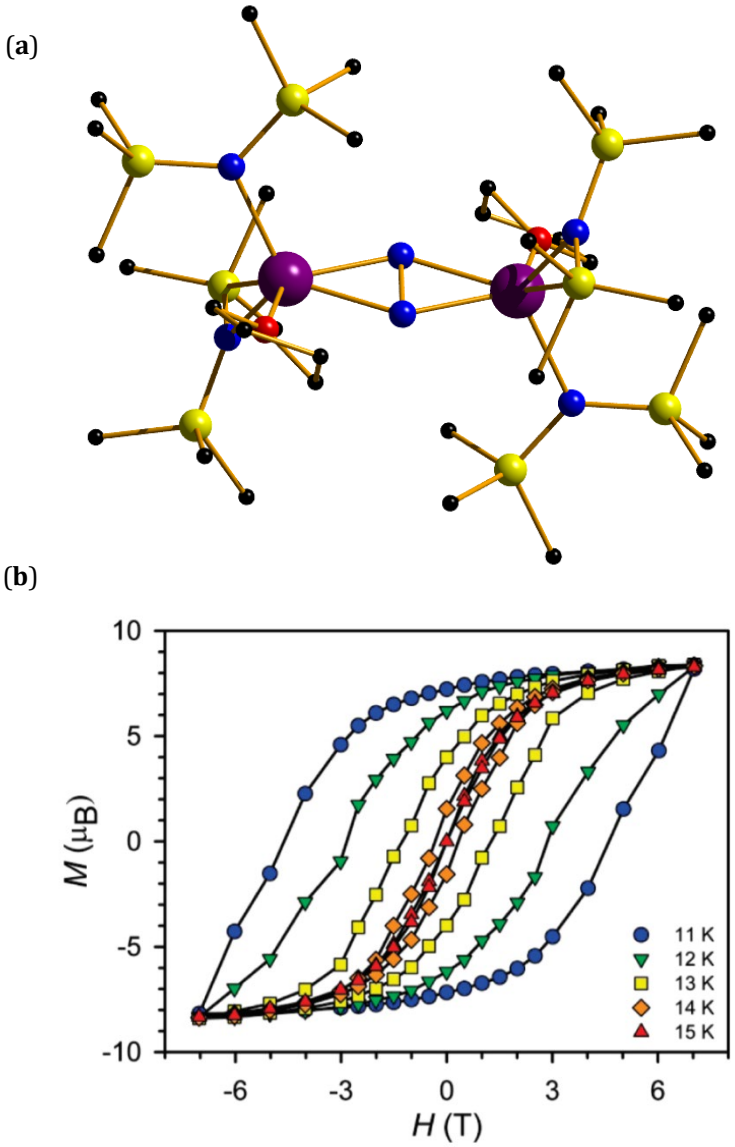

Figure 20 (a) Structure of the N_2^{3-} radical bridged complex $[[(Me_3Si)_2N]_2(THF)Tb]_2(\mu\text{-}\eta^2\text{:}\eta^2\text{-}N_2)^-$. Colour scheme: Tb, purple; Si, yellow; O, red; N, blue; C, black (hydrogen atoms omitted for clarity). (b) *M* v *H* of $[[(Me_3Si)_2N]_2(THF)Tb]_2(\mu\text{-}\eta^2\text{:}\eta^2\text{-}N_2)^-$ from 11 to 15 K (average sweep rate 0.9 mT/s).[48]

1.2.5 A Return to Mononuclear Systems

After 15 years of studying 4*f* systems, it was hypothesised that to further enhance the temperature at which magnetic hysteresis is observed, the axial crystal field parameters must be maximised.[64] This entails removing all equatorial ligand interactions and employing large, bulky axial ligands. For example, using a cyclopentadienyl (Cp) type ligand, resulting in a mononuclear double decker arrangement similar to that first shown by Ishikawa *et al* in 2003. This was realised in 2017 with the synthesis of the hexa-*tert*-butyldysprosocenium complex, $[Dy(Cp^{ttt})_2][B(C_6F_5)_4]$ where $Cp^{ttt} = (C_5H_2{}^tBu_3\text{-}1,2,4)$ and $^tBu = C(CH_3)_3$ as shown in **fig**. **21** (**a**).[64, 65]

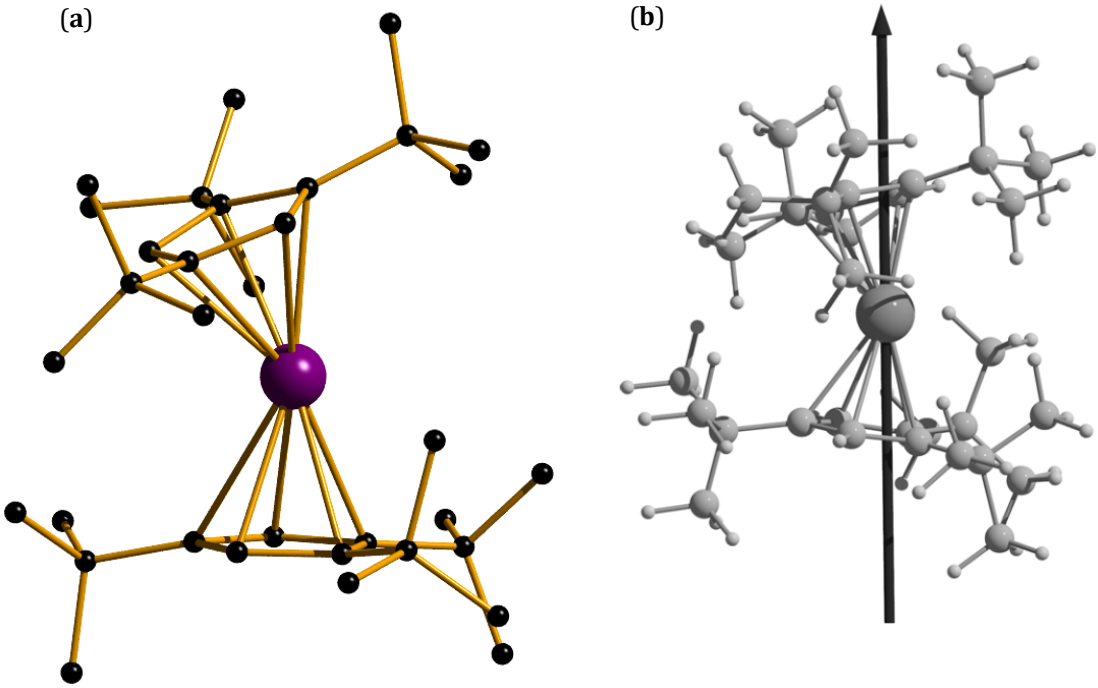

Figure 21 (**a**) Molecular structure of $[Dy(Cp^{ttt})_2][B(C_6F_5)_4]$. Colour scheme: Dy, purple; C, black (H atoms removed for clarity).[65] (**b**) Direction of the principal axis of the *g*-tensor in the ground Kramer doublet of $[Dy(Cp^{ttt})_2][B(C_6F_5)_4]$.[64]

Up to the fourth Kramer doublet the *g*-tensor remains essentially perfectly axial, as shown in **fig**. **21** (**b**) which correlates with a Cp-Dy-Cp angle of 152.84°.[64] This axial system exhibits a staggering improvement in the magnetic properties, with open hysteresis loops up to 60 K (**fig**. **22**).[65]

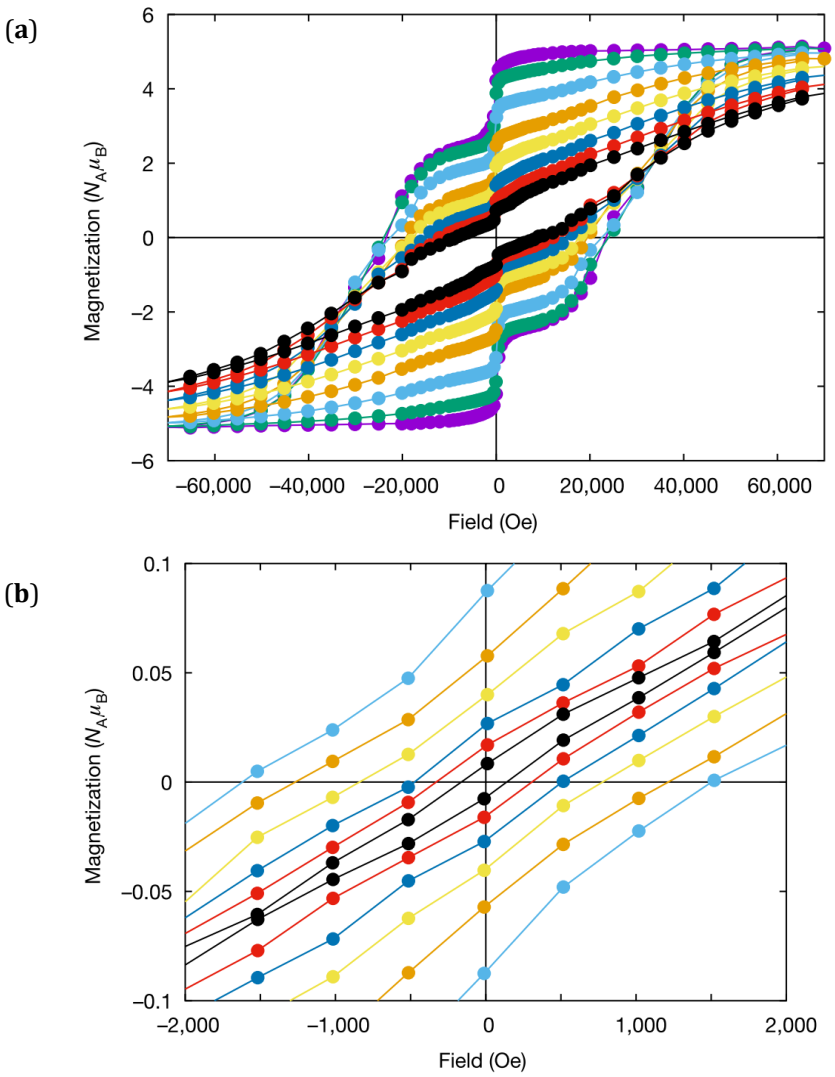

Figure 22 (**a**) Hysteresis loops recorded from 2 K (purple) to 30 K (black) in steps of 4 K. (**b**) Hysteresis loops recorded from 52 K (light blue) to 62 K (black) in steps of 2 K.[65]

The discovery of this system was a seminal moment for the field of SMM research edging T_B closer to 77 K where liquid nitrogen could be used in place of the very expensive and rare liquid helium. In October 2018, this barrier was broken again and hysteresis above 77 K was achieved with the synthesis of the dysprosium metallocene, $[(Cp^{iPr5}Dy(Cp^*)]^+$ (Cp^{iPr}, penta-iso-propylcyclopentadienyl; Cp* pentamethylcyclopentadienyl) (**fig**. **23**).[66] Magnetic studies reveal U_{eff} = 1541 cm^{-1} (2466 K) and magnetic hysteresis up to 80 K (**fig**. **24**).

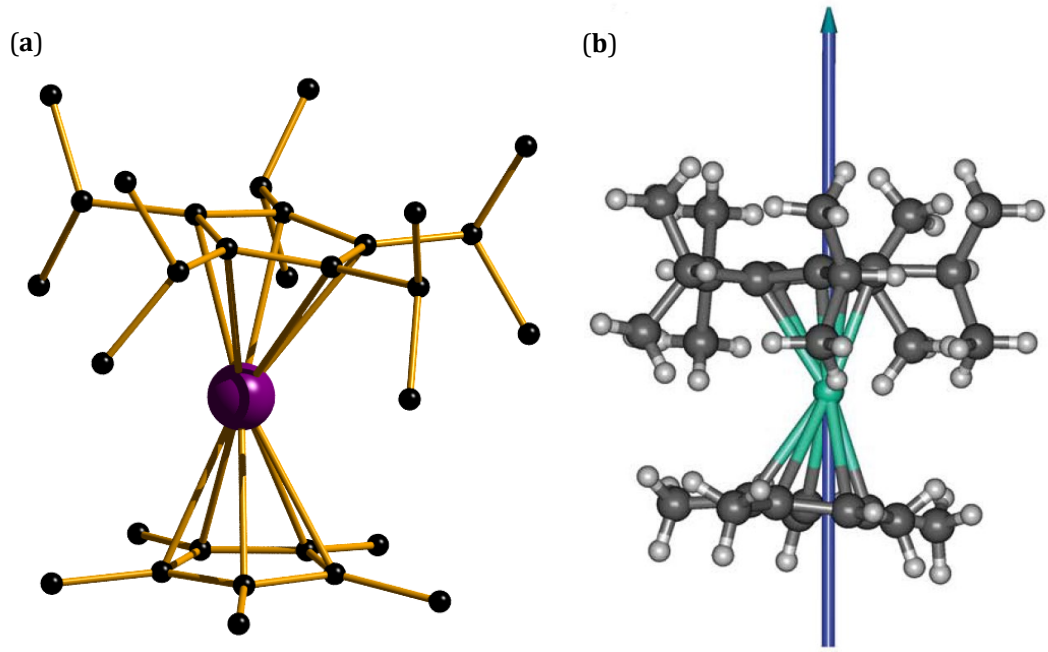

Figure 23 (**a**) Molecular structure of $[(Cp^{iPr5}Dy(Cp^*)]^+$. (**b**) The principle axis of the ground state Kramers' doublet in $[(Cp^{iPr5}Dy(Cp^*)]^+$.[66]

This system further maximised the axial crystal field parameters, correlating with a Cp-Dy-Cp angle of 162.50° almost 9.7° wider than the previous metallocene. This solidifies the notion that this parameter is paramount in increasing the temperature at which blocked magnetisation can be retained. Although the magnetic behaviour of this complex suggests such species can be employed at practical temperatures, one has to note that these metallocene complexes are not stable under ambient conditions and are both highly air- and moisture-sensitive, making real world applications doubtful.

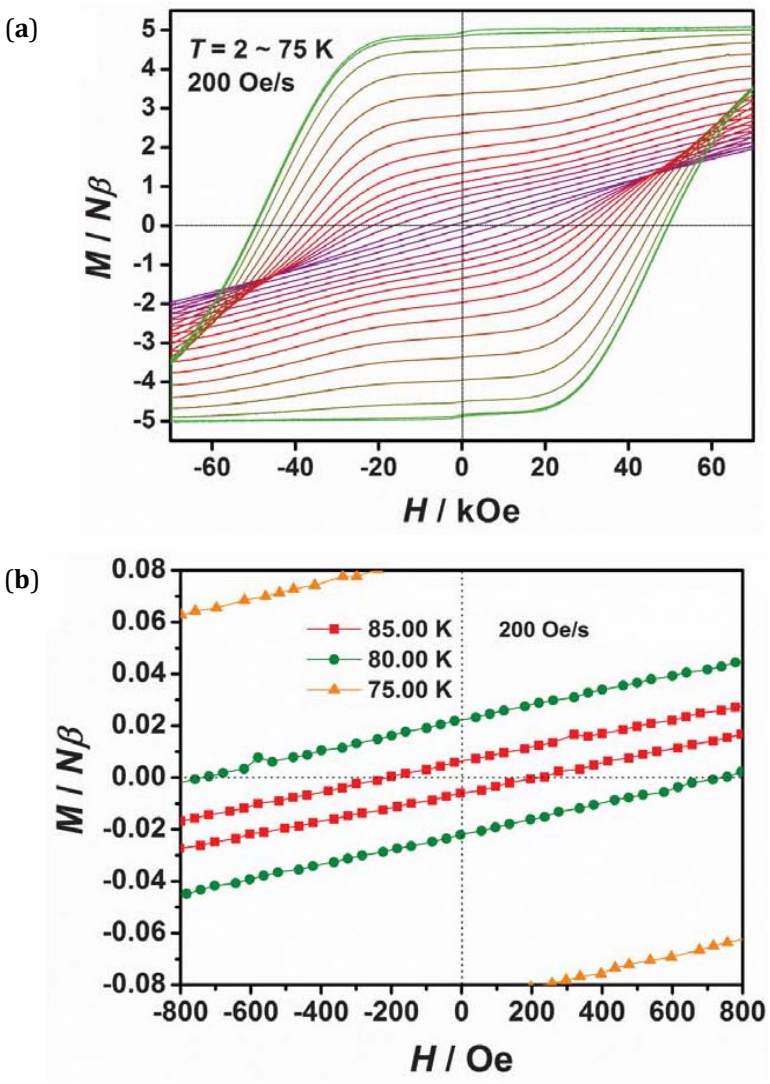

Figure 24 (**a**) Hysteresis loops recorded from 2 K (purple) to 75 K (purple) in steps of 5 K for the $[(Cp^{iPr5}Dy(Cp^*)]^+$ cation. (**b**) Hysteresis loops recorded from 75 K (orange) to 85 K (red) in steps of 5 K.[66]

The following chapters investigate the effectiveness of several of the methods discussed to improve SMM behaviour in polymetallic 3/4*d*-4*f* systems. Synthesis of novel 3/4*d*-4*f* systems and subsequent structural and magnetic characterisation and *ab initio* computational analysis were undertaken to elucidate these effects. The structures investigated were chosen due to their suitability in terms of what was being investigated in each chapter.

1.3 References

1. O. Kahn, Molecular Magnetism, *VCH*, 1993.
2. Z. Fu, Y. Xiao, Y. Su, Y. Zheng, P. Kögerler and T. Brückel, *Euro. Phys. Let.*, 2015, **112**, 27003.
3. R. McLellan, M. A. Palacios, C. M. Beavers, S. J. Teat, S. Piligkos, E. K. Brechin and S. J. Dalgarno, *Chem. Euro. J.*, 2015, **21**, 2804-2812.
4. J. W. Sharples, Y. Z. Zheng, F. Tuna, E. J. McInnes and D. Collison, *Chem. Comm.*, 2011, **47**, 7650-7652.
5. S.-J. Liu, J.-P. Zhao, J. Tao, J.-M. Jia, S.-D. Han, Y. Li, Y.-C. Chen and X.-H. Bu, *Inorg. Chem.*, 2013, **52**, 9163-9165.
6. P. Hermann, J. Kotek, V. Kubicek and I. Lukes, *Dalton Trans.*, 2008, **23**, 3027-3047.
7. E. J. Werner, A. Datta, C. J. Jocher and K. N. Raymond, *Angew. Chem. Int. Ed.*, 2008, **47**, 8568-8580.
8. J. L. Liu, W. Q. Lin, Y. C. Chen, S. Gomez-Coca, D. Aravena, E. Ruiz, J. D. Leng and M. L. Tong, *Chem. Euro. J*, 2013, **19**, 17567-17577.
9. S. T. Liddle and J. van Slageren, *Chem. Soc. Rev.*, 2015, **44**, 6655-6669.
10. R. Sessoli and A. K. Powell, *Coord. Chem. Rev.*, 2009, **253**, 2328-2341.
11. J. Luzon and R. Sessoli, *Dalton Trans.*, 2012, **41**, 13556-13567.
12. L. Rosado Piquer and E. C. Sanudo, *Dalton Trans.*, 2015, **44**, 8771-8780.
13. W. Wernsdorfer, R. Sessoli, A. Caneschi, D. Gatteschi, A. Cornia and D. Mailly, *J. App. Phys.*, 2000, **87**, 5481-5486.
14. S.-Y. Lee and S.-K. Yoo, *Phys. Rev. B*, 2000, **62**, 13884-13887.
15. W. Wernsdorfer and R. Sessoli, *Science*, 1999, **284**, 133-135.
16. C. S. Tautermann, A. F. Voegele and K. R. Liedl, *J. Chem. Phys.*, 2004, **120**, 631-637.
17. D. Gatteschi and R. Sessoli, *Angew. Chem. Int. Ed.*, 2003, **42**, 268-297.
18. J. M. Frost, K. L. M. Harriman and M. Murugesu, *Chem. Sci.*, 2016, **7**, 2470-2491.
19. R. Sessoli, H. L. Tsai, A. R. Schake, S. Wang, J. B. Vincent, K. Folting, D. Gatteschi, G. Christou and D. N. Hendrickson, *J. Am. Chem. Soc.*, 1993, **115**, 1804-1816.
20. A. Caneschi, D. Gatteschi, R. Sessoli, A. L. Barra, L. C. Brunel and M. Guillot, *J. Am. Chem. Soc.*, 1991, **113**, 5873-5874.
21. R. Sessoli, D. Gatteschi, A. Caneschi and M. A. Novak, *Nature*, 1993, **365**, 141-143.
22. M. Muntó, J. Gómez-Segura, J. Campo, M. Nakano, N. Ventosa, D. Ruiz-Molina and J. Veciana, *J. Mat. Chem.*, 2006, **16**, 2612-2617.
23. R. Bagai and G. Christou, *Inorg. Chem.*, 2007, **46**, 10810-10818.
24. R. Sessoli, D. Gatteschi, A. Caneschi and M. A. Novak, *Nature*, 1993, **365**, 141-143.
25. D. Ruiz-Molina, M. Mas-Torrent, J. Gómez, A. I. Balana, N. Domingo, J. Tejada, M. T. Martínez, C. Rovira and J. Veciana, *Adv. Mat.*, 2003, **15**, 42-45.
26. W. Jeon, M. Kyung Jin, Y. Kim, D.-Y. Jung, B. Jin Suh and S. Yoon, *Phys. Rev. B*, 2004, 67, 052101-052105.
27. G. Christou, D. Gatteschi, D. N. Hendrickson and R. Sessoli, *MRS Bulletin*, 2000, **25**, 66-71.
28. C. J. Milios, A. Vinslava, W. Wernsdorfer, S. Moggach, S. Parsons, S. P. Perlepes, G. Christou, E. K. Brechin and *J. Am. Chem. Soc.*, 2007, **129**, 2754-2755.
29. C. J. Milios, R. Inglis, R. Bagai, W. Wernsdorfer, A. Collins, S. Moggach, S. Parsons, S. P. Perlepes, G. Christou and E. K. Brechin, *Chem. Comm.*, 2007, **33**, 3476-3478.
30. C. J. Milios, R. Inglis, A. Vinslava, R. Bagai, W. Wernsdorfer, S. Parsons, S. P. Perlepes, G. Christou and E. K. Brechin, *J. Am. Chem. Soc.*, 2007, **129**, 12505-12511.
31. R. Inglis, L. F. Jones, C. J. Milios, S. Datta, A. Collins, S. Parsons, W. Wernsdorfer, S. Hill, S. P. Perlepes, S. Piligkos and E. K. Brechin, *Dalton Trans.*, 2009, **18**, 3403-3412.

32. T. C. Stamatatos, K. A. Abboud, W. Wernsdorfer and G. Christou, *Angew. Chem. Int. Ed.*, 2008, **47**, 6694-6698.
33. M. Murugesu, J. Raftery, W. Wernsdorfer, G. Christou and E. K. Brechin, *Inorg. Chem.*, 2004, **43**, 4203-4209.
34. M. Charalambous, E. E. Moushi, C. Papatriantafyllopoulou, W. Wernsdorfer, V. Nastopoulos, G. Christou and A. J. Tasiopoulos, *Chem. Comm.*, 2012, **48**, 5410-5412.
35. A. J. Tasiopoulos, A. Vinslava, W. Wernsdorfer, K. A. Abboud and G. Christou, *Angew. Chem. Int. Ed.*, 2004, **43**, 2117-2121.
36. O. Waldmann, *Inorg. Chem.*, 2007, **46**, 10035-10037.
37. H. L. C. Feltham and S. Brooker, *Coord. Chem. Rev.*, 2014, **276**, 1-33.
38. C. Benelli and D. Gatteschi, *Chem. Rev.*, 2002, **102**, 2369-2387.
39. S.-D. Jiang, B.-W. Wang and S. Gao, in *Molecular Nanomagnets and Related Phenomena*, ed. S. Gao, 2015, vol. 164, pp. 111-141, Springer-Verlag, Berlin.
40. N. Ishikawa, M. Sugita, T. Ishikawa, S.-y. Koshihara and Y. Kaizu, *J. Am. Chem. Soc.*, 2003, **125**, 8694-8695.
41. N. Ishikawa, M. Sugita and W. Wernsdorfer, *Angew. Chem. Int. Ed.*, 2005, **44**, 2931-2935.
42. N. Ishikawa, M. Sugita, N. Tanaka, T. Ishikawa, S.-y. Koshihara and Y. Kaizu, *Inorg. Chem.*, 2004, **43**, 5498-5500.
43. N. Ishikawa, M. Sugita, T. Ishikawa, S. Koshihara and Y. Kaizu, *J. Am. Chem. Soc.*, 2003, **125**, 8694-8695.
44. N. Ishikawa, M. Sugita, T. Ishikawa, S.-y. Koshihara and Y. Kaizu, *J. Phys. Chem. B*, 2004, **108**, 11265-11271.
45. N. Ishikawa, M. Sugita, N. Tanaka, T. Ishikawa and S. Koshihara, *Inorg. Chem.*, 2004, **43**, 5498-5500.
46. M. Gonidec, D. B. Amabilino and J. Veciana, *Dalton Trans.*, 2012, **41**, 13632-13639.
47. M. Gonidec, I. Krivokapic, J. Vidal-Gancedo, E. S. Davies, J. McMaster, S. M. Gorun and J. Veciana, *Inorg. Chem.*, 2013, **52**, 4464-4471.
48. C. R. Ganivet, B. Ballesteros, G. de la Torre, J. M. Clemente-Juan, E. Coronado and T. Torres, *Chem. Euro. J.*, 2013, **19**, 1457-1465.
49. H. Wang, B.-W. Wang, Y. Bian, S. Gao and J. Jiang, *Coord. Chem. Rev.*, 2016, **306**, 195-216.
50. P. H. Lin, T. J. Burchell, L. Ungur, L. F. Chibotaru, W. Wernsdorfer and M. Murugesu, *Angew. Chem. Int. Ed.*, 2009, **48**, 9489-9492.
51. R. J. Blagg, L. Ungur, F. Tuna, J. Speak, P. Comar, D. Collison, W. Wernsdorfer, E. J. McInnes, L. F. Chibotaru and R. E. Winpenny, *Nature Chem.*, 2013, **5**, 673-678.
52. J. Tang, I. Hewitt, N. T. Madhu, G. Chastanet, W. Wernsdorfer, C. E. Anson, C. Benelli, R. Sessoli and A. K. Powell, *Angew. Chem. Int. Ed.*, 2006, **45**, 1729-1733.
53. L. F. Chibotaru, L. Ungur and A. Soncini, *Angew. Chem. Int. Ed.*, 2008, **47**, 4126-4129.
54. J. Luzon, K. Bernot, I. J. Hewitt, C. E. Anson, A. K. Powell and R. Sessoli, *Phys. Rev. Let.*, 2008, **100**, 247205-247209.
55. A. Soncini and L. F. Chibotaru, *Phys. Rev. B*, 2008, **77**, 220406-220410.
56. N. A. Spaldin, M. Fiebig and M. Mostovoy, *J. Phys.-Cond. Mat.*, 2008, **20**, 434203-434218.
57. U. Staub, C. Piamonteze, M. Garganourakis, S. P. Collins, S. M. Koohpayeh, D. Fort and S. W. Lovesey, *Phys. Rev. B*, 2012, **85**, 144421-144428.
58. I. J. Hewitt, J. Tang, N. T. Madhu, C. E. Anson, Y. Lan, J. Luzon, M. Etienne, R. Sessoli and A. K. Powell, *Angew. Chem. Int. Ed.*, 2010, **49**, 6352-6356.
59. A. Mishra, W. Wernsdorfer, K. A. Abboud and G. Christou, *J. Am. Chem. Soc.*, 2004, **126**, 15648-15649.

60. L. Zhao, J. Wu, H. Ke and J. Tang, *Inorg. Chem.*, 2014, **53**, 3519-3525.
61. A. Mishra, W. Wernsdorfer, S. Parsons, G. Christou and E. K. Brechin, *Chem. Comm.*, 2005, **16**, 2086-2088.
62. E. M. Pineda, N. F. Chilton, F. Tuna, R. E. P. Winpenny and E. J. L. McInnes, *Inorg. Chem.*, 2015, **54**, 5930-5941.
63. J. D. Rinehart, M. Fang, W. J. Evans and J. R. Long, *Nature Chem.*, 2011, **3**, 538.
64. F. S. Guo, B. M. Day, Y. C. Chen, M. L. Tong, A. Mansikkamaki and R. A. Layfield, *Angewandte Chemie*, 2017, **56**, 11445-11449.
65. C. A. P. Goodwin, F. Ortu, D. Reta, N. F. Chilton and D. P. Mills, *Nature*, 2017, **548**, 439-442.
66. F.-S. Guo, B. Day, Y.-C. Chen, M.-L. Tong, A. Mansikkamäki and R. Layfield, *Science*, 2018, **362**, 1400-1403.

Chapter 2: $[Ni^{II}_3Ln^{III}_3]$ Triangle-in-Triangle Complexes

2.1 Introduction

In order to maximise the number of J_{LnM} exchange interactions in a molecular system whilst retaining a high level of symmetry, a number of topologies can be envisioned and studied by utilising a ligands known coordination chemistry.[1-10] For example, a previous study built upwards from an initial $[Cr^{III}_2Ln^{III}_2(bdea)_2(\mu_3\text{-}OH)_2(piv)_4(NO_3)_4]$ dimer-in-dimer (butterfly) to an intermediate $[Cr^{III}_3Ln^{III}_3(bdea)_3(\mu_3\text{-}OH)_3(\mu\text{-}X)(piv)_6(L)_3]$ (X = OH; N_3; L = Hpiv, H_2O) triangle-in-triangle, and finally to a $[Cr^{III}_4Ln^{III}_4(bdea)_4(\mu_3\text{-}OH)_4(\mu\text{-}X)_4(piv)_8]$ (X = N_3, piv, NO_3) square-in-square, employing the ligand *N*-*N*-butyldiethanolamine (H_2bdea).[11] The three different structural topologies are shown in **fig**. **1**.

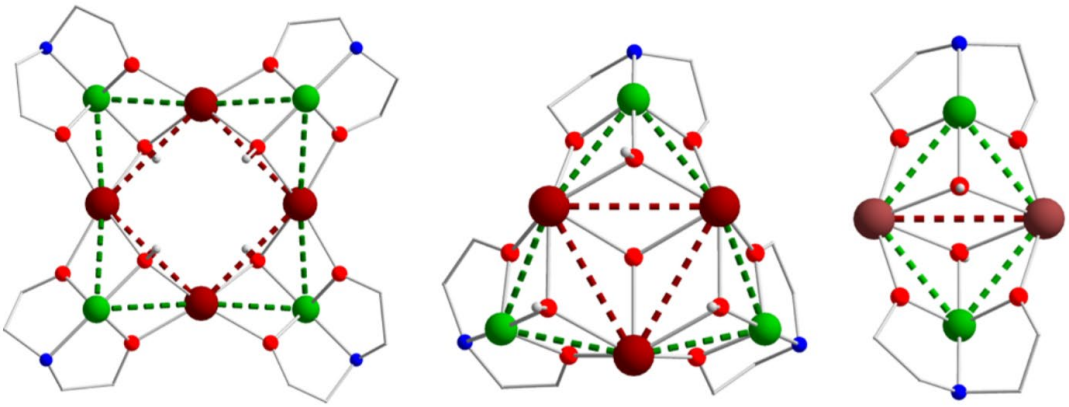

Figure 1 $[Cr^{III}_4Ln^{III}_4]$ square-in-square, $[Cr^{III}_3Ln^{III}_3]$ triangle-in-triangle and $[Cr^{III}_2Ln^{III}_2]$ butterfly topologies shown by their clusters. Colour scheme: Cr, green; Ln, maroon; O, red; N, blue.[11]

Both the $[Cr^{III}_3Ln^{III}_3]$ and $[Cr^{III}_4Ln^{III}_4]$ systems did not possess a high level of molecular symmetry with the former crystallising in the triclinic $P\bar{1}$ space-group, and the latter forming in the monoclinic space group $P2_1/n$. The magnetic data of these systems could not be fitted due to the complexity (lack of symmetry) of the topologies and none demonstrated SMM behaviour. A preceding study was published by the same group on the $[Cr^{III}_4Dy^{III}_4(\mu_3\text{-}OH)_4(\mu\text{-}N_3)_4(mdea)_4]$ system (where H_2mdea = methyldiethanolamine). This system also had a square-in-square topology but with 4-fold symmetry with the $I\bar{4}2m$ space group. This system showed magnetic hysteresis below 1.1 K with a sweep rate of 0.035 T s^{-1}.[12] Here, the static (dc) magnetic behaviour could be quantitatively rationalised. Simulations of the dc magnetic behaviour revealed a J_{DyCr} = -1.50 cm^{-1}, J_{DyDy} = 1.25 cm^{-1} and J_{CrCr} = -0.12 cm^{-1}.

Similar work has been carried out with Nickel as the 3*d* metal. In 2016, a family of 4-fold symmetric $[Ni^{II}_4Ln^{III}_4(H_3L)_4(\mu_3\text{-}OH)_4(\mu\text{-}OH)_4]$ square-in-square compounds were reported (where H_3L is a deprotonated form of H_5L = N_1, N_3-bis(6-formyl-2-(hydroxymethyl)-4-

methylphenol)diethylenetriamine). The [$Ni^{II}_4Dy^{III}_4$] analogue displayed the tails of out-of-phase ac susceptibility signals, but with no observable peaks down to T = 2 K.[13]

A series of 3-fold symmetric ($P\bar{3}c1$ space group), [$Ni^{II}_3Ln^{III}_3(\mu_3\text{-}O)(\mu_3\text{-}OH)_3(L)_3(\mu\text{-}OOCCMe_3)_3$]($ClO_4$) triangle-in-triangle complexes (where L = 6,6'-[(2-(dimethylamino)ethylazanediyl)-bis(methylene)]bis(2-methoxy-4-methylphenol) were synthesised in 2014. These complexes were magnetically characterised and the [$Ni^{II}_3Dy^{III}_3$] analogue proved to be an SMM with U_{eff} = 6.95 cm^{-1} (10 K) but did not show hysteresis at 1.8 K. Fitting of the static (dc) magnetic behaviour of the [$Ni^{II}_3Gd^{III}_3$] analogue revealed a J_{GdNi} = 0.96 cm^{-1} and J_{GdGd} = -0.18 cm^{-1}.[14]

The pro-ligand 2-(hydroxymethyl)pyridine (hmpH) has a long and successful history within the field of molecular magnetism. It has been involved in the synthesis of more than 464 3*d* complexes, with the majority containing either Manganese or Nickel, and has shown a propensity to promote ferromagnetic interactions. Despite this, the number of 3*d*-4*f* compounds made with this ligand is far less with 69 known. The structures reported in the literature include cubanes and polycubanes, with examples exhibiting SMM properties, spin frustration effects and the magnetocaloric effect.[7, 15-22] There are few examples containing Ni^{II} ions, such as the [$Ni^{II}_3Ln^{III}(hmp)_4(OAc)_5$] and [$Ni^{II}_2Ln^{III}_2(hmp)_4(PhCO_2)_5(MeOH)_2$]($ClO_4$) cubane systems which both show ferromagnetic Ni-Gd interactions.[15, 16]

Herein is reported a novel [$Ni^{II}_3Ln^{III}_3$] triangle-in-triangle family of complexes of general formula [$Ni^{II}_3Ln^{III}_3(hmp)_{12}$]($ClO_4$)$_3$, built with the pro-ligand 2-(hydroxymethyl)pyridine (hmpH), that possess 3-fold symmetry ($R\bar{3}$ space group). The syntheses, structures and magnetic properties are discussed.

2.2 Experimental

2.2.1 Materials

All reactions were carried out under aerobic conditions. Chemicals and solvents were obtained from commercial sources and used without purification.

2.2.2 Synthetic Procedures

$[Ni^{II}_3Gd^{III}_3(hmp)_{12}](ClO_4)_3 \cdot 3MeOH$ (1)

$Ni(ClO_4)_2.6H_2O$ (0.365 g, 1 mmol) and $GdCl_3.6H_2O$ (0.371 g, 1 mmol) were dissolved in a mixture of MeCN (16 mL) and MeOH (4 mL), followed by the addition of hmpH (0.47 mL, 5 mmol) and NEt_3 (0.69 mL, 5 mmol) resulting in a blue solution. The solution was stirred for 15 minutes, after which the solution was capped and left undisturbed. Within 48 hours light blue x-ray quality rod shaped crystals of **1** had formed in an approximate yield of 15%. Anal. Calculated (found) for **1**: $Ni_3Gd_3C_{72}H_{72}O_{24}N_{12}Cl_3$*: C, 38.54 (38.75); H, 3.23 (3.05); N, 7.49 (7.31); Ni, 7.85 (8.10); Gd, 21.03 (21.83)*.

$[Ni^{II}_3Tb^{III}_3(hmp)_{12}](ClO_4)_3 \cdot 3MeCN$ (2)

$Ni(ClO_4)_2.6H_2O$ (0.365 g, 1 mmol) and $Tb(NO_3)_3.6H_2O$ (0.435 g, 1 mmol) were dissolved in a mixture of MeCN (16 mL) and MeOH (4 mL), followed by the addition of hmpH (0.47 mL, 5 mmol) and NEt_3 (0.69 mL, 5 mmol), resulting in a blue solution. The solution was stirred for 15 minutes, after which the solution was capped and left undisturbed. Within 48 hours light blue x-ray quality rod shaped crystals of **2** had formed in an approximate yield of 56%. Anal. Calculated (found) for **2**: $Ni_3Tb_3C_{72}H_{72}O_{24}N_{12}Cl_3$*: C, 38.46 (38.57); H, 3.23 (3.06); N, 7.47 (7.33); Ni, 7.83 (8.06); Tb, 21.20 (21.49).

$[Ni^{II}_3Dy^{III}_3(hmp)_{12}](ClO_4)_3 \cdot 3MeCN$ (3)

$Ni(ClO_4)_2.6H_2O$ (0.365 g, 1 mmol) and $Dy(NO_3)_3.5H_2O$ (0.438 g, 1 mmol) were dissolved in a mixture of MeCN (18 mL) and MeOH (2 mL), followed by the addition of hmpH (0.47 mL, 5 mmol) and NEt_3 (0.69 mL, 5 mmol), resulting in a blue solution. The solution was stirred for 15 minutes, after which the solution was capped and left undisturbed. Within 48 hours light blue x-ray quality rod shaped crystals of **3** had formed in an approximate yield of 57%. Anal. Calculated (found) for **3**: $Ni_3Dy_3C_{78}H_{81}O_{24}N_{15}Cl_3$*: C, 38.28 (38.51); H, 3.21 (3.04); N, 7.44 (7.38); Ni, 7.79 (8.01); Dy, 21.58 (21.76).

$[Ni^{II}_3Ho^{III}_3(hmp)_{12}](ClO_4)_3 \cdot 3MeCN$ (4)

$Ni(ClO_4)_2.6H_2O$ (0.365 g, 1 mmol) and $Ho(NO_3)_3.5H_2O$ (0.441 g, 1 mmol) were dissolved in a mixture of MeCN (16 mL) and MeOH (4 mL), followed by the addition of hmpH (0.47 mL, 5 mmol) and NEt_3 (0.69 mL, 5 mmol), resulting in a blue solution. The solution was stirred for 15 minutes, after which the solution was capped and left undisturbed. Within 48 hours light blue x-ray quality rod shaped crystals of **4** had formed in an approximate yield of 50%. Anal. Calculated (found) for **4**: $Ni_3Ho_3C_{78}H_{81}O_{24}N_{15}Cl_3$*: C, 38.15 (37.86); H, 3.20 (3.02); N, 7.42 (7.32); Ni, 7.77 (8.03); Ho, 21.83 (21.64).

$[Ni^{II}_3Er^{III}_3(hmp)_{12}](ClO_4)_3 \cdot 3MeCN$ (5)

$Ni(ClO_4)_2.6H_2O$ (0.365 g, 1 mmol) and $Er(NO_3)3.5H_2O$ (0.443 g, 1 mmol) were dissolved in a mixture of MeCN (16 mL) and MeOH (4 mL), followed by the addition of hmpH (0.47 mL, 5 mmol) and NEt_3 (0.69 mL, 5 mmol), resulting in a blue solution. The solution was stirred for 15 minutes, after which the solution was capped and left undisturbed. Within 48 hours light blue x-ray quality rod shaped crystals of **5** had formed in an approximate yield of 60%. Anal. Calculated (found) for **5**: $Ni_3Er_3C_{72}H_{72}O_{24}N_{12}Cl_3$*: C, 38.03 (37.45); H, 3.19 (2.99); N, 7.39 (7.36); Ni, 7.74 (8.11); Er, 22.07 (21.87).

$[Ni^{II}_3Y^{III}_3(hmp)_{12}](ClO_4)_3 \cdot 3MeCN$ (6)

$Ni(ClO_4)_2.6H_2O$ (0.365 g, 1 mmol) and $Y(NO_3)_3.6H_2O$ (0.383 g, 1 mmol) were dissolved in a mixture of MeCN (19 mL) and MeOH (1 mL), followed by the addition of hmpH (0.47 mL, 5 mmol) and NEt_3 (0.69 mL, 5 mmol), resulting in a blue solution. The solution was stirred for 15 minutes, after which the solution was capped and left undisturbed. Within 48 hours light blue x-ray quality rod shaped crystals of **6** had formed in an approximate yield of 55%. Anal. Calculated (found) for **6**: $Ni_3Y_3C_{72}H_{72}O_{24}N_{12}Cl_3$*: C, 41.42 (41.30); H, 3.56 (3.30); N, 8.25 (8.11); Ni, 8.64 (8.77); Y, 13.08 (12.70).

*assuming the sample had fully desolvated

2.2.3 Powder Diffraction

Powder X-ray diffraction data of plate-loaded powder samples of **1**-**6** were measured on a Bruker D2 Phaser, wavelength 1.54056 Å from 5-30° 2θ (0.22° intervals) at room temperature. The experimental X-ray powder diffraction data of **1**-**6** are compared to the calculated spectra of compound **1** in **fig. 2**. The data shows that compounds **1**-**6** are analogous.

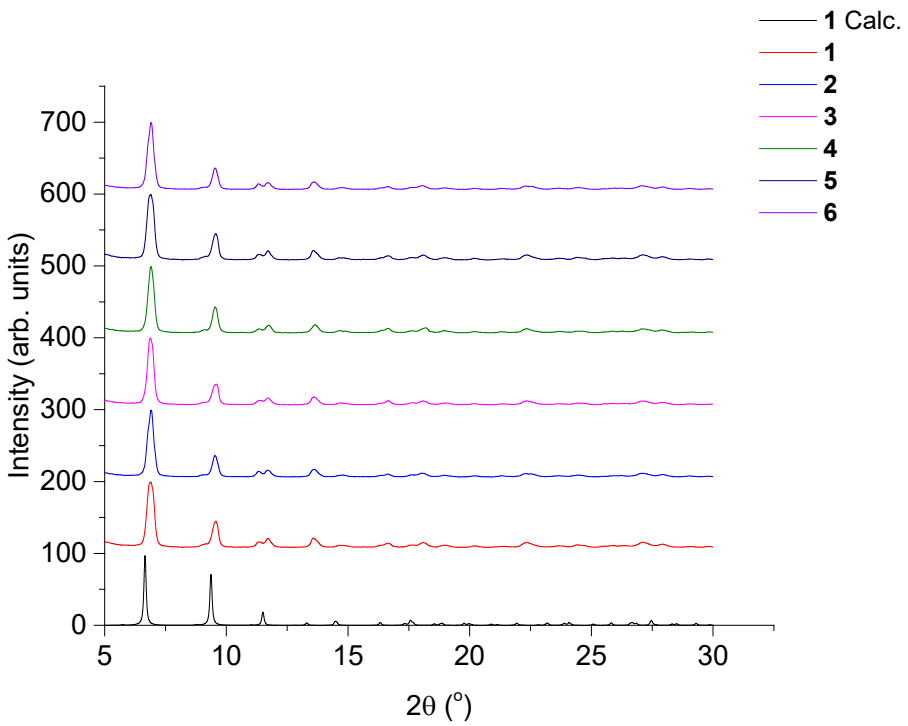

Figure 2 X-ray powder diffraction of isostructural **1**-**6** compared to the calculated pattern of **1**, 5-30° 2θ.

Table 1 Summary of crystallographic data for compounds **1**-**6**.

	1	**2**	**3**	**4**	**5**	**6**
Empirical formula	$C_{78}H_{81}Cl_3Gd_3N_{15}Ni_3O_2$	$C_{75}H_{84}Cl_3N_{12}Ni_3O_{27}Tb_3$	$C_{78}H_{81}Cl_3Dy_3N_{15}Ni_3O_{24}$	$C_{78}H_{81}Cl_3Ho_3N_{15}Ni_3O_2$	$C_{78}H_{81}Cl_3Er_3N_{15}Ni_3O_{24}$	$C_{78}H_{81}Cl_3N_{15}Ni_3O_{24}Y_3$
Formula weight	2366.8	2344.78	2382.55	2389.84	2396.83	2161.78
Temperature/ K	120.01(10)	120	120.00(10)	170	293(2)	293(2)
Crystal system	trigonal	trigonal	trigonal	trigonal	trigonal	trigonal
Space group	$R\bar{3}$	$R\bar{3}$	$R\bar{3}$	$R\bar{3}$	$R\bar{3}$	$R\bar{3}$
***a*/Å**	26.7074(3)	26.5294(5)	26.5953(4)	26.6419(15)	26.6134(3)	26.6182(3)
***b*/Å**	26.7074(3)	26.5294(5)	26.5953(4)	26.6419(15)	26.6134(3)	26.6182(3)
***c*/Å**	20.7912(3)	20.6898(4)	20.7600(3)	20.7960(11)	20.7896(4)	41.6537(10)
α/°	90	90	90	90	90	90
β/°	90	90	90	90	90	90
γ/°	120	120	120	120	120	120
Volume/Å^3	12843.2(3)	12610.8(5)	12716.5(4)	12783.3(16)	12752.0(4)	25558.9(8)
Z	6	6	6	6	6	12
ρ_{calc}g/cm^3	1.836	1.853	1.867	1.863	1.873	1.685
μ/mm^{-1}	17.05	14.472	3.443	3.58	3.758	2.848
***F*(000)**	7038	6984	7074	7092	7110	13176
Radiation	CuKα (λ = 1.54178)	CuKα (λ = 1.54184)	MoKα (λ = 0.71073)	MoKα (λ = 0.71073)	MoKα (λ = 0.71073)	MoKα (λ = 0.71073)
2Θ range for data collection/°	6.618 to 152.196	6.664 to 152.416	5.888 to 59.468	6.116 to 41.622	6.124 to 50.694	6.034 to 50.682
Goodness-of-fit on F^2	1.082	1.055	1.193	1.069	1.043	1.017
Final *R* indexes [I>=2σ(I)]	R_1 = 0.0453, wR_2 = 0.1128	R_1 = 0.0314, wR_2 = 0.0729	R_1 = 0.0373, wR_2 = 0.0783	R_1 = 0.0330, wR_2 = 0.0625	R_1 = 0.0322, wR_2 = 0.0590	R_1 = 0.0346, wR_2 = 0.0766
Final *R* indexes [all data]	R_1 = 0.0502, wR_2 = 0.1165	R_1 = 0.0368, wR_2 = 0.0756	R_1 = 0.0460, wR_2 = 0.0811	R_1 = 0.0505, wR_2 = 0.0683	R_1 = 0.0472, wR_2 = 0.0627	R_1 = 0.0553, wR_2 = 0.0838
Largest diff. peak/hole / eÅ^{-3}	0.89/-1.36	0.58/-0.70	0.71/-1.66	0.63/-0.37	0.71/-0.65	0.56/-0.45

2.2.4 Magnetic Measurements

Magnetic susceptibility and magnetization measurements were carried out on a Quantum Design MPMS XL SQUID magnetometer, and a Physical Properties Measurement System (PPMS) equipped with an ACMS option, operating in the 1.8 – 300 K and 0 – 7 T, temperature and field ranges. Microcrystalline samples were contained in a gelatine capsule and dispersed in eicosane to avoid sample movement. Diamagnetic corrections were applied to the observed paramagnetic susceptibilities using Pascal's constants.

2.3 Structural Description

Single-crystal X-ray diffraction measurements reveal that isostructural compounds of general formula $[Ni^{II}_3Ln^{III}_3(hmp)_{12}](ClO_4)_3$, **1**-**6**, crystallise in the trigonal space group R$\bar{3}$. The molecular structure and packing diagram of compound **2** are shown in **fig**. **3**. Each complex is a heterometallic hexanuclear cluster containing three (outer) Ni^{II} and three (inner) Ln^{III} ions that form a triangle-in-a-triangle metallic skeleton, with the asymmetric unit (**fig**. **3** (**a**)) containing a third of the complex (*i.e.* one Ni^{II} and one Ln^{III} ion), lying on a rotation centre.

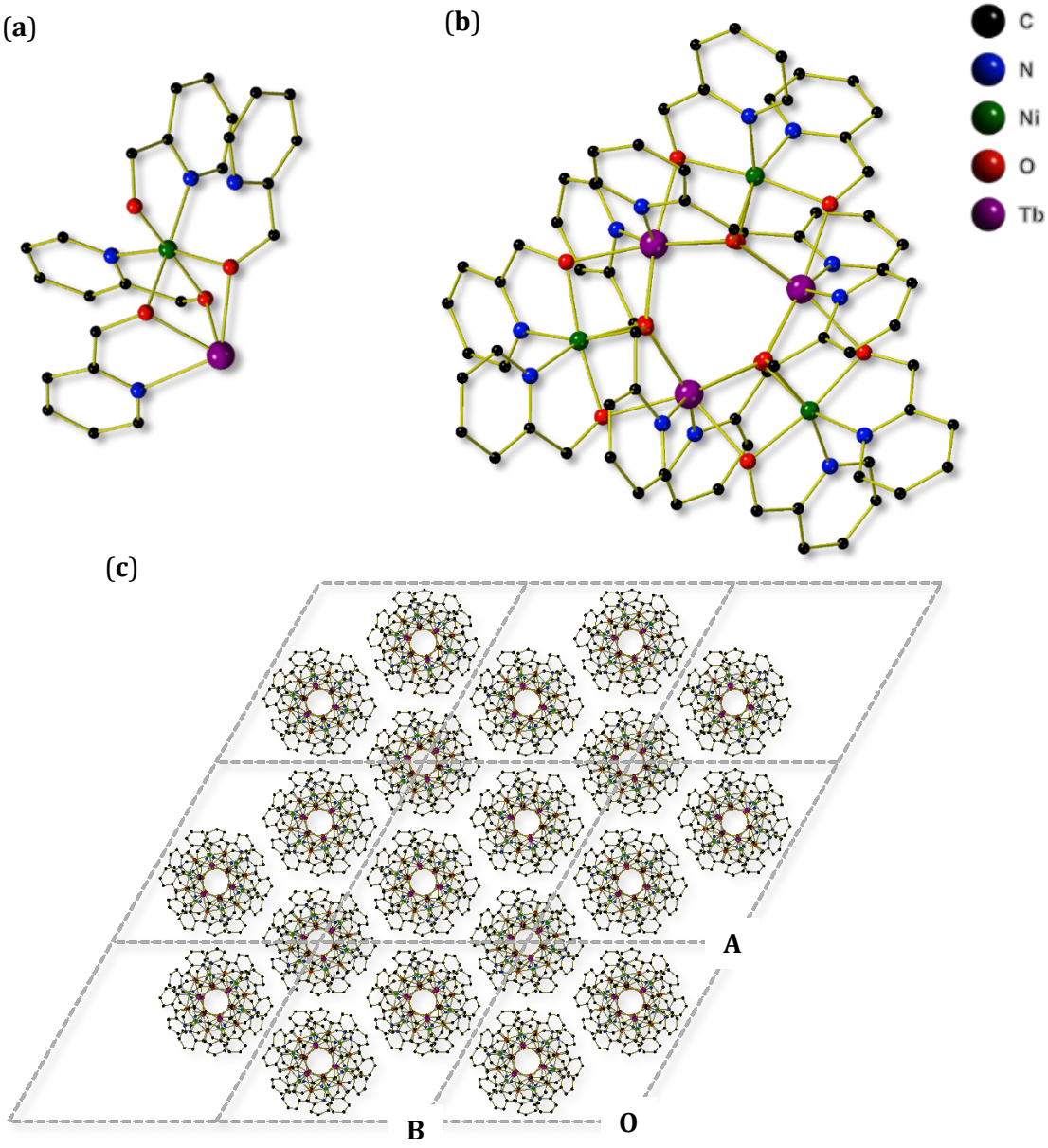

Figure 3 (**a**) The asymmetric unit of **2**. (**b**) The molecular structure of the cation in **2**. (**c**) The packing diagram of **2** viewed down the crystallographic *c*-axis. Hydrogen atoms and counter ions have been removed for clarity.

Each compound is charge balanced by three ClO_4^- ions. Each (outer) Ni^{II} ion is bridged to two (inner) Ln^{III} ions via two μ_3-O atoms of two hmp^- ligands, the N atoms of which are coordinated to the Ni^{II} ions, *i.e*. these hmp ligands are μ–bridging (**fig, 4** (**a**)). The second type of hmp ligand chelates to one (inner) Ln^{III} ion, with the O-atom of its arm further bridging to one (inner) Ln^{III} and one (outer) Ni^{II} ion, *i.e.* these μ_3–O atoms are found in the centre of the cage (**fig. 4** (**b**)).

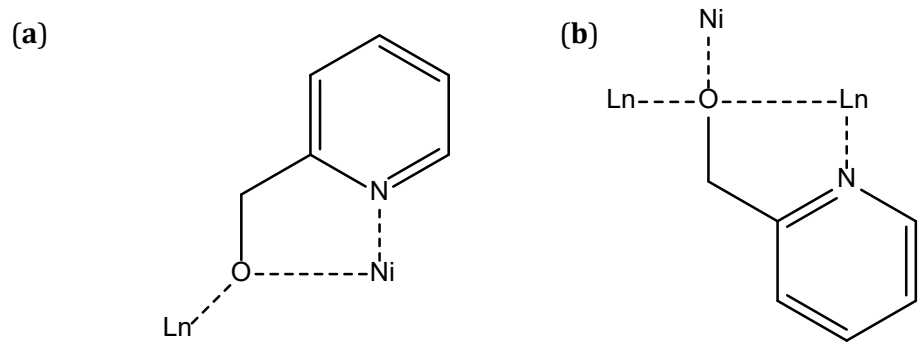

Figure 4 (**a**) μ-bridging hmp^- ligand motif. (**b**) μ_3-bridging hmp^- ligand motif.

Three MeCN(MeOH) molecules of crystallisation per complex are found within the structure of **2**-**6**(**1**). Looking down the *c*-axis there, a 3x3x2 (*a*, *b*, *c*) unit cell section is shown in **fig**. **3**(**c**), showing 3-fold symmetry in each 3x3x1 (*a*, *b*, *c*) layer.

The Ln^{III} ions as a result are eight coordinate and in distorted square antiprismatic geometry (**fig**. **4** (**b**)), determined using the SHAPE program.[23] The average Ln–(μ-O), Ln–(μ_3-O) and Ln–N bond lengths are 2.265 Å, 2.405 Å and 2.516 Å, respectively. The Ni^{II} ions in all cases are six coordinate with octahedral geometries with an average Ni-$L_{N,O}$ bond distance of 2.067 Å. **Table 2** shows selected bond distances (Å) for complexes **1**-**6** (atom assignments are shown in **fig**. **5** (**a**)).

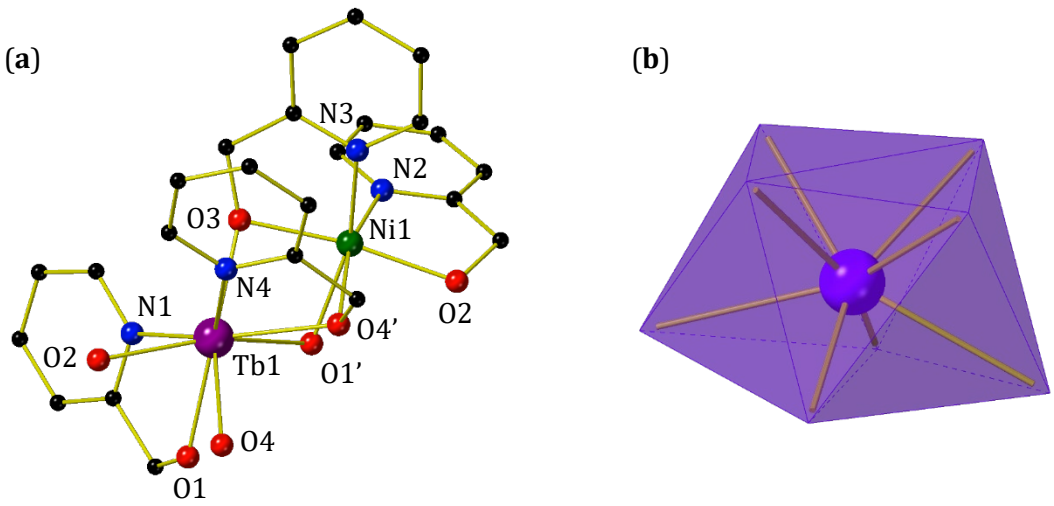

Figure 5 (**a**) Structural diagram of **1**-**6** displaying coordinating atom names (**2** shown). (**b**) Geometry of Ln^{III} ions of **1**-**6** (**2** shown).

Table 2 Selected bond distances (Å) of compounds **1**-**6**.

	1	**2**	**3**	**4**	**5**	**6**
Ln1-O1	2.381(2)	2.364(2)	2.352(3)	2.434(6)	2.411(3)	2.338(2)
Ln1-O4	2.473(2)	2.453(3)	2.350(2)	2.350(6)	2.334(3)	2.438(2)
Ln1-O1'	2.464(4)	2.452(3)	2.452(2)	2.121(4)	2.329(4)	2.424(3)
Ln1-O4'	2.385(5)	2.371(3)	2.441(4)	2.126(4)	2.420(4)	2.347(3)
Ln1-O2	2.302(4)	2.285(2)	2.271(5)	2.255(4)	2.250(4)	2.259(3)
Ln1-O3	2.304(5)	2.280(3)	2.20(1)	2.264(6)	2.252(5)	2.259(3)
Ln1-N1	2.549(4)	2.127(2)	2.524(3)	3.074(1)	2.490(4)	2.508(3)
Ln1-N4	2.544(4)	2.122(2)	2.517(3)	2.496(7)	2.500(4)	2.505(3)
Ni1-N2	2.023(5)	2.034(3)	2.06(1)	2.028(8)	2.036(6)	2.031(3)
Ni1-N3	2.030(5)	2.035(3)	2.037(5)	2.034(7)	2.033(5)	2.029(3)
Ni1-O2'	2.039(3)	2.046(3)	2.036(3)	2.014(6)	2.029(3)	2.039(2)
Ni1-O3	2.041(3)	2.035(3)	2.21(1)	2.024(7)	2.028(3)	2.038(2)
Ni1-O4	2.134(4)	2.122(2)	2.120(4)	2.121(4)	2.120(4)	2.120(3)
Ni1-O1'	2.128(4)	2.127(2)	2.125(3)	2.126(4)	2.120(4)	2.116(3)

2.4 Magnetic Studies

To probe the magnetic properties of **1**-**6**, dc magnetic susceptibility measurements were performed on microcrystalline samples in the temperature range of 2-300 K with an applied magnetic field of 0.1 T. The $\chi_M T$ versus T plots of **1**-**6** are shown in **fig**. **6**.

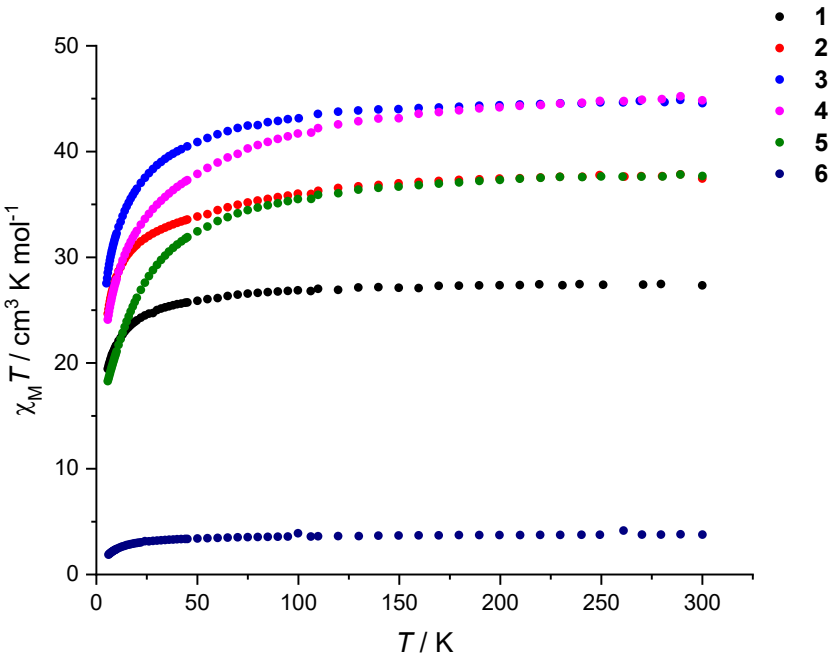

Figure 6 Plot of $\chi_M T$ versus T for **1**-**6** measured under a 0.1 T dc field.

The room temperature experimental (theoretical) $\chi_M T$ values are 27.35 (27.08), 37.45 (38.91), 44.58 (45.96), 44.84 (45.66), 37.69 (37.9) and 3.77 (3.46) cm^3 K mol^{-1} for **1**-**6** respectively. These values are in good agreement with those expected for three Ni^{II} (S = 1, g = 2.15) and three Gd^{III} ($^8S_{7/2}$, g = 2), Tb^{III} ($^7F_6$, g = 3/2), Dy^{III} ($^6H_{15/2}$, g = 4/3), Ho^{III} ($^5I_8$, g = 5/4) and Er^{III} ($^4I_{15/2}$, g = 6/5) non-interacting ions. Compounds **1**-**6** display similar profiles: between 300 and 100 K the $\chi_M T$ product stays relatively constant. Upon decreasing from 100 to 2 K the $\chi_M T$ product decreases to 19.57, 25.54, 28.52, 24.02, 18.94 and 1.76 cm^3 K mol^{-1} for **1**-**6** respectively. The nonzero $\chi_M T$ values at low temperature indicate that that in all compounds weak antiferromagnetic interactions are present. The decrease may also be due to the anisotropy associated with the nickel and lanthanide ions. For **6**, where the diamagnetic Y^{III} is present, the decrease in $\chi_M T$ is clearly due to weak AF exchange between the three Ni^{II} ions.

2.4.1 Dc Susceptibility Fitting

The $\chi_M T$ data of **1** was fitted using the program MAGFIT which block-diagonalises the spin-Hamiltonian by use of Irreducible Tensor algebra.[24] The program uses the Levenberg-Marquardt algorithm.[25] This is a spin-only fit so both Gd^{III} and Ni^{II} were assumed to be isotropic with g = 2. The exchange scheme is shown in **fig**. **7**. The best fit exchange values determined for **1** were: J_{GdGd} = -0.02 cm^{-1} and J_{GdNi} = -0.32 cm^{-1}. The experimental and best fit $\chi_M T$ plots are shown in **fig**. **8**. The spin-Hamiltonian used for this fit is given in **equation 1** below.

$$\hat{H}_{iso} = -2J_{GdGd}(\hat{S}_1\hat{S}_2 + \hat{S}_1\hat{S}_3 + \hat{S}_2\hat{S}_3) - 2J_{GdNi}(\hat{S}_1\hat{S}_4 + \hat{S}_2\hat{S}_5 + \hat{S}_2\hat{S}_4 + \hat{S}_2\hat{S}_6 + \hat{S}_3\hat{S}_5 + \hat{S}_3\hat{S}_6) + \mu_B g \sum_{i=1-6} B.\hat{S}_i \quad (1)$$

Where μ_B is the Bohr-magneton, g is the g-factor which is taken to be g = 2, B is the magnetic field vector and $\hat{S}$ is a spin operator. The energy level diagram for this fit is shown in **fig**. **9**.

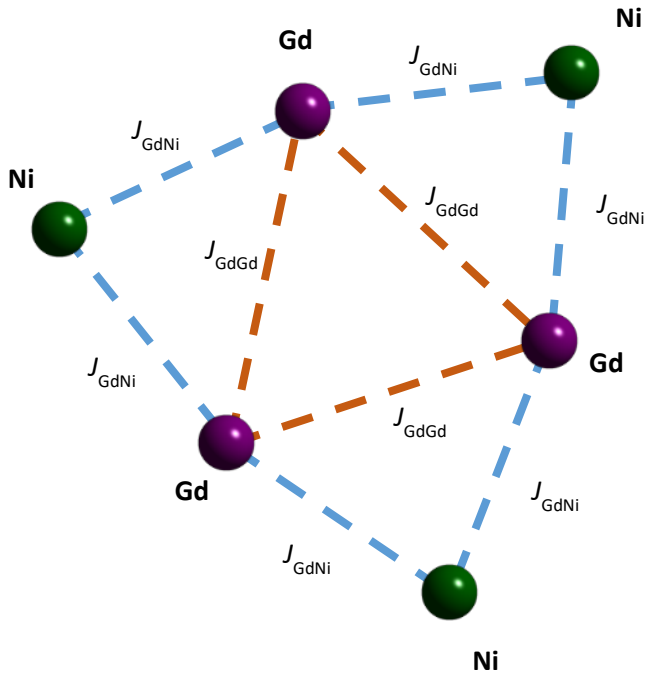

Figure 7 Exchange scheme for complex **1**.

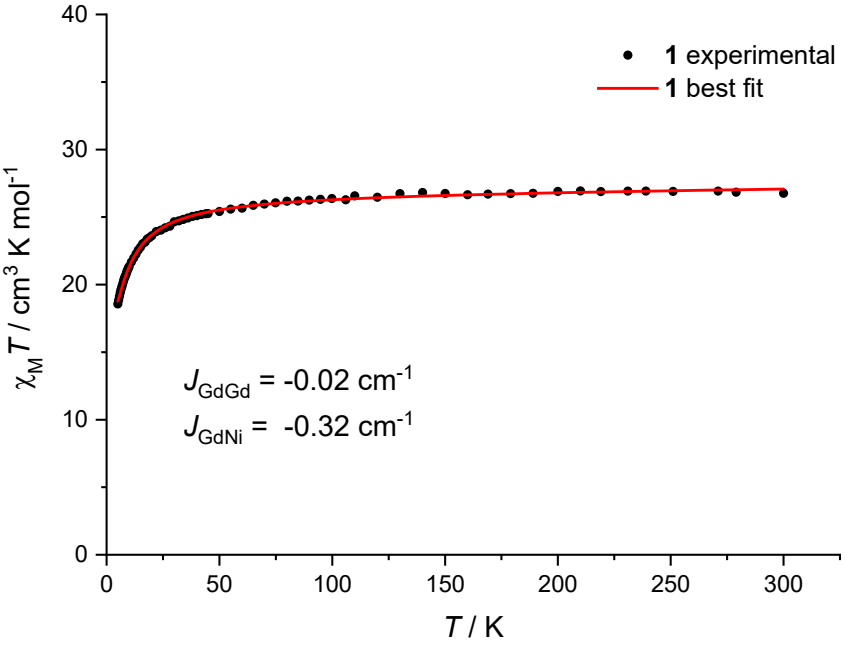

Figure 8 Plot of experimental and best fit $\chi_M T$ versus T for **1**. The experimental data points are given by the black dots and the fit employing the spin-Hamiltonian in **equation 1** is the solid red line.

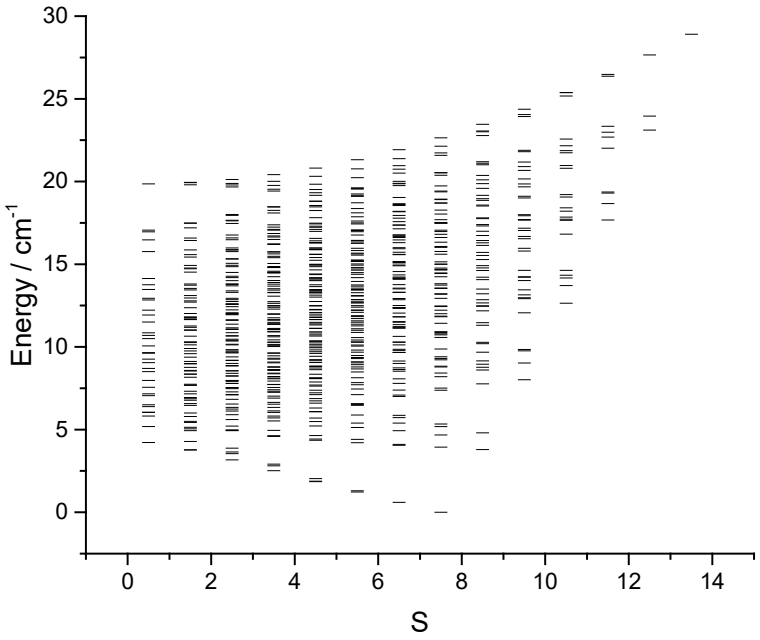

Figure 9 Energy level diagram for spin-only exchange interactions for compound **1**.

The energy level diagram shows the S = 15/2 ground state and first excited state S = 13/2 with a 0.597 cm^{-1} energy gap, showing that the ground state is not well isolated. Up to 30 cm^{-1} there are a vast number of energy levels without accounting for the anisotropy of the Ni^{II} ion, thus resulting in many additional relaxation pathways via QTM or TA-QTM.

2.4.2 Ac Susceptibility Measurements

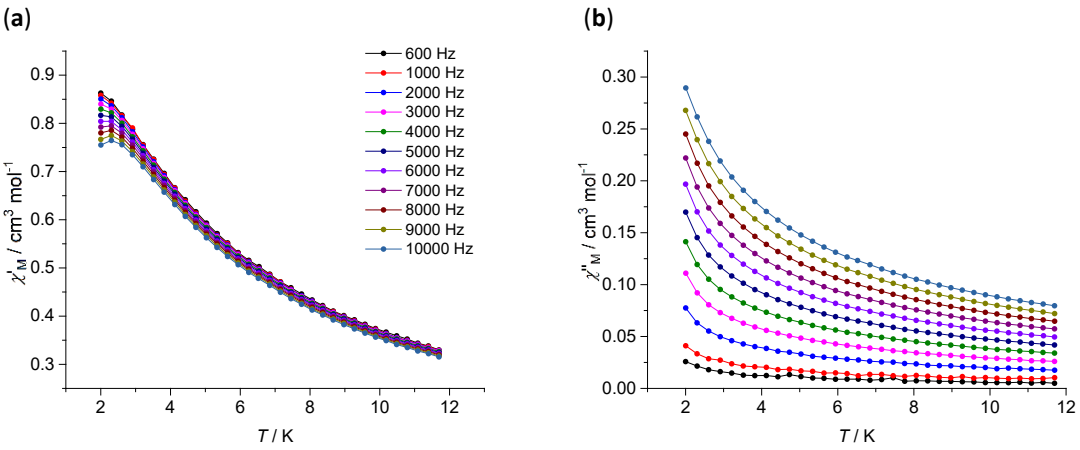

Figure 10 Dynamic Behaviour of **2**. (**a**) In-phase ac susceptibility (χ_M') from 2-11.75 K and 600-10000 Hz. (**b**) Out-of-phase ac susceptibility (χ_M'') from 2-11.75 K and 600-10000 Hz. Lines are a visual guide.

Out-of-phase ac susceptibility measurements from 600-10000 Hz show tails going below 2 K. It is not evident from this data whether there is any frequency dependence. Compound **2** is the only analogue of the family that shows any dynamic behaviour, indicating that its origin may be the single-ion magnet (SIM) properties of the Tb^{III} ion. The increase in the number of potential relaxation pathways due to the J_{GdGd} and J_{GdNi} exchange interactions calculated could result in the lack of significant SMM behaviour, as has been observed in numerous previous studies.[1, 26] The influence of *d-f* and *f-f* exchange interactions can be proven via the synthesis of family members containing diamagnetic 3*d* metals, thus removing the 3*d*-4*f* exchange interactions. This systematic approach is highly effective and can give a direct measure of the effect these exchange interactions have on U_{eff}. Unfortunately, it was not possible to synthesise the [$M^{II}_3Ln^{III}_3$] (where M = diamagnetic transition metal) analogues of this system and thus any discussion of the effect of the exchange interactions would be entirely speculative. **Chapters 3** and **4** probe these effects in more detail.

2.5 Discussion

The examples discussed in the introduction (**section 2.1**) represent all examples of 3*d*-4*f* structures with similar topologies to the family investigated in the literature. From these studies it appears that high symmetry is required to achieve SMM behaviour regardless of ligands involved as only those with their space group symmetry reflecting the internal symmetry of the molecule manifested SMM behaviour.[11-14] Simulation of the dc magnetic behaviour data of $[Cr^{III}_4Dy^{III}_4(\mu_3\text{-}OH)_4(\mu\text{-}N_3)_4(mdea)_4]$ system which exhibited hysteresis at 1.1 K revealed a J_{DyCr} = -1.5 cm^{-1} and J_{DyDy} = 1.25 cm^{-1}.[12] This is a simulation and is based on the dc behaviour of anisotropic Dy^{III} ions, therefore, this value may not be representative of the actual value. Fitting of static dc magnetic behaviour of the $[Ni^{II}_3Ln^{III}_3(\mu_3\text{-}O)(\mu_3\text{-}OH)_3(L)_3(\mu\text{-}OOCCMe_3)_3](ClO_4)$ system revealed a J_{GdNi} = 0.96 cm^{-1} and J_{GdGd} = -0.18 cm^{-1}, the $[Ni_3Dy_3]$ analogue of which showed a U_{eff} = 6.95 cm^{-1} (10 K).[14] Comparing these *J* values with those obtained for **1** ($[Ni^{II}_3Gd^{III}_3(hmp)_{12}](ClO_4)_3\cdot 3MeOH$), J_{GdNi} = -0.32 cm^{-1} and J_{GdGd} = -0.02 cm^{-1}, show a marked change. The J_{GdNi} interaction has switched from ferromagnetic to slightly weaker antiferromagnetic exchange, while J_{GdGd} has decreased in strength to almost zero. This could be due to slight changes in the local crystal field parameters due to changes in electronegativity in the ligand sphere as the molecules described here only contains hmp^- ligands whereas the molecule described in the literature contains oxides, hydroxides and carboxylates.[27] Quantitative comparison cannot be given with the analysis available but this change in donor-acceptor nature of the ligands may change their interactions with the 4*f* shell of the lanthanide ions which could change nature of their anisotropy (shape and direction). Computational analysis may afford clarity on these speculations.

As only tails are seen in the ac susceptibility data of **2** ($[Ni^{II}_3Tb^{III}_3(hmp)_{12}](ClO_4)_3\cdot 3MeCN$) in this study it can be hypothesised that within these topologies stronger magnetic interactions can result in improved SMM behaviour. Nevertheless, the effect of numerous parameters not accounted for such as the ligand field, geometry and single-ion environment of the Ln^{III} ions may have a greater impact on these properties and these studies limit the understanding of these parameters.

2.6 Conclusion

Compounds **1**-**6**, with the general formula $[Ni^{II}_3Ln^{III}_3(hmp)_{12}](ClO_4)_3$ and possessing a highly symmetric triangle-in-triangle metal topology, were synthesised and magnetically characterised. Magnetic susceptibility measurements performed on microcrystalline samples in the temperature range 2-300 K revealed that antiferromagnetic interactions were present in compounds **1**-**6**. MAGFIT was employed to fit the experimental susceptibility data for the $[Ni^{II}_3Gd^{III}_3]$ complex (**1**); with the best fit parameters being J_{GdGd} = -0.02 cm^{-1} and J_{GdNi} = -0.32 cm^{-1}. Complex **2**, $[Ni^{II}_3Tb^{III}_3]$, showed out-of-phase ac susceptibility signals, but no peaks were observed above 2 K. **2** is therefore likely to be an SMM, but with a small energy barrier to the relaxation of the magnetization, which may be due to the large number of potential relaxation pathways induced by the J_{LnLn} and J_{LnNi} exchange interactions.

2.7 References

1. A. B. Canaj, D. I. Tzimopoulos, M. Siczek, T. Lis, R. Inglis and C. J. Milios, *Inorg. Chem.*, 2015, **54**, 7089-7095.
2. M. A. Palacios, E. Moreno Pineda, S. Sanz, R. Inglis, M. B. Pitak, S. J. Coles, M. Evangelisti, H. Nojiri, C. Heesing, E. K. Brechin, J. Schnack and R. E. Winpenny, *Chem. Phys. Chem.*, 2016, **17**, 55-60.
3. Z.-L. Wu, Y.-G. Ran, X.-Y. Wu, Y.-P. Xia, M. Fang and W.-M. Wang, *Polyhedron*, 2017, **126**, 282-286.
4. D. I. Alexandropoulos, L. Cunha-Silva, G. Lorusso, M. Evangelisti, J. Tang and T. C. Stamatatos, *Chem. Comm.*, 2016, **52**, 1693-1696.
5. S. K. Langley, D. P. Wielechowski, N. F. Chilton, B. Moubaraki and K. S. Murray, *Inorg. Chem.*, 2015, **54**, 10497-10503.
6. S. K. Langley, L. Ungur, N. F. Chilton, B. Moubaraki, L. F. Chibotaru and K. S. Murray, *Inorg. Chem.*, 2014, **53**, 4303-4315.
7. T. N. Hooper, J. Schnack, S. Piligkos, M. Evangelisti and E. K. Brechin, *Angew. Chem. Int Ed.*, 2012, **51**, 4633-4636.
8. C. Aronica, G. Pilet, G. Chastanet, W. Wernsdorfer, J. F. Jacquot and D. Luneau, *Angew. Chem. Int Ed.*, 2006, **45**, 4659-4662.
9. K. Griffiths, P. Kumar, J. D. Mattock, A. Abdul-Sada, M. B. Pitak, S. J. Coles, O. Navarro, A. Vargas and G. E. Kostakis, *Inorg. Chem.*, 2016, **55**, 6988-6994.
10. H. H. Zou, L. B. Sheng, F. P. Liang, Z. L. Chen and Y. Q. Zhang, *Dalton Trans.*, 2015, **44**, 18544-18552.
11. J. Rinck, Y. Lan, C. E. Anson and A. K. Powell, *Inorg. Chem.*, 2015, **54**, 3107-3117.
12. J. Rinck, G. Novitchi, W. Van den Heuvel, L. Ungur, Y. Lan, W. Wernsdorfer, C. E. Anson, L. F. Chibotaru and A. K. Powell, *Angew. Chem. Int. Ed.*, 2010, **49**, 7583-7587.
13. S. Biswas, J. Goura, S. Das, C. V. Topping, J. Brambleby, P. A. Goddard and V. Chandrasekhar, *Inorg. Chem.*, 2016, **55**, 8422-8436.
14. J. Goura, R. Guillaume, E. Riviere and V. Chandrasekhar, *Inorg. Chem.*, 2014, **53**, 7815-7823.
15. P. Wang, S. Shannigrahi, N. L. Yakovlev and T. S. Hor, *Dalton Trans.*, 2014, **43**, 182-187.
16. W. R. Yu, G. H. Lee and E. C. Yang, *Dalton Trans.*, 2013, **42**, 3941-3949.
17. J. L. Liu, W. Q. Lin, Y. C. Chen, S. Gomez-Coca, D. Aravena, E. Ruiz, J. D. Leng and M. L. Tong, *Chem. Euro. J.*, 2013, **19**, 17567-17577.
18. J. Feuersenger, D. Prodius, V. Mereacre, R. Clérac, C. E. Anson and A. K. Powell, *Polyhedron*, 2013, **66**, 257-263.
19. P. Wang, S. Shannigrahi, N. L. Yakovlev and T. S. Hor, *Inorg. Chem.*, 2012, **51**, 12059-12061.
20. C. Papatriantafyllopoulou, K. A. Abboud and G. Christou, *Inorg. Chem.*, 2011, **50**, 8959-8966.
21. J. Feuersenger, D. Prodius, V. Mereacre, R. Clérac, C. E. Anson and A. K. Powell, *Inorg. Chem. Comm.*, 2011, **14**, 1851-1854.
22. F. He, M.-L. Tong and X.-M. Chen, *Inorg. Chem.*, 2005, **44**, 8285-8292.
23. M. Llunell, D. Casanova, J. Cirera, P. Alemany and S. Alvarez, *SHAPE, Version 2.0*, 2010.
24. A. Bencini and D. Gatteschi, *Electron Paramagnetic Resonance of Exchange Coupled Systems*, *Springer-Verlag*, Berlin, 1990, pp. 287.
25. W. H. Press, S. A. Teukolsky, W. T. Vetterling and B. P. Flannery, *Cambridge University Press*, 1992.

26. T. D. Pasatoiu, A. Ghirri, A. M. Madalan, M. Affronte and M. Andruh, *Dalton Trans.*, 2014, **43**, 9136-9142.
27. V. Mereacre, A. Baniodeh, C. E. Anson and A. K. Powell, *J. Am. Chem. Soc.*, 2011, **133**, 15335-15337.

Chapter 3: $[M^{II}_2Ln^{III}_2]$ Butterfly Complexes

3.1 Introduction

The previous chapter showed that exchange interactions may have a negative impact upon the magnetisation relaxation behaviour of $[Ni^{II}_3M^{III}_3(hmp)_{12}](ClO_4)_3\cdot 3MeCN$, since no SMM behaviour was evident above T = 2 K. However, since no diamagnetic 3*d* metals could be incorporated, a detailed study was not possible. The molecules discussed in this chapter are 3*d*-4*f* heterometallic complexes that all possess 'butterfly' or 'diamond-like' $[M^{II}_2Ln^{III}_2]$ topologies (**fig**. **1**). Two different structure types, namely $[M^{II}_2Ln^{III}_2(hmp)_6(NO_3)_4(MeCN)_2]\cdot MeOH$ and $[M^{II}_2Ln^{III}_2(mhmp)_6(NO_3)_4]\cdot MeCN$ (where M = Ni, Zn; Ln = Gd, Tb, Dy, Y; hmpH = 2-(hydroxymethyl)pyridine and mhmpH = 6-methyl-2-(hydroxymethyl)pyridine), possessing different magnetic properties, have been investigated. In each family the Ni^{II} ions have be replaced with Zn^{II} ions, and the Ln^{III} ions replaced with Y^{III} ions in order to probe the $J_{M\text{-}M}$ and $J_{Ln\text{-}M}$ exchange interactions individually.[1] Best fits to dc magnetic susceptibility data reveal that the typical J_{LnNi} interactions are in the range $-|2-5|$ cm^{-1}, with the majority being ferromagnetic in nature.[2-25] A number of previously published $[Ni_xDy_x]$ complexes with similar structures (and exchange coupling constants) have been shown to display frequency dependent behaviour in ac susceptibility studies below 7 K.[9, 10, 15-17, 19, 21, 26] Perhaps the most pertinent example is the compound $[Ni^{II}_2Dy^{III}_2L_{10}(bipy)_2]$ (where L^- = 3, 5-dichlorobenzoate) which has U_{eff} = 73 cm^{-1}.[27]

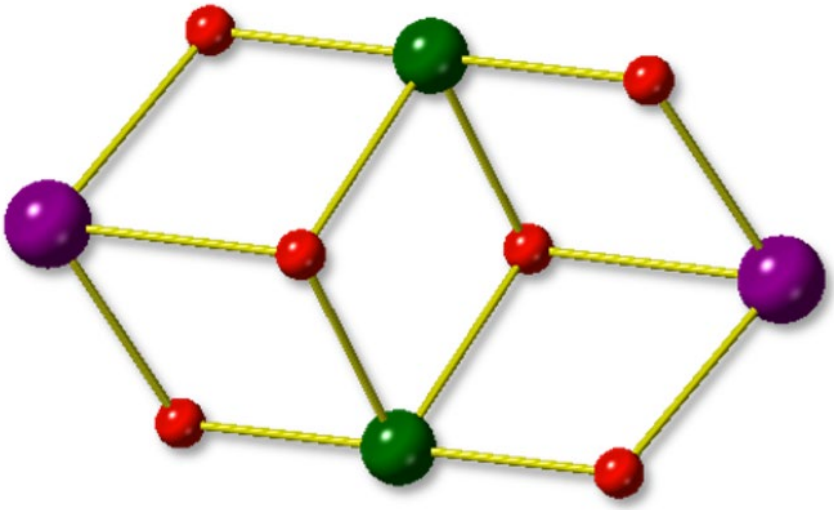

Figure 1 The core common to all the $[M^{II}_2Ln^{III}_2]$ complexes reported in this chapter, where the inner M^{II} ions (green) represent the 'body' and the outer Ln^{III} ions (purple) the 'wings' of a butterfly. Colour scheme: Purple – Ln^{III} ion; Green – M^{II} ion; Red – oxygen.

3.2 Experimental

3.2.1 Materials

All reactions were carried out under aerobic conditions. Chemicals and solvents were obtained from Sigma Aldrich and Alfa Aesar and used without further purification.

3.2.2 Synthetic Procedures

$[Ni^{II}_2Gd^{III}_2(hmp)_6(NO_3)_4(MeCN)_2]\cdot MeOH$ (1)

$NiBr_2$ (0.218 g, 1 mmol) and $Gd(NO_3)_3\cdot 6H_2O$ (0.451 g, 1 mmol) were dissolved in a mixture of MeCN (12 mL) and MeOH (8 mL), followed by the addition of hmpH (0.47 mL, 5 mmol) and NEt_3 (0.69 mL, 5 mmol) resulting in a brown/green solution. The solution was stirred for 1 hour before being filtered to isolate a green/blue solution. The solution was then layered with diethyl ether (Et_2O) via vapour diffusion. After 48 hours, light green/blue block shaped crystals of **1** had appeared, with an approximate yield of 62%. Elemental analysis calculated (found) for **1**: $Ni_2Gd_2C_{40}H_{42}N_{12}O_{18}$*: C, 33.60 (33.78); H, 3.00 (2.98); N, 11.91 (11.85); Ni, 8.32 (8.25); Gd, 22.29 (22.16).

$[Ni^{II}_2Tb^{III}_2(hmp)_6(NO_3)_4(MeCN)_2]\cdot MeOH$ (2)

The synthesis of **1** was followed, but with $Tb(NO_3)_3\cdot 6H_2O$ (0.435 g, 1 mmol) used in place of $Gd(NO_3)_3\cdot 6H_2O$. After 48 hours light green/blue block shaped crystals of **2** had appeared, with an approximate yield of 41%. Elemental analysis calculated (found) for **2**: $Ni_2Tb_2C_{40}H_{42}N_{12}O_{18}$*: C, 33.97 (33.91); H, 2.99 (2.97); N, 11.89 (11.84); Ni, 8.30 (8.24); Tb, 22.48 (22.52).

$[Ni^{II}_2Dy^{III}_2(hmp)_6(NO_3)_4(MeCN)_2]\cdot MeOH$ (3)

The synthesis of **1** was followed, but with $Dy(NO_3)_3\cdot 6H_2O$ (0.438 g, 1 mmol) used in place of $Gd(NO_3)_3\cdot 6H_2O$. After 48 hours light green/blue block shaped crystals of **3** had appeared, with an approximate yield of 65%. Elemental analysis calculated (found) for **3**: $Ni_2Dy_2C_{40}H_{42}N_{12}O_{18}$*: C, 33.80 (33.85); H, 2.98 (2.93); N, 11.83 (11.85); Ni, 8.26 (8.23); Dy, 22.87 (22.90).

$[Ni^{II}_2Y^{III}_2(hmp)_6(NO_3)_4(MeCN)_2]\cdot MeOH$ (4)

The synthesis of **1** was followed, but with $Y(NO_3)_3\cdot 6H_2O$ (0.383 g, 1 mmol) used in place of $Gd(NO_3)_3\cdot 6H_2O$. After 48 hours light green/blue block shaped crystals of **4** had appeared, with an approximate yield of 58%. Elemental analysis calculated (found) for **4**: $Ni_2Y_2C_{40}H_{42}N_{12}O_{18}$*: C, 37.71 (37.60); H, 3.32 (3.28); N, 13.19 (13.11); Ni, 9.21 (9.23); Y, 13.96 (13.91).

$[Zn^{II}_2Gd^{III}_2(hmp)_6(NO_3)_4(MeCN)_2]\cdot MeOH$ (5)

The synthesis of **1** was followed, but with $ZnBr_2$ (0.225 g, 1 mmol) used in place of $NiBr_2$. After 48 hours colourless block shaped crystals of **5** had appeared, with an approximate yield of 54%. Elemental analysis calculated (found) for **5**: $Zn_2Gd_2C_{40}H_{42}N_{12}O_{18}$*: C, 33.74 (33.67); H, 2.97 (2.98); N, 11.80 (11.77); Zn, 9.18 (9.21); Gd, 22.08 (22.06).

$[Zn^{II}_2Tb^{III}_2(hmp)_6(NO_3)_4(MeCN)_2]\cdot MeOH$ (6)

The synthesis of **2** was followed, but $ZnBr_2$ (0.225 g, 1 mmol) used in place of $NiBr_2$. After 48 hours colourless block shaped crystals of 6 had appeared, with an approximate yield of 59%. Elemental analysis calculated (found) for **6**: $Zn_2Tb_2C_{40}H_{42}N_{12}O_{18}$*: C, 33.66 (33.62); H, 2.97 (2.99); N, 11.77 (11.72); Zn, 9.16 (9.20); Tb, 22.27 (22.24).

$[Zn^{II}_2Dy^{III}_2(hmp)_6(NO_3)_4(MeCN)_2]\cdot MeOH$ (7)

The synthesis of **3** was followed, but with $ZnBr_2$ (0.225 g, 1 mmol) used in place of $NiBr_2$. After 48 hours colourless block shaped crystals of **7** had appeared, with an approximate yield of 68%. Elemental analysis calculated (found) for **7**: $Zn_2Dy_2C_{40}H_{42}N_{12}O_{18}$*: C, 33.49 (33.51); H, 2.95 (2.96); N, 11.72 (11.75); Zn, 9.12 (9.09); Dy, 22.65 (22.67).

$[Ni^{II}_2Gd^{III}_2(mhmp)_6(NO_3)_4]\cdot MeCN$ (8)

$Ni(ClO_4)_2\cdot 6H_2O$ (0.5 mmol, 0.182 g), $Gd(NO_3)_3\cdot 6H_2O$ (0.5 mmol, 0.225 g) and mhmpH (2.5 mmol, 0.307 g) were dissolved in a mixture of MeOH (12 mL) and MeCN (8 mL), followed by the addition of NEt_3 (2.5 mmol, 0.345 mL) forming a green/blue solution. The solution was stirred for 1 hour before being filtered. The solution was then layered with diethyl ether (Et_2O) via vapour diffusion. After 48 hours blue/green block shaped crystals of **8** had appeared, with an approximate yield of 5.2%. Elemental analysis calculated (found) for **8**: $Ni_2Gd_2C_{42}H_{48}N_{10}O_{18}$*: C, 35.71 (35.72); H, 3.42 (3.45); N, 9.91 (9.92); Ni, 8.31 (8.29); Gd, 22.26 (22.24).

$[Ni^{II}_2Dy^{III}_2(mhmp)_6(NO_3)_4]\cdot MeCN$ (9)

The synthesis of **8** was followed, but with $Dy(NO_3)_3\cdot 6H_2O$ (0.219 g, 0.5 mmol) in place of $Gd(NO_3)_3\cdot 6H_2O$. After 48 hours light green/blue block shaped crystals of **9** had appeared, with an approximate yield of 6.7%. Elemental analysis calculated (found) for **9**: $Ni_2Dy_2C_{42}H_{48}N_{10}O_{18}$*: C, 35.44 (35.48); H, 3.40 (3.44); N, 9.84 (9.82); Ni, 8.25 (8.21); Dy, 22.83 (22.84).

$[Ni^{II}_2Y^{III}_2(mhmp)_6(NO_3)_4]\cdot MeCN$ (10)

The synthesis of **8** was followed, but with $Y(NO_3)_3\cdot 6H_2O$ (0.191 g, 0.5 mmol) used in place of $Gd(NO_3)_3\cdot 6H_2O$. After 48 hours light green/blue block shaped crystals of **10** had appeared, with an approximate yield of 7.7%. Elemental analysis calculated (found) for **13**: $Ni_2Y_2C_{42}H_{48}N_{10}O_{18}$*: C, 39.53 (39.55); H, 3.79 (3.77); N, 10.98 (10.96); Ni, 9.20 (9.16); Y, 13.93 (13.98).

$[Zn^{II}_2Dy^{III}_2(mhmp)_6(NO_3)_4]\cdot MeCN$ (11)

The synthesis of **9** was followed, but with $Zn(ClO_4)_2\cdot 6H_2O$ (0.186 g, 0.5 mmol) used in place of $Ni(ClO_4)_2\cdot 6H_2O$. After 48 hours colourless block shaped crystals of **11** had appeared, with an approximate yield of 8.6%. Elemental analysis calculated (found) for **11**: $Zn_2Dy_2C_{42}H_{48}N_{10}O_{18}$*: C, 35.11 (35.08); H, 3.37 (3.39); N, 9.75 (9.78); Zn, 9.10 (9.12); Dy, 22.62 (22.59).

*assuming the sample had fully desolvated

3.2.3 Crystallography

A suitable crystal of each complex was selected and mounted on a MITIGEN holder in Paratone oil on an Agilent Technologies SuperNova diffractometer. A MoKα source was used for **2**, **4**, **8**, **9** and **11** and a CuKα source was used for **1**, **3**, **5**-**7** and **10**. The crystals were kept at *T* = 120.0 K, with the exception of **9** which was kept at 150 K. Using Olex2, the structure was solved with the ShelXT structure solution program, using Direct Methods.[28, 29] The models were refined with ShelXL using Least Squares minimisation.[28] Crystallographic data and refinement parameters for **1**-**4**, **5**-**7** and **8**-**11** are summarised in **Tables S1-3** respectively.

3.2.4 Powder X-ray Diffraction

The X-ray powder diffraction data of plate loaded powder samples of **1**-**11** were measured on a Bruker D2 Phaser, wavelength 1.54056 Å from 5-30° 2θ (0.22° intervals) at room temperature. The experimental X-ray powder diffraction data of **1**-**7** were compared to the calculated spectrum of **1**, shown in **fig**. **2**. The experimental X-ray powder diffraction data of **8**-**11** were compared to the calculated spectrum of **8**, shown in **fig**. **3**.

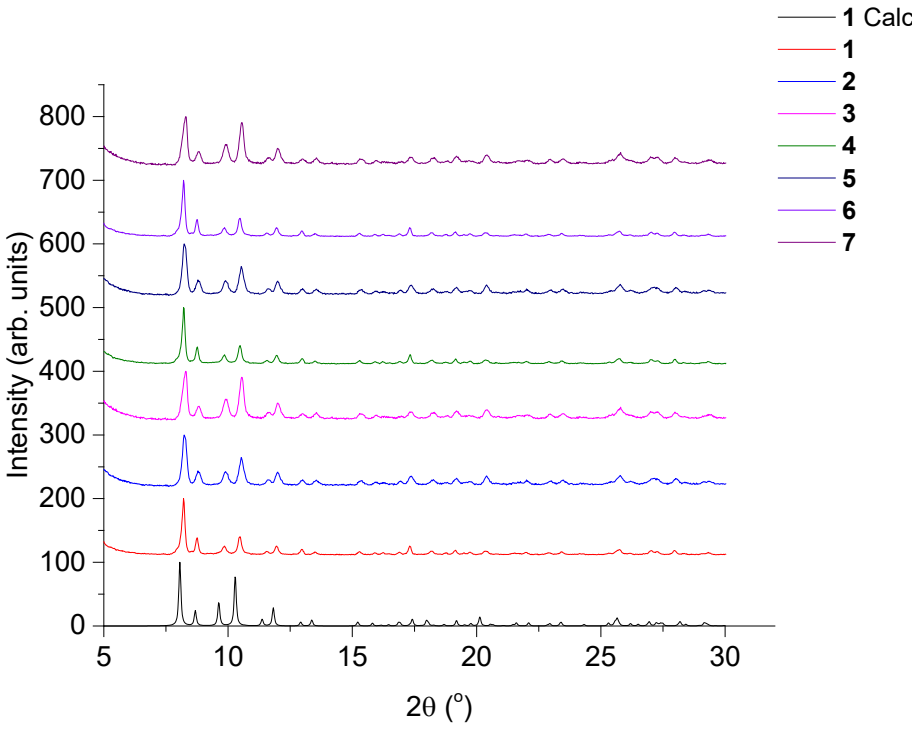

Figure 2 X-ray powder diffraction of isostructural compounds **1**-**7** compared to the calculated pattern of **1**, 5-30° 2θ.

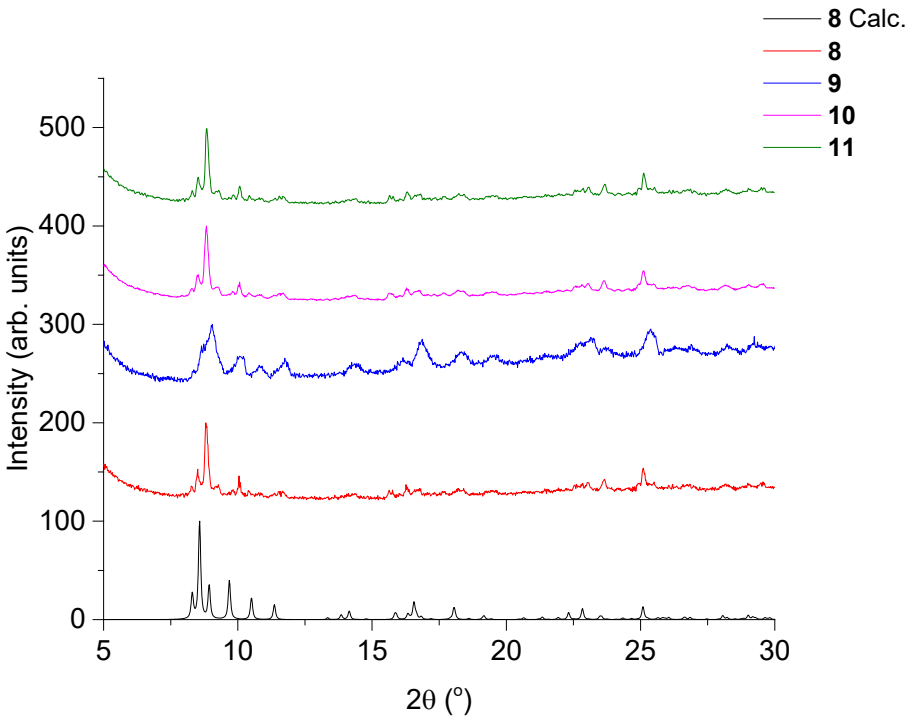

Figure 3 X-ray powder diffraction of isostructural compounds **8**-**11** compared to the calculated pattern of **8**, 5-30° 2θ.

3.2.5 Magnetic studies

Dc/ac magnetic susceptibility and magnetization measurements were carried out on a Quantum Design SQUID magnetometer and a PPMS magnetometer with an ACMS option operating in the 1.8-300 K and 0-7 T temperature and field ranges, respectively. Ac susceptibility frequency measurement ranges for the MPMS and PPMS are 0.5-1000 Hz and 1000-10000 Hz, respectively. In-phase (χ_M') and out-of-phase (χ_M'') ac susceptibility measurements were carried out and plotted as a function of temperature and frequency. Microcrystalline samples were contained in a gelatine capsule and dispersed in eicosane to avoid sample movement. Diamagnetic corrections were applied to the observed paramagnetic susceptibilities using Pascal's constants.

3.3 Results and discussion

3.3.1 Structural descriptions

Single crystal X-ray diffraction measurements reveal that the isostructural compounds **1**-**7** crystallise in the monoclinic space group $P2_1/n$ and **8**-**11** crystallise in the monoclinic $C2/c$ space group. The molecular structures of representative **7** and **11** are shown in **fig**. **4**.

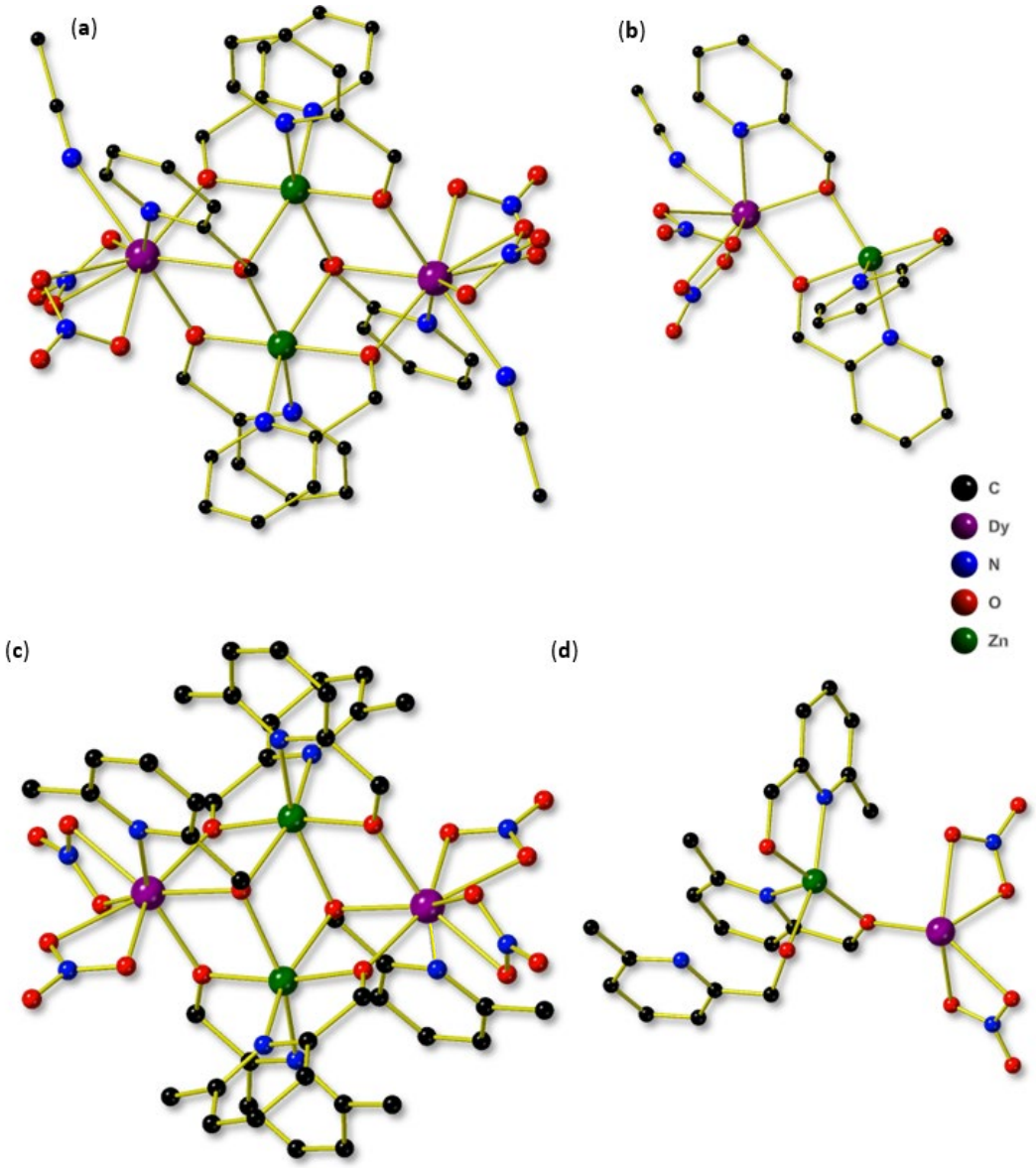

Figure 4 (**a**) Molecular structure of **7**. (**b**) Asymmetric unit (ASU) of **7**. (**c**) Molecular structure of **11**. (**d**) ASU of **11**. Solvent molecules of crystallisation have been omitted for clarity. Colour code is given in the inset of the figure.

Each complex is a heterometallic tetranuclear cluster containing two M^{II} ions (Ni^{II} for **1**-**4**, **8**-**10**; Zn^{II} for **5**-**7**, **10** and **11**) and two Ln^{III} ions, with half of the complex (one M^{II} and one Ln^{III}

ion) in the ASU, with the inversion centre lying midway between the M^{II} ions. This is a common structural topology in 3d/4f chemistry, often referred to as a 'butterfly', where the M^{II} ions occupy the 'body' positions and the Ln^{III} ions the 'wings' of the butterfly. Compounds **1**-**7** (referred to herein as *BF1*) and **8**-**11** (*BF2*) are structurally similar, the differences originating from the use of two slightly different ligands, 2-(hydroxymethyl)pyridine (hmpH) and 6-methyl-2-(hydroxymethyl)pyridine (mhmpH). In particular, the methyl group of the mhmp ligand sterically skews the structure resulting in a change in the coordination number of the Ln^{III} ion, and a comcomitant change in bond lengths and bridging angles, whilst retaining the same bridging motifs.

The hmp^-/$mhmp^-$ ligands are of two types: four are μ-bridging (**Fig. 5** (**a**)), chelating to the M^{II} ions, and bridging to the outer Ln^{III} ion; the remaining two are μ_3-bridging ((**Fig. 5** (**b**)), chelating to the Ln^{III} ions and further μ-bridging the two central M^{II} ions.

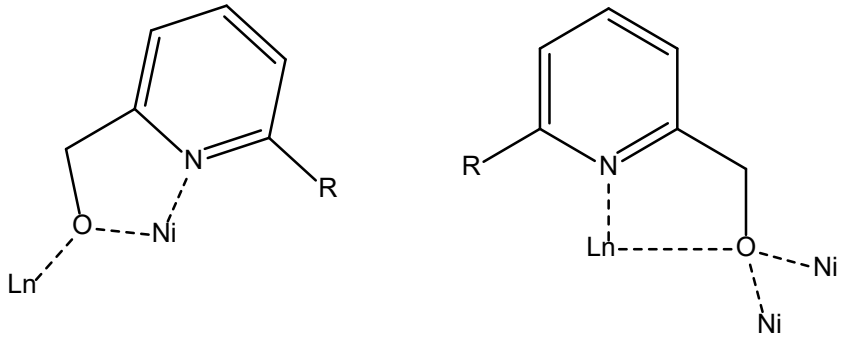

Figure 5 (**a**) μ-bridging (m)hmp^- ligand. (b) μ_3-bridging (m)hmp^-. Where R = H or CH_3 for hmp^- and $mhmp^-$, respectively.

For *BF1* the coordination of each of the Ln^{III} ions is completed by the presence of two chelating NO_3^- ions and one MeCN molecule. . For *BF2* there are also two chelating NO_3^- ions on each Ln^{III} ion, but no MeCN – on account of the Me-substituent on the ligand. Intramolecular pi-pi stacking interactions are present between the rings of the hmp^-/$mhmp^-$ ligands as seen in **fig. 4** (**a**) and (**c**), respectively. The effect on the distortion of bridging angles on changing ligand from hmp- to mhmp-, *i.e.* the addition of a single methyl group, is summarised in **fig**. **6** and **Tables 1**-**2**.

Table 1 Comparison of the bridging angles common to compounds **1**-**7** (*BF1*).

	1	**2**	**3**	**4**	**5**	**6**	**7**
Ln1-O2-M1	106.3(2)	108.15(9)	108.1(1)	108.2(1)	108.8(1)	108.8(1)	108.7(1)
Ln1-O3-M1'	108.0(2)	106.67(9)	106.6(1)	106.7(1)	107.1(1)	107.1(1)	106.9(1)
Ln1-O1-M1	99.6(2)	99.03(7)	98.9(1)	99.1(1)	100.2(1)	100.0(1)	100.1(1)
Ln1-O1-M1'	98.8(2)	99.64(7)	99.5(1)	99.8(1)	102.0(1)	101.8(1)	101.9(1)
M1-O1-M1'	100.1(2)	99.96(8)	100.2(1)	100.0(1)	99.3(1)	99.0(1)	99.1(1)

Table 2 Comparison of the bridging angles common to compounds **8**-**11** (*BF2*).

	8	**9**	**10**	**11**
Ln1-O2-M1	107.27(9)	106.8(2)	107.07(8)	108.0(1)
Ln1-O3-M1'	107.2(1)	107.3(2)	106.94(8)	108.1(1)
Ln1-O1-M1	97.12(8)	97.2(1)	98.94(7)	97.8(1)
Ln1-O1-M1'	98.91(8)	98.9(1)	97.20(6)	100.4(1)
M1-O1-M1'	101.89(8)	102.4(1)	102.06(7)	101.8(1)

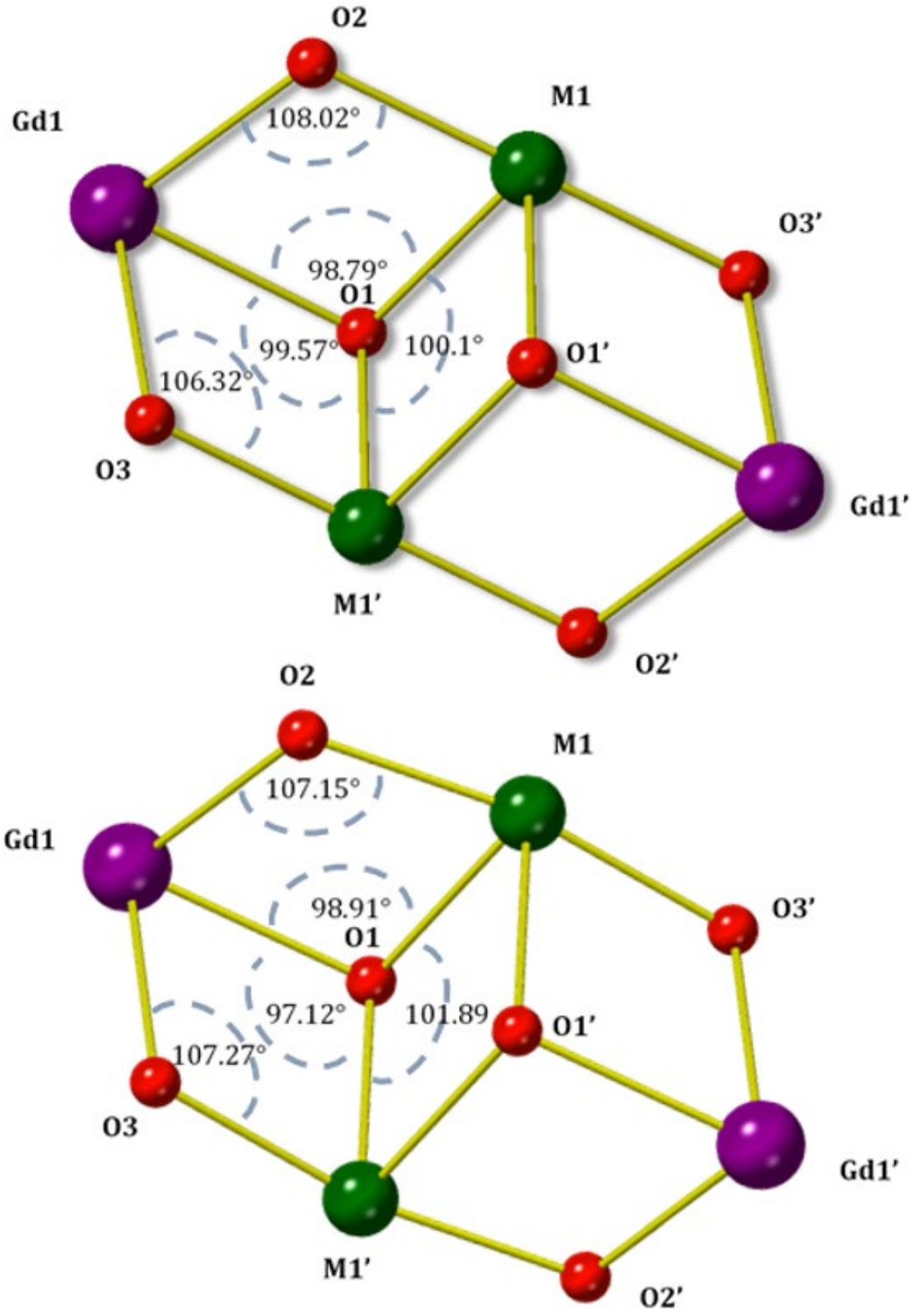

Figure 6 Comparison of the core structure with associated bond angles of **1** and **8**.

The Ln^{III} ions of *BF1* are 9 coordinate with capped square antiprismatic geometry (CShM = 2.466) and in *BF2* they are 8 coordinate and all possess triangular dodecahedron geometry (2.542) (**fig**. **7** (**b**) and **fig**. **8** (**b**)). [30] The M^{II} ions of **1**-**7** are all in an octahedral geometry with average Ni-$L_{N,O}$ and Zn-$L_{N,O}$ bond distances of 2.069 Å and 2.117 Å in *BF1*. The average Ln–(μ-O), Ln–(μ_3-O), Ln–O(NO_3) and Ln–N bond lengths are 2.238 Å, 2.361 Å, 2.531 Å and 2.558 Å, respectively. The M^{II} ions of **8**-**11** are all in an octahedral geometry with average Ni-$L_{N,O}$ and Zn-$L_{N,O}$ bond distances of 2.1063 Å and 2.1478 Å in *BF2*. The average Ln–(μ-O), Ln–(μ_3-O), Ln–O(NO_3) and Ln–N bond lengths are 2.211 Å, 2.294 Å, 2.477 Å and 2.592 Å, respectively. **Tables 3** and **4** summarise the bond distances for compounds **1**-**7** and **8**-**11**, respectively (labels shown in **fig**. **7** (**a**) and **fig**. **8** (**b**)).

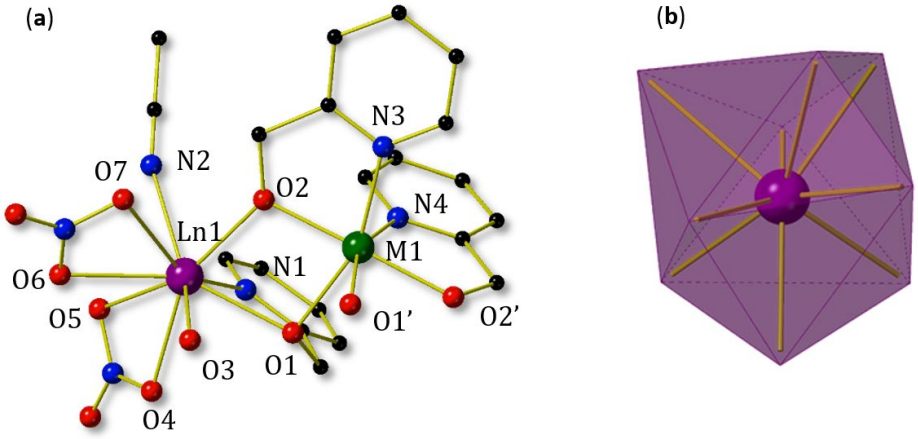

Figure 7 (**a**) Molecular structure of the ASU common to *BF1* displaying coordinating atom names (complex **7** shown). (**b**) Geometry of Ln^{III} ions of *BF1* (complex **7** shown).

Table 3 *BF1* transition metal and lanthanide coordination bond distances.

	1	2	3	4	5	6	7
Ln1-O1	2.408(5)	2.385(2)	2.386(3)	2.360(3)	2.380(3)	2.364(3)	2.357(3)
Ln1-O2	2.258(5)	2.245(2)	2.228(3)	2.225(3)	2.282(3)	2.259(3)	2.249(3)
Ln1-O3	2.267(5)	2.242(2)	2.238(3)	2.221(3)	2.271(3)	2.255(3)	2.248(3)
Ln1-O4	2.500(6)	2.575(2)	2.572(3)	2.561(3)	2.572(3)	2.569(3)	2.558(3)
Ln1-O5	2.626(6)	2.510(2)	2.506(3)	2.484(3)	2.533(3)	2.517(3)	2.505(3)
Ln1-O6	2.520(5)	2.467(2)	2.453(3)	2.432(3)	2.498(3)	2.480(3)	2.456(3)
Ln1-O7	2.582(7)	2.616(2)	2.616(3)	2.613(3)	2.619(3)	2.613(3)	2.613(3)
Ln1-N1	2.605(7)	2.594(2)	2.584(3)	2.578(3)	2.611(3)	2.601(3)	2.592(3)
Ln1-N2	2.568(7)	2.552(3)	2.541(4)	2.526(4)	2.554(4)	2.545(4)	2.538(4)
M1-O1'	2.141(5)	2.140(2)	2.129(3)	2.138(3)	2.210(3)	2.204(3)	2.197(3)
M1-O1	2.088(4)	2.090(2)	3.035(4)	2.088(3)	2.109(3)	2.110(3)	2.106(3)
M1-O2	2.013(5)	2.006(2)	2.011(3)	2.001(3)	2.047(3)	2.044(3)	2.045(3)
M1-O2'	2.028(5)	2.024(2)	2.026(3)	2.024(3)	2.067(3)	2.064(3)	2.069(3)
M1-N3	2.066(6)	2.065(2)	2.095(3)	2.086(4)	2.151(3)	2.129(4)	2.160(4)
M1-N4	2.095(6)	2.092(2)	2.062(3)	2.069(4)	2.126(3)	2.153(4)	2.122(4)

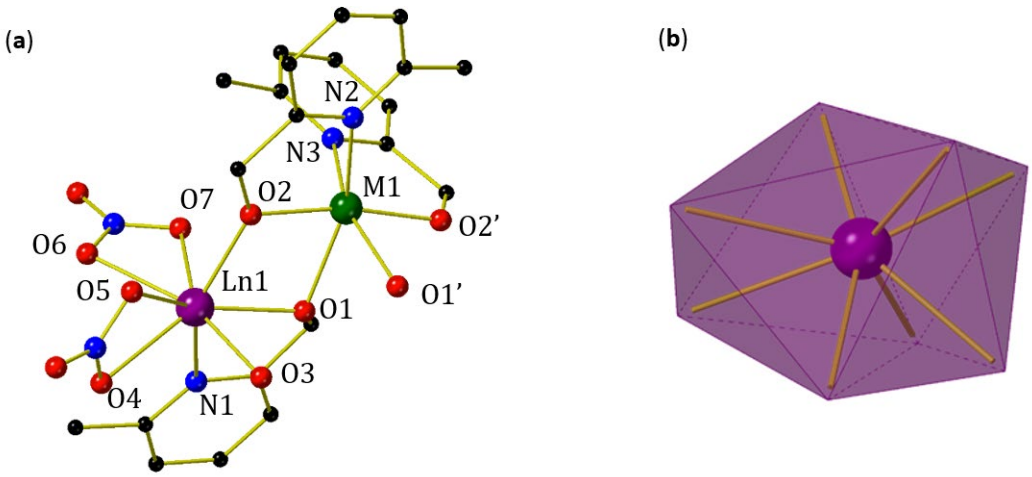

Figure 8 (**a**) Molecular structure of the ASU common to *BF2* displaying coordinating atom labels (complex **11** shown). (**b**) Geometry of Ln^{III} ions of *BF2* (complex **11** shown).

Table 4 *BF2* transition metal and lanthanide coordination bond distances.

	8	**9**	**10**	**11**
Ln1-O1	2.331(2)	2.300(4)	2.289(2)	2.273(3)
Ln1-O2	2.207(2)	2.204(4)	2.197(2)	2.199(3)
Ln1-O3	2.236(2)	2.195(4)	2.173(2)	2.220(3)
Ln1-O4	2.491(3)	2.499(5)	2.494(2)	2.469(4)
Ln1-O5	2.487(2)	2.438(4)	2.429(2)	2.468(3)
Ln1-O6	2.479(2)	2.462(4)	2.445(2)	2.435(3)
Ln1-O7	2.531(3)	2.478(5)	2.450(2)	2.521(4)
Ln1-N1	2.598(2)	2.583(5)	2.570(2)	2.596(3)
M1-O1'	2.194(2)	2.161(4)	2.188(2)	2.267(3)
M1-O1	2.152(2)	2.195(3)	2.149(2)	2.198(3)
M1-O2	1.997(2)	2.002(4)	1.997(2)	2.021(3)
M1-O2'	2.005(2)	2.002(4)	2.005(2)	2.027(4)
M1-N3	2.144(3)	2.140(4)	2.141(2)	2.189(4)
M1-N4	2.139(2)	2.145(5)	2.142(2)	2.191(3)

3.3.2 BF1 magnetism

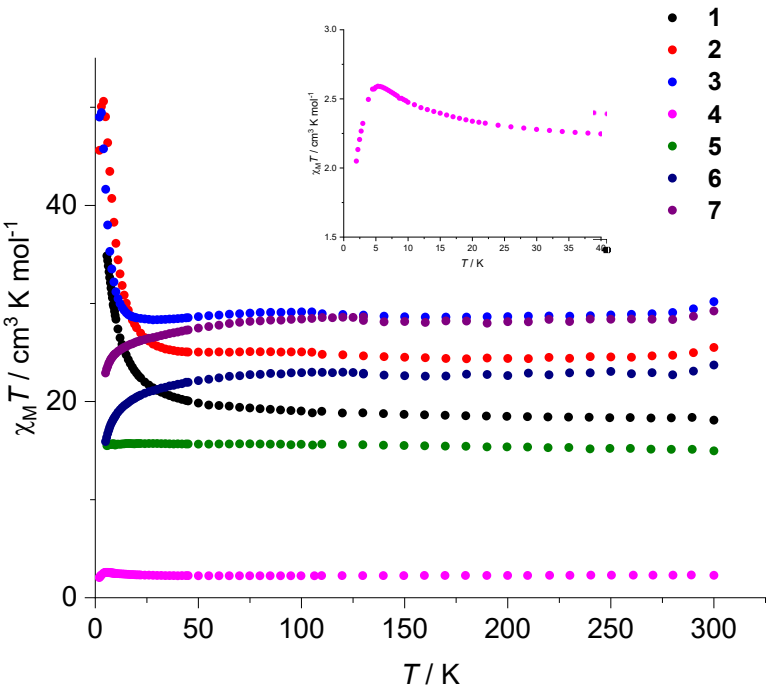

Figure 9 Plots of $\chi_M T$ versus T for **1**-**7** measured under 0.1 T applied dc magnetic field. Inset: Zoomed in $\chi_M T$ versus T plot for **4**.

Experimental $\chi_M T$ versus T plots for **1**-**7** are shown in **fig**. **9**. The room temperature experimental $\chi_M T$ values are (expected) 18.38 (18.06), 24.98 (23.64), 29.45 (30.64), 2.31 (2.30), 15.76 (15.50), 23.10 (23.64), 28.70 (28.34) cm^3 K mol^{-1} for **1**-**7**, respectively. These values are in good agreement with that expected for two Ni^{II} (S = 1, g = 2.15) and two Gd^{III} ($^8S_{7/2}$, g = 2), Tb^{III} ($^7F_6$, g = 3/2) and Dy^{III} ($^6H_{15/2}$, g = 4/3) ions that are non-interacting. Compounds **1**-**3** show similar profiles: between 300-100 K the $\chi_M T$ values stay relatively constant, **2** and **3** decreasing slightly due to zero-field splitting/depopulation effects. At the lowest temperatures measured, all three rise sharply, indicative of dominant ferromagnetic exchange interactions. The $\chi_M T$ value of **1** reaches a maximum of 34.86 cm^3 k mol^{-1} at 5 K, **2** reaches 50.60 cm^3 mol^{-1} at 4 K and **3** reaches 49.47 cm^3 mol^{-1} at 3 K. Both **2** and **3** then decrease slightly towards 2 K, resulting from zfs and/or inter- or intramolecular AF interactions. The $\chi_M T$ value of **4** decreases to 2.24 cm^3 K mol^{-1} to T = 100 K, before plateauing and then increasing to 2.59 cm^3 K mol^{-1} at 5.3 K. It then then sharply decreases to 2.05 cm^3 K mol^{-1}, due to zfs and/or intra-/intermolecular AF exchange. The $\chi_M T$ value of compound **5** remains essentially constant from 300-5 K, with a very small decrease below 8 K. The $\chi_M T$ values of compounds **6** and **7** remain constant from 300-100 K, before decreasing steadily to

2 K. This is due to one, or a combination of, depopulation effects, zfs, inter- or intramolecular AF exchange.

3.3.3 *BF1* fitting

The spin-Hamiltonian used to fit all systems described in this chapter is shown in **equation 1**, where μ_B is the Bohr-magneton, *g* is the *g*-factor, *B* is the magnetic field vector and $\hat{S}$ is a spin operator, *J* is the exchange interaction, and *D* is the zero-field splitting parameter.

$$\hat{H} = -2\sum_{i,j>i}^{n} \hat{S}_i J_{ij} \hat{S}_j + \mu_B \sum_{i=1}^{n} \vec{B}\, g_i \hat{S}_i + \sum_{i=1}^{n} D\left[\hat{S}_{z,i}^2 - S_i(S_i+1)/3\right] \quad (\mathbf{1})$$

The $\chi_M T$ of the $[Ni_2Gd_2]$ and $[Ni_2Y_2]$ analogues, **1** and **4**, were fitted using the program PHI,[31] employing the exchange interaction scheme shown in **fig**. **10**. We first fitted the data for **4** to extract J_{NiNi}, g_{Ni} and D_{Ni}. These values were then fixed, and used to fit the data of **1**, to extract J_{GdNi}.

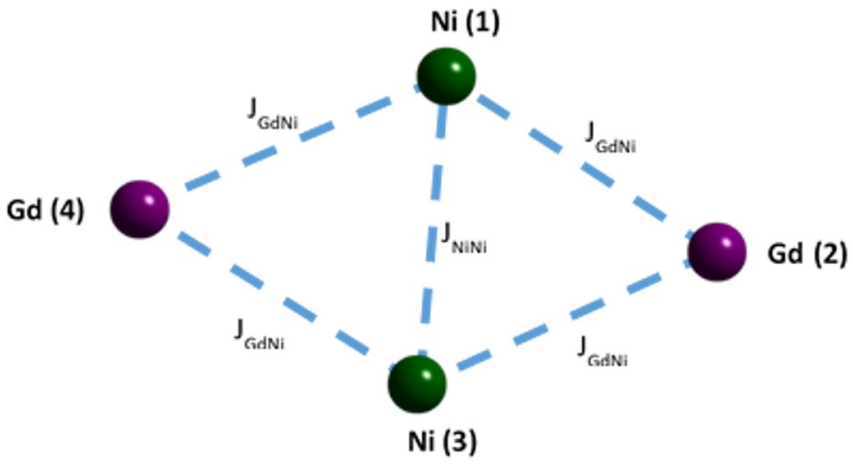

Figure 10 Exchange interaction scheme used to fit the magnetic susceptibility data for **1**.

The best fit exchange values determined for **4** are: J_{NiNi} = 2.98 cm^{-1}, g_{Ni} = 2.16 and D_{Ni} = 4.60 cm^{-1}. The subsequent best fit J_{GdNi} exchange value for **1** is J_{GdNi} = 0.73 cm^{-1} with g_{Gd} fixed at g_{Gd} = 2.00 (**figs**. **11** and **12**). The exchange Hamiltonians are shown in **equations 2** and **3**, respectively. These values are entirely consistent with literature precedent.[16, 32]

$$\hat{H} = -2J_{NiNi}(\hat{S}_1\hat{S}_3) \quad (\mathbf{2})$$

$$\hat{H} = -2J_{NiNi}(\hat{S}_1\hat{S}_3) - 2J_{GdNi}(\hat{S}_1\hat{S}_2 + \hat{S}_2\hat{S}_3 + \hat{S}_3\hat{S}_4 + \hat{S}_1\hat{S}_4) \quad (\mathbf{3})$$

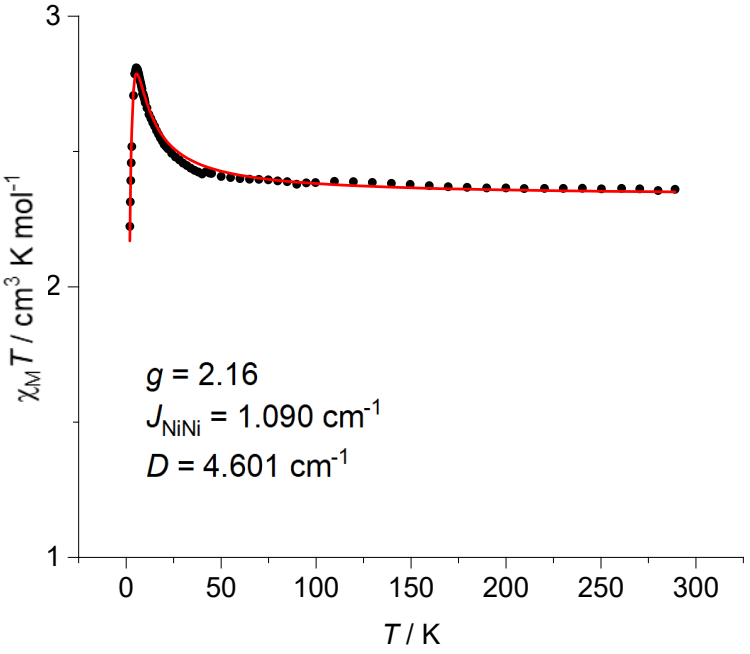

Figure 11 Plot of experimental (black circles) and best fit (red line) $\chi_M T$ versus T data for compound **4**.

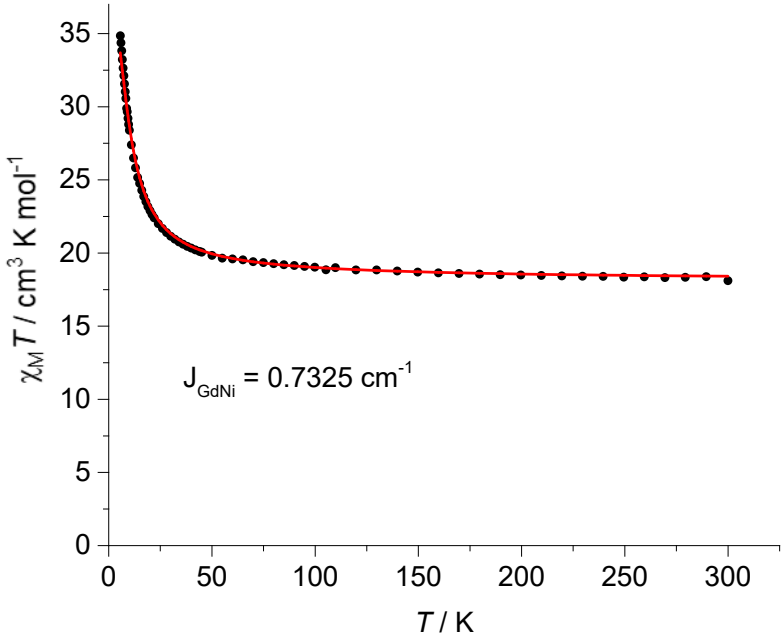

Figure 12 Plot of experimental (black circles) and best fit (red line) $\chi_M T$ versus T data for compound **1**.

3.3.4 *BF1* Dynamic Behaviour

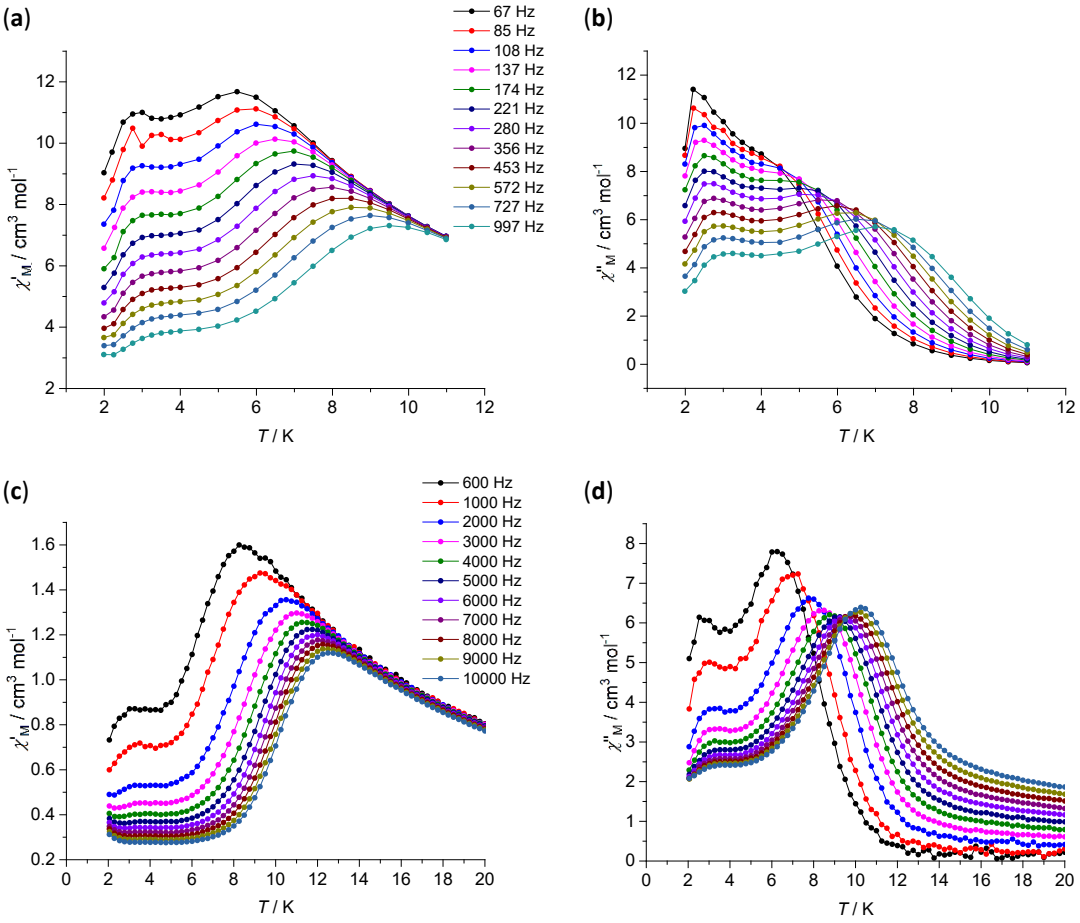

Figure 13 Dynamic Behaviour of **7**: (**a**) χ_M' SQUID measurements from 2-11 K. (**b**) χ_M'' SQUID measurements from 2-11 K . (**c**) χ_M' PPMS measurements from 2-20 K . (**d**) χ_M'' PPMS measurements from 2-20 K. Lines are a visual guide.

AC susceptibility measurements performed on **7** with an applied dc field of 0.1 T show temperature and frequency dependent behaviour (**fig**. **13**), indicating the presence of a thermal barrier for magnetization reversal. No such behaviour is present under zero dc field indicating that the QTM rate is competitive. Additionally, complexes **1**-**6** did not show any dynamic behaviour. **Fig**. **13** (**b**) gives the out-of-phase ac susceptibility as a function of temperature from 67-997 Hz which shows frequency dependent peaks up to approximately 7 K at 997 Hz, and frequency independent peaks below 4 K. The latter could be a result of long range order, *e.g.* spin-glass behaviour, or from single-ion QTM processes. **Fig**. **13** (**d**) shows the out-of-phase ac susceptibility data as a function of temperature from 600-10000 Hz which displays a continuation of the frequency dependent peaks of **fig**. **13** (**b**) up to approximately 11 K at 10000 Hz.

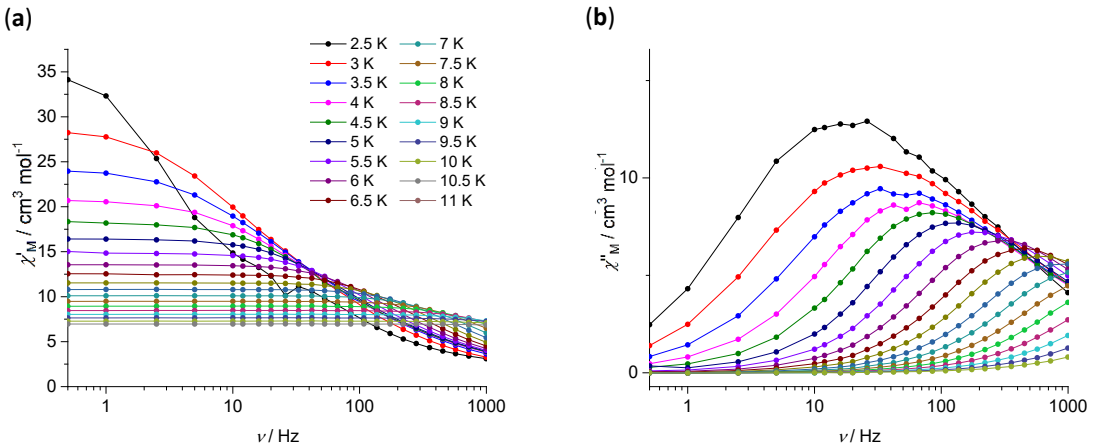

Figure 14 Dynamic Behaviour of **7**: (**a**) χ_M' measured from 2.5-11 K in the SQUID. (**b**) χ_M'' measured from 2.5-11 K in the SQUID. Lines are a visual guide.

Representing the out-of-phase AC susceptibility as a function of frequency (**fig**. **14** (**b**)) removes the frequency independent peaks, and thus is more appropriate to extract values for Arrhenius plots below 5 K. At 2.5 K a peak in the χ_M'' forms at ~18.2 Hz. Upon increasing the temperature, the maximum of the peaks shift to higher frequencies until 7 K. After which temperature, the maximum cannot be observed as they are above 1000 Hz. The fitted Cole-Cole plots (**fig**. **15**) indicate that the frequency dependent peaks are from a single relaxation pathway.[33]

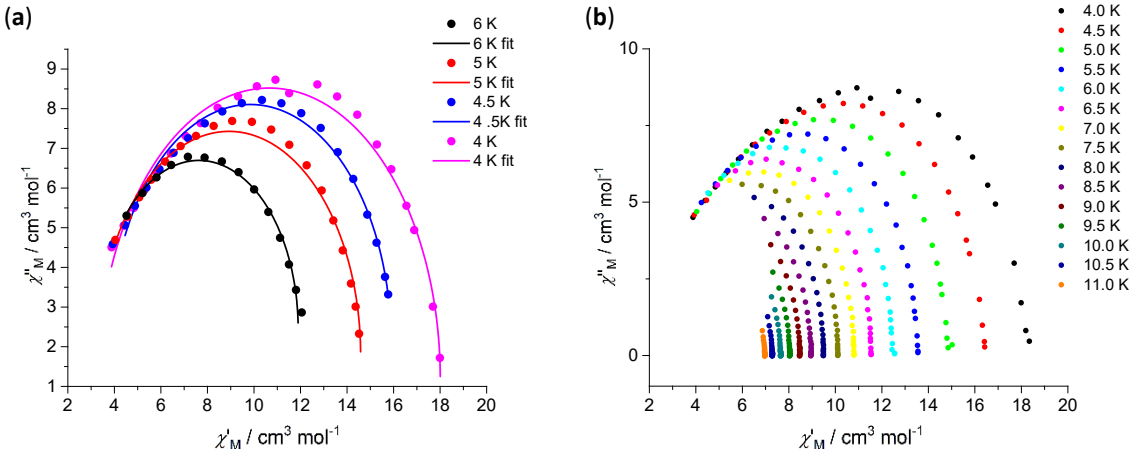

Figure 15 Cole-Cole plots for: (**a**) **7** with fitting; 0.1 T applied field from 4-6 K. (**b**) **7**; 0.1 T applied field from 4-10 K.

Upon decreasing the temperature from 6 to 4 K there is a broadening of the peaks as a result of additional relaxation pathways. Above this temperature only the thermal barrier relaxation process operates. The full temperature range Cole-Cole plot is shown in **fig**. **15** (**b**).

Table 5 summarises the data fitting from the Cole-Cole plots given in **fig**. **15** (**a**). Cole-Cole plots are calculated using **equation 3** which is a relaxation model.

$$\chi''(\chi) = \frac{\chi_T - \chi_S}{2\tan[\frac{(1+\alpha)\pi}{2}]} + \sqrt{\left(\chi' - \chi_S\right)\left(\chi_T - \chi'\right) + \frac{(\chi_T - \chi_S)^2}{4tan^2[\frac{(1+\alpha)\pi}{2}]}} \qquad (4)$$

The exponent parameter α which takes values between 0 and 1, describes different spectral shapes. When α = 0, this model reduces to a Debye model and when α > 0 the relaxation is stretched. So when α is close to 0 it indicates that there is one relaxation pathway. The values of χ_S and χ_T are the values of where the model crosses the χ_M' axis.

Table 5 Alpha values derived from the Cole-Cole fits of **7** in an applied field of 0.1 T.

	***T* / K**			
	4.0	4.5	5.0	6.0
χS	3.30922	3.82911	3.53447	3.44385
error	0.13356	0.09258	0.41115	1.24176
χT	18.00266	15.86614	14.39329	11.81741
error	0.04874	0.04832	0.18907	0.46939
α	0.10034	0.209797	0.23513	0.33438
error	0.013	0.01136	0.05333	0.15777

3.3.5 BF2 Magnetism

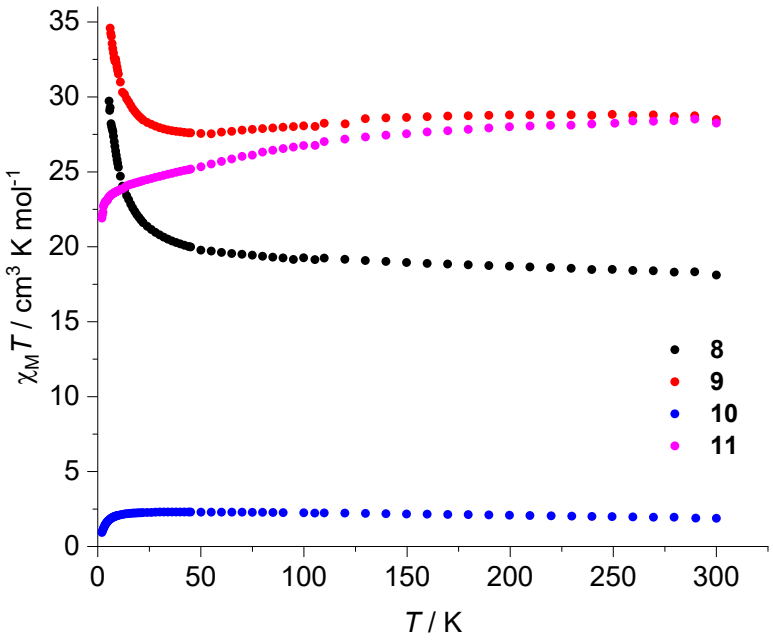

Figure 16 Plot of $\chi_M T$ versus T data for compounds **8**-**11** measured under an applied field of 0.1 T.

Experimental $\chi_M T$ versus T data for **8**-**11** are shown in **fig**. **16**. Room temperature experimental $\chi_M T$ values (expected) 18.11 (18.06), 28.48 (28.34), 2.25 (2.30), 28.41 (28.34) cm^3 K mol^{-1} for **8**-**11,** respectively, are in good agreement with those expected for two Ni^{II} (S = 1, g = 2.15) and two Gd^{III} ($^8S_{7/2}$, g = 2), Tb^{III} ($^7F_6$, g = 3/2), Dy^{III} ($^6H_{15/2}$, g = 4/3), Ho^{III} ($^5I_8$, g = 5/4) and Er^{III} ($^4I_{15/2}$, g = 6/5) ions that are non-interacting. For compounds **8** and **9**, the $\chi_M T$ values remain relatively constant until 100 K where **8** begins to steadily rise and **9** slightly decreases, before they both increase more rapidly to 29.72 and 34.59 cm^3 K mol^{-1}, respectively, suggestive of the presence of ferromagnetic exchange interactions. The data for complex **10** remains essentially constant in the whole temperature range, with a small decrease in $\chi_M T$ at very low temperature. For compound **11** the $\chi_M T$ value decreases with decreasing temperature to ~30 K, consistent with the depopulation of the M_J states of the Dy^{III} ion, before decreasing more rapidly at lower temperatures. The data for both is indicative of weak AF exchange between the constituent metal centres.

3.3.6 *BF2* Fitting

The $\chi_M T$ versus T data of the [Ni_2Gd_2] and [Ni_2Y_2] analogues, **8** and **10**, were fitted using the program PHI using the same model as described above for *BF1*.[31] As with the *BF1* family of

complexes above, the data of the $[Ni_2Y_2]$ analogue **10** was fitted first, before fixing g_{Ni}, J_{NiNi} and D_{Ni} and fitting the data obtained for the $[Ni_2Gd_2]$ analogue **8**. The best fit exchange values determined employing **equation 1** for **10** (**fig**. **17**) are: J_{NiNi} = -0.32 cm^{-1}, g_{Ni} = 2.2 and D_{Ni} = 3.03 cm^{-1}. Using these values the best fit exchange J_{GdNi} value for **8** (**fig**. **18**) was J_{GdNi} = 0.52 cm^{-1} with g_{Gd} fixed at g_{Gd} = 2.00. The exchange Hamiltonians used are given in **equations 5** and **6**, respectively.

$$\widehat{H} = -2J_{NiNi}(\hat{S}_1\hat{S}_3) \quad (5)$$

$$\widehat{H} = -2J_{NiNi}(\hat{S}_1\hat{S}_3) - 2J_{GdNi}(\hat{S}_1\hat{S}_2 + \hat{S}_2\hat{S}_3 + \hat{S}_3\hat{S}_4 + \hat{S}_1\hat{S}_4) \quad (6)$$

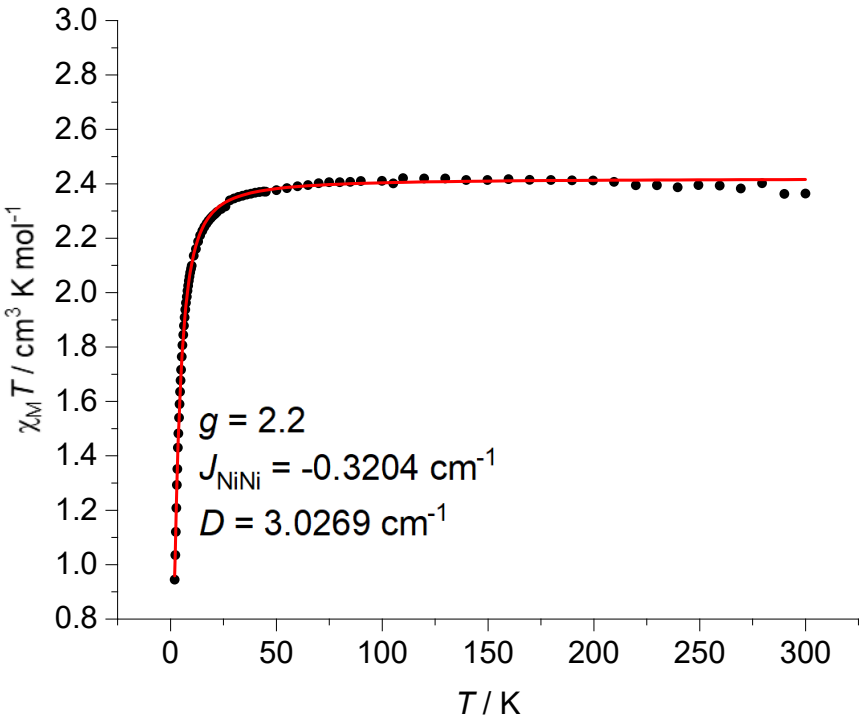

Figure 17 Plot of experimental (black circles) and best fit (red line) $\chi_M T$ versus T data for compound **10**.

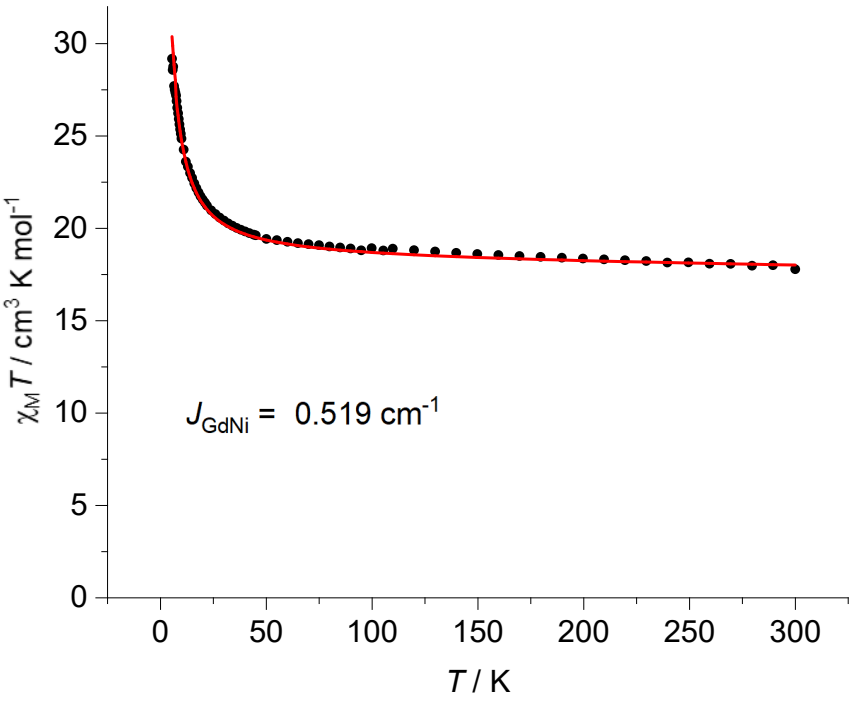

Figure 18 Plot of experimental (black circles) and best fit (red line) $\chi_M T$ versus T data for compound **8**.

3.3.7 *BF2* Dynamic Behaviour

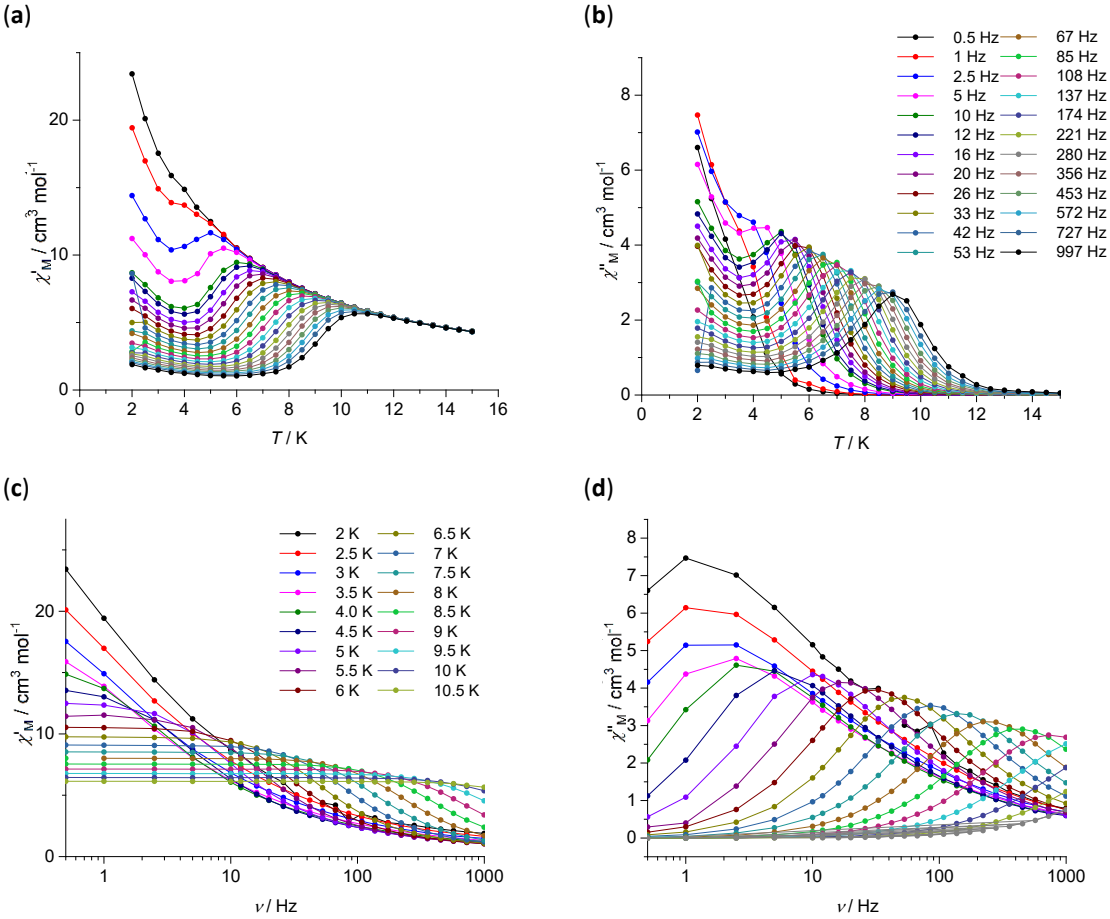

Figure 19 Dynamic Behaviour of **11**: (**a**) χ_M' SQUID measurements from 2-15 K as a function of temperature. (**b**) χ_M'' SQUID measurements from 2-15 K as a function of temperature. (**c**) χ_M' SQUID measurements from 2-10.5 K as a function of frequency. (**d**) χ_M'' SQUID measurements from 2-10.5 as a function of frequency.

Ac susceptibility measurements performed on **11** in an applied dc field of 0.1 T show temperature and frequency dependent behaviour (**fig**. **19**), indicating the presence of a thermal barrier for magnetization reversal. No such behaviour was present under zero dc field indicating that the QTM rate is competitive. **Fig**. **19** (**b**) shows the out-of-phase ac susceptibility data as a function of temperature from 0.5-997 Hz displaying frequency dependent peaks to approximately 9 K at 997 Hz. Frequency independent signals are observed below 3 K. The out-of-phase AC susceptibility as a function of frequency is given in **fig**. **19** (**d**). At 2 K a maximum in χ_M'' is observed at around 1.181 Hz. Upon increasing the temperature, the maximum shifts to higher frequencies until fully observable peaks are seen at 4.5 K. This remains up to 9 K, above which the maximum χ_M'' values appear above 1000

Hz. Cole-Cole plots (**fig**. **20**, **Table 6**) indicate that the frequency dependent peaks are from a single relaxation pathway.

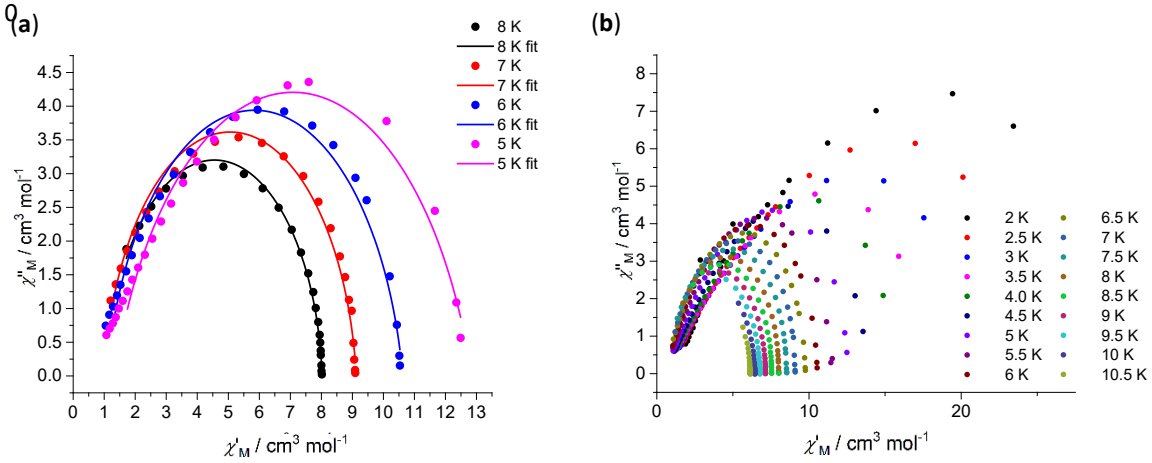

Figure 20 Cole-Cole Plots for: (**a**) **11** with fitting, 0.1 T applied field from 5-8 K at 0.5-997 Hz. (**b**) **11**, 0.1 T applied field from 2-12 K at 0.5-997 Hz.

Upon decreasing the temperature from 8 to 5 K there is a broadening of the out-of-phase peaks as a result of the emergence of additional relaxation pathways, as observed for *BF1*. The full temperature range Cole-Cole plot is shown in **fig**. **20** (**b**). The corresponding α values for 8 and 5 K are 0.0518 (± 0.00799) and 0.18836 (± 0.01493), respectively. Deviation from an α value from 0 towards 1 indicates that additional relaxation pathways are present.[1, 34, 35] **Table 6** summarises the fitting data of the Cole-Cole plots in **fig**. **20** (**a**).

Table 6 Alpha (α) values of Cole-Cole fits of **8** powder 0.1 T applied field

	Temperature / K			
	5.0	6.0	7.0	8.0
χS	1.06988	0.99112	0.97391	1.06706
error	0.13075	0.06469	0.05269	0.05691
χT	13.10246	10.70553	9.1473	8.03511
error	0.12873	0.04954	0.02483	0.01077
α	0.18836	0.11998	0.07338	0.05184
error	0.01493	0.01173	0.01089	0.00799

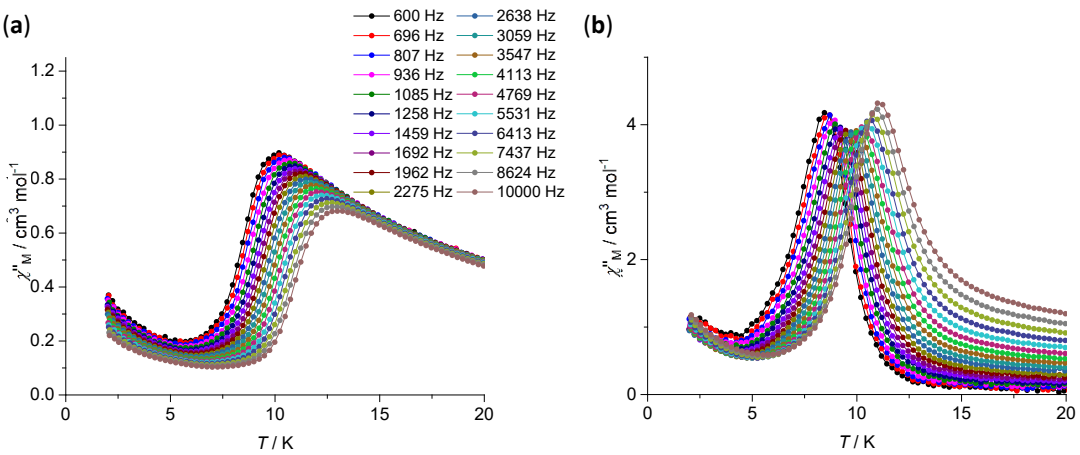

Figure 21 Dynamic Behaviour of **11**: (**a**) χ_M' PPMS measurements from 2-20 K. (**b**) χ_M'' PPMS measurements from 2-20 K.

Out-of-phase ac susceptibility measurements for **11** in the frequency range 600-10000 Hz show frequency dependent behaviour with maxima in χ_M'' being present to approximately 11.15 K at 10000 Hz (**fig**. **21**). There also appears to be frequency independent behaviour below 5 K. The maxima originate from a single relaxation pathway, as confirmed by the Cole-Cole plot shown in **fig**. **22**.

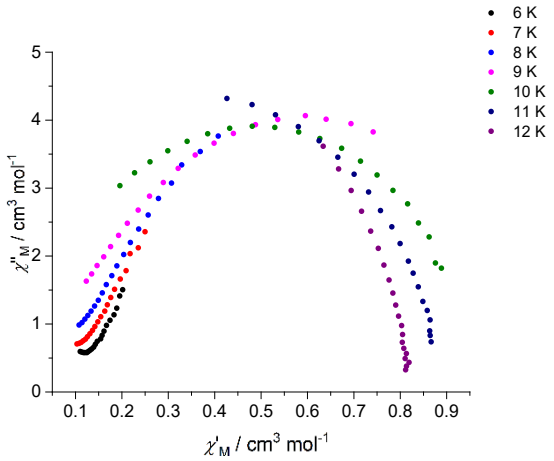

Figure 22 Cole-Cole plots for **11**, 0.1 T applied field, from 6-12 K, 600-10000 Hz.

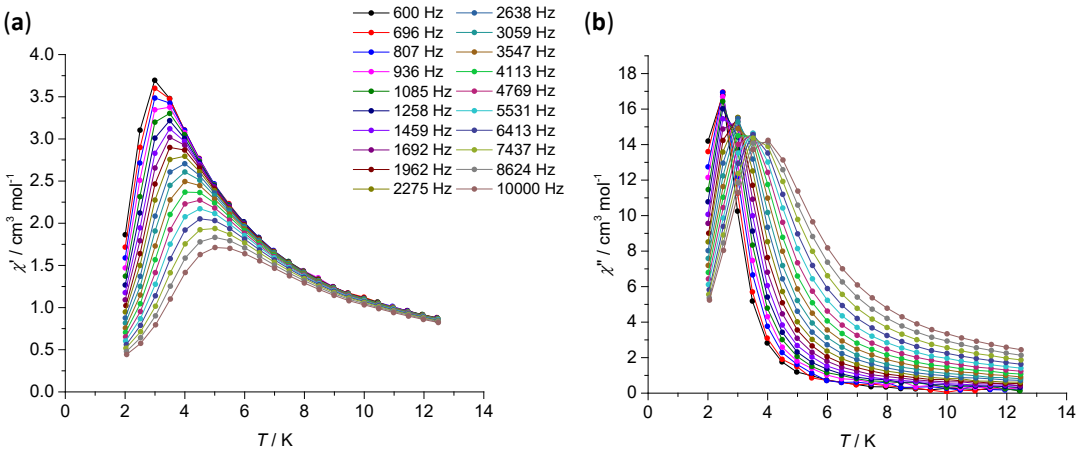

Figure 23 Dynamic Behaviour of **9**: (**a**) χ_M'' PPMS measurements from 2-12.5 K. (**b**) χ_M' from 2-12.5 K from 600-10000 Hz.

Out-of-phase ac susceptibility measurements for **9** in the 600-10000 Hz frequency range display frequency dependent behaviour with maxima up to ~4 K at 10000 Hz, and down to 2.4 K at 600 Hz (**fig**. **23**). Compared to the χ_M'' data of the $[Zn_2Dy_2]$ complex, **11**, the maxima for **9** have shifted considerably downward in temperature, showing that the SMM behaviour is poorer as the result of the addition of J_{DyNi} interactions. The maxima appear to be of a single relaxation pathway, as confirmed by the Cole-Cole plot shown in **fig**. **24**.

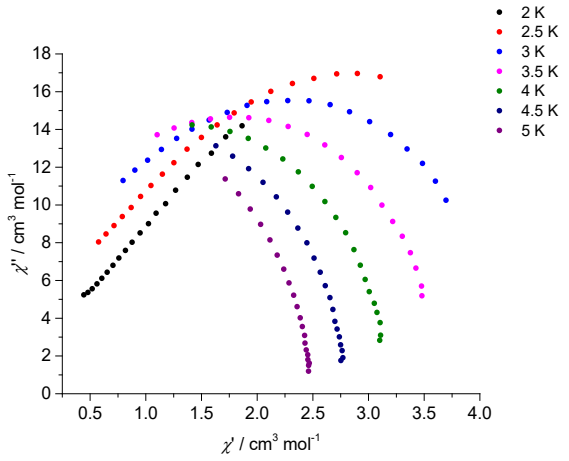

Figure 24 Cole-Cole plots of **9**, 0.1 T applied field, from 2-5 K, 600-10000 Hz.

The Arrhenius plots for **7**, **9** and **11** are shown in **fig**. **25** which gives a direct comparison of the relaxation behaviour with associated U_{eff} values.

3.3.8 Arrhenius plots

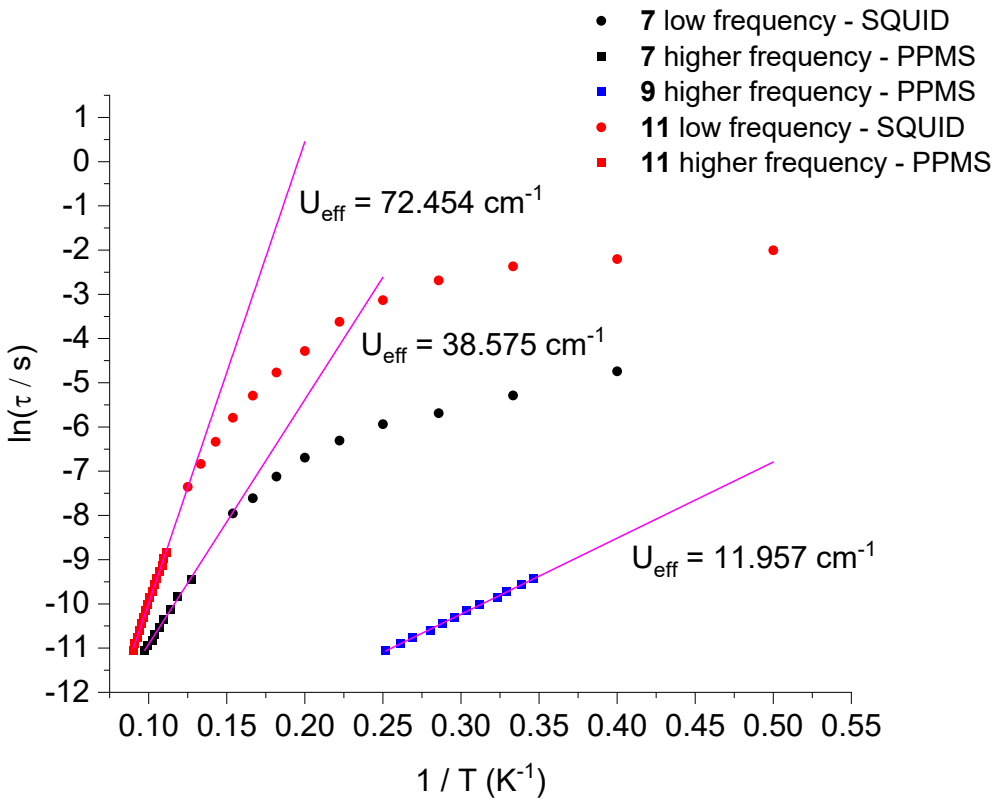

Figure 25 Arrhenius plots for **7**, **9** and **11** constructed from the low frequency (filled circles) and high frequency (filled squares) out-of-phase ac susceptibility data. The solid lines (magenta) represent the linear fits of the data using the Arrhenius law.

The Arrhenius plots were constructed using the χ_M'' data for **7**, **9** and **11**, with both 0.5-1000 and 1000-10000 Hz regions, employing the Arrhenius law, $\tau = \tau_0 \exp(U_{eff}/k_B T)$. The data is summarised in **Table 6**.

Table 6 U_{eff} and τ_0 values, for compounds **7**, **9** and **11** extracted from an Arrhenius analysis of the out-of-phase ac susceptibility data.

	7	**9**	**11**
U_{eff} **(cm^{-1})**	38.575	11.957	72.4536
Error (cm^{-1})	0.920	0.146	1.1779
τ_0 **(s)**	7.239 x 10-8	2.060 x 10-7	1.379 x 10-9
Error (s)	9.738 X 10-9	1.265 x 10-8	2.1644 x 10-10

Upon decreasing frequency there is a plateau in the frequency dependent behaviour indicating that additional relaxation pathways, such as QTM, are present. The $[Zn_2Dy_2]$ complex of *BF2*, **11**, has a larger U_{eff} value than that of *BF1*, **7**, indicating that the structural differences between the two complexes causes a change in the dynamic behaviour. The change in lanthanide geometry from capped square antiprismatic in *BF1* to triangular dodecahedron in *BF2* could have had an impact on the dynamic behaviour but without

computational analysis to determine the anisotropy axis direction it cannot be determined here. The change in Ln-O-M and M-O-M' bond angles may also have a role in the change in magnetic behaviour. The U_{eff} value of **11**, measured in applied dc field, is close to the record value for butterfly species, of 73 cm^{-1}[36] which was measured in zero applied dc field.[27] Although these values are comparable, the U_{eff} value of **11** was measured in applied field which prevents QTM so is therefore does not retain its magnetisation as effectively.

The $[Ni_2Dy_2]$ complex, **9**, has a much smaller U_{eff} value than the $[Zn_2Dy_2]$ complex, **11**, and the relaxation mechanism appears to be of different origin. This indicates that the addition of J_{DyNi} interactions has a negative effect on the relaxation behaviour of the system. Fitting of compounds **4** and **10** show that the J_{NiNi} value is 1.090 cm^{-1} and -0.3204 cm^{-1}, respectively. The change from ferromagnetic to antiferromagnetic exchange could be due to the change in M-O-M' bond angle between **4** and **10** from 100° to 102.06° with a change of 2.06°. A magneto-structural correlation of the Ni-O-Ni bond angles with the J_{NiNi} in $[Ni_4X_4]^{4+}$ cubane complexes showed a linear relationship.[36, 37] It was shown that a switch between ferromagnetic exchanges below 99° Ni-O-Ni bond angle to antiferromagnetic above. However, these values were also dependant on the Ni-O-O-Ni torsion angle of the bridging carboxylates not present in the structures investigated here. So although a magneto-structural correlation is possible the systems report here cannot be compared to literature correlations directly.

The values derived from the fitting of the $\chi_M T$ data of **1**, **4**, **8** and **10** show that the J_{GdNi} value is larger for *BF1* (J_{GdNi} = 0.73 cm^{-1}) than *BF2* (J_{GdNi} = 0.52 cm^{-1}) which could be due to the change in the Ln-O-M bond angles and ligand field but without computational work this it is not possible to correlate these. Structures containing this ligand (hmp) have shown positive *J* values (ferromagnetic interactions), this is no exception.[11, 16, 32] However, the data suggests that the J_{DyNi} interaction in **9** will be smaller than that in **3**. A comprehensive systematic study of butterfly compounds with 27 analogous structures with several different transition metals indicated that it is not the sign (AF, F) of the exchange interaction that quenches the single ion dynamic behaviour of Dy^{III}, rather it is its magnitude.[1] Larger *J* values result in increased QTM due to mixing of low lying energy levels close to the ground state.[1, 22, 33] The J_{NiNi} interaction in *BF2* is antiferromagnetic (J_{NiNi} = -0.32 cm^{-1}), whilst that in *BF1* is ferromagnetic (J_{NiNi} = 1.09 cm^{-1}). There is no simple magneto-structural relationship found in the literature to correlate bond angles in these 3*d*-4*f* structure types to the values calculated.[16]

3.4 Conclusion

Compounds **1**-**7** and **8**-**11**, of general formulae $[M^{II}_2Ln^{III}_2(hmp)_6(NO_3)_4]\cdot MeOH$ (*BF1*) and $[M^{II}_2Ln^{III}_2(mhmp)_6(NO_3)_4]\cdot MeCN$ (*BF2*), have been synthesised and magneto-structurally characterised. These complexes possess two-fold symmetry and what is known as a butterfly-like topology with the M^{II} ions in the body positions and Ln^{III} ions on the wings. The addition of a methyl group to the ligand ($mhmp^-$) in the *BF2* family of compounds compared to that of *BF1* (hmp^-) family of compounds results in a change to the bond angles involved in mediating magnetic exchange between the metal centres, and in the local geometries of the Ln^{III} ion ions. The latter were analysed with SHAPE software to be 9 coordinate capped square-antiprism for *BF1* and 8 coordinate triangular dodecahedron for *BF2*. Fitting of the magnetic susceptibility data collected for compounds, **1** and **4** (*BF1)* revealed best fit parameters: J_{NiNi} = 1.09 cm^{-1} and J_{GdNi} = 0.7325 cm^{-1}. Analogous measurements of **8** and **10** (*BF2)* revealed best fit parameters: J_{NiNi} = -0.32 cm^{-1} and J_{GdNi} = 0.52 cm^{-1}. The $[Zn_2Dy_2]$ analogues of both *BF1* and *BF2* (**7** and **11**) display frequency dependent peaks in out-of-phase ac susceptibility measurements indicating slow relaxation of magnetisation. The U_{eff} values for **7** and **11** were calculated to be 38.58 cm^{-1} and 72.45 cm^{-1}, respectively. The larger U_{eff} in *BF2* is a result of a change in single-ion magnet behaviour at the Ln^{III} ion due to the change in geometry. The $[Ni_2Dy_2]$ analogue of *BF2* (**9**) also exhibits frequency dependent behaviour in ac susceptibility measurements with a U_{eff} = 11.957 cm^{-1}, whereas the $[Ni_2Dy_2]$ analogue of *BF1* did not. This could be due to the improvement in SIM behaviour paired with a weaker J_{LnNi} value.

3.5 References

1. E. M. Pineda, N. F. Chilton, F. Tuna, R. E. P. Winpenny and E. J. L. McInnes, *Inorg. Chem.*, 2015, **54**, 5930-5941.
2. S. Wang, X. Yang, J. Qian, Q. Li, Z. Chen, L. Zhang, S. Huang, C. Wang and R. A. Jones, *Dalton Trans.*, 2017, **46**, 1748-1752.
3. M. X. Yao, Z. X. Zhu, X. Y. Lu, X. W. Deng and S. Jing, *Dalton Trans.*, 2016, **45**, 10689-10695.
4. W.-K. Dong, J.-C. Ma, L.-C. Zhu and Y. Zhang, *New J. Chem.* 2016, **40**, 6998-7010.
5. D. I. Alexandropoulos, L. Cunha-Silva, G. Lorusso, M. Evangelisti, J. Tang and T. C. Stamatatos, *Chem. Comm.*, 2016, **52**, 1693-1696.
6. J. Wu, L. Zhao, P. Zhang, L. Zhang, M. Guo and J. Tang, *Dalton Trans.*, 2015, **44**, 11935-11942.
7. X.-Y. Lu, Y.-Q. Liu, X.-W. Deng, Z.-X. Zhu, M.-X. Yao and S. Jing, *New Journal of Chem. Euro. J*, 2015, **39**, 3467-3473.
8. C. Chen, Y. Liu, P. Li, H. Zhou and X. Shen, *Dalton Trans.*, 2015, **44**, 20193-20199.
9. A. B. Canaj, D. I. Tzimopoulos, M. Siczek, T. Lis, R. Inglis and C. J. Milios, *Inorg. Chem.*, 2015, **54**, 7089-7095.
10. L. Zhao, J. Wu, H. Ke and J. Tang, *Inorg. Chem.*, 2014, **53**, 3519-3525.
11. P. Wang, S. Shannigrahi, N. L. Yakovlev and T. S. Hor, *Dalton Trans.*, 2014, **43**, 182-187.
12. T. D. Pasatoiu, A. Ghirri, A. M. Madalan, M. Affronte and M. Andruh, *Dalton Trans.*, 2014, **43**, 9136-9142.
13. A. Chakraborty, P. Bag, E. Riviere, T. Mallah and V. Chandrasekhar, *Dalton Trans.*, 2014, **43**, 8921-8932.
14. N. Ahmed, C. Das, S. Vaidya, A. K. Srivastava, S. K. Langley, K. S. Murray and M. Shanmugam, *Dalton Trans.*, 2014, **43**, 17375-17384.
15. N. Ahmed, C. Das, S. Vaidya, S. K. Langley, K. S. Murray and M. Shanmugam, *Chem. Euro. J.*, 2014, **20**, 14235-14239.
16. W. R. Yu, G. H. Lee and E. C. Yang, *Dalton Trans.*, 2013, **42**, 3941-3949.
17. Q. W. Xie, S. Q. Wu, C. M. Liu, A. L. Cui and H. Z. Kou, *Dalton Trans.*, 2013, **42**, 11227-11233.
18. X. Yi, K. Bernot, F. Pointillart, G. Poneti, G. Calvez, C. Daiguebonne, O. Guillou and R. Sessoli, *Chemi. Euro. J*, 2012, **18**, 11379-11387.
19. S. Sakamoto, S. Yamauchi, H. Hagiwara, N. Matsumoto, Y. Sunatsuki and N. Re, *Inorg. Chem. Comm.*, 2012, **26**, 20-23.
20. T. D. Pasatoiu, J. P. Sutter, A. M. Madalan, F. Z. Fellah, C. Duhayon and M. Andruh, *Inorg. Chem.*, 2011, **50**, 5890-5898.
21. K. C. Mondal, G. E. Kostakis, Y. Lan, W. Wernsdorfer, C. E. Anson and A. K. Powell, *Inorg. Chem.*, 2011, **50**, 11604-11611.
22. S. Hill, S. Datta, J. Liu, R. Inglis, C. J. Milios, P. L. Feng, J. J. Henderson, E. del Barco, E. K. Brechin and D. N. Hendrickson, *Dalton Trans.*, 2010, **39**, 4693-4707.
23. C. G. Efthymiou, T. C. Stamatatos, C. Papatriantafyllopoulou, A. J. Tasiopoulos, W. Wernsdorfer, S. P. Perlepes and G. Christou, *Inorg. Chem.*, 2010, **49**, 9737-9739.
24. J. P. Sutter, S. Dhers, R. Rajamani, S. Ramasesha, J. P. Costes, C. Duhayon and L. Vendier, *Inorg. Chem.*, 2009, **48**, 5820-5828.
25. J. P. Costes, T. Yamaguchi, M. Kojima and L. Vendier, *Inorg. Chem.*, 2009, **48**, 5555-5561.
26. V. Chandrasekhar, P. Bag, W. Kroener, K. Gieb and P. Muller, *Inorg. Chem.*, 2013, **52**, 13078-13086.

27. F. H. Zhao, H. Li, Y. X. Che, J. M. Zheng, V. Vieru, L. F. Chibotaru, F. Grandjean and G. J. Long, *Inorg Chem*, 2014, **53**, 9785-9799.
28. G. M. Sheldrick, *Acta Crys. A*, 2008, **64**, 112-122.
29. O. V. Dolomanov, L. J. Bourhis, R. J. Gildea, J. A. K. Howard and H. Puschmann, *J. App. Crys.*, 2009, **42**, 339-341.
30. M. Llunell, D. Casanova, J. Cirera, P. Alemany and S. Alvarez, *SHAPE, Version 2.0*, 2010.
31. N. F. Chilton, R. P. Anderson, L. D. Turner, A. Soncini and K. S. Murray, *J. Comp. Chem.*, 2013, **34**, 1164-1175.
32. T. N. Hooper, J. Schnack, S. Piligkos, M. Evangelisti and E. K. Brechin, *Angew. Chem. Int. Ed.*, 2012, **51**, 4633-4636.
33. R. J. Blagg, L. Ungur, F. Tuna, J. Speak, P. Comar, D. Collison, W. Wernsdorfer, E. J. McInnes, L. F. Chibotaru and R. E. Winpenny, *Nature Chem.*, 2013, **5**, 673-678.
34. E. Lucaccini, M. Briganti, M. Perfetti, L. Vendier, J. P. Costes, F. Totti, R. Sessoli and L. Sorace, *Chem. Euro. J*, 2016, **22**, 5552-5562.
35. L. T. A. Ho and L. F. Chibotaru, *Phys. Rev. B,* 2016, **94**, 104422-104427.
36. J. P. S. Walsh, S. Sproules, N. F. Chilton, A.-L. Barra, G. A. Timco, D. Collison, E. J. L. McInnes and R. E. P. Winpenny, *Inorg. Chem.*, 2014, **53**, 8464-8472.
37. M. A. Halcrow, J.-S. Sun, J. C. Huffman and G. Christou, *Inorg. Chem.*, 1995, **34**, 4167-4177.

3.6 Supplementary Information

Table S1 Crystallographic details for **1-4**

	1	**2**	**3**	**4**
Empirical formula	$C_{40}H_{42}Gd_2N_{12}Ni_2O_{18}$	$C_{41}H_{46}N_{12}Ni_2O_{19}Tb_2$	$C_{41}H_{42}Dy_2N_{14}Ni_2O_{18}$	$C_{40}H_{42}N_{12}Ni_2O_{18}Y_2$
Formula weight	1410.77	1446.16	1461.3	1274.09
Temperature/ K	120.01(10)	120	120.00(10)	120.00(10)
Crystal system	monoclinic	monoclinic	monoclinic	monoclinic
Space group	$P2_1/n$	$P2_1/n$	$P2_1/n$	$P2_1/n$
***a*/Å**	13.7134(5)	13.7166(4)	13.72999(12)	13.7319(8)
***b*/Å**	11.0870(5)	11.0485(3)	11.03378(12)	11.0219(6)
***c*/Å**	16.5991(7)	16.5797(4)	16.59027(17)	16.5768(11)
α/°	90	90	90	90
β/°	94.377(4)	94.343(3)	94.3212(9)	94.359(6)
γ/°	90	90	90	90
Volume/Å^3	2516.36(18)	2505.41(12)	2506.17(4)	2501.7(3)
Z	2	2	2	2
ρ_{calc}g/cm^3	1.862	1.917	1.936	1.691
μ/mm^{-1}	18.335	3.616	17.28	3.122
***F*(000)**	1388	1428	1436	1288
Crystal size/mm^3	0.052 × 0.0399 × 0.0302	0.4491 × 0.0683 × 0.0395	0.2558 × 0.0474 × 0.0328	0.4717 × 0.0446 × 0.0262
Radiation	CuKα (λ = 1.54184)	MoKα (λ = 0.71073)	CuKα (λ = 1.54184)	MoKα (λ = 0.71073)
2Θ range for data collection/°	8.066 to 152.78	6.156 to 59.594	8.066 to 152.226	5.95 to 50.698
Data/restraints/parameters	5243/0/355	6605/4/354	5192/0/355	4572/1/345
Goodness-of-fit on F^2	1.028	1.054	1.04	1.15
Final *R* indexes [I>=2σ (I)]	R_1 = 0.0616, wR_2 = 0.1489	R_1 = 0.0305, wR_2 = 0.0535	R_1 = 0.0431, wR_2 = 0.1100	R_1 = 0.0575, wR_2 = 0.0990
Final *R* indexes [all data]	R_1 = 0.0765, wR_2 = 0.1595	R_1 = 0.0401, wR_2 = 0.0569	R_1 = 0.0462, wR_2 = 0.1137	R_1 = 0.0746, wR_2 = 0.1037
Largest diff. peak/hole / eÅ^{-3}	1.14/-1.69	0.72/-0.59	0.97/-1.34	1.04/-0.79

Table S2 Crystallographic details for **5-7**

	5	6	7
Empirical formula	$C_{41}H_{46}Gd_2N_{12}O_{19}Zn_2$	$C_{41}H_{44}N_{12}O_{20}Tb_2Zn_2$	$C_{40.5}H_{43}Dy_2N_{12}O_{19}Zn_2$
Formula weight	1456.14	1473.46	1457.61
Temperature/ K	120	120.00(10)	120.00(10)
Crystal system	monoclinic	monoclinic	monoclinic
Space group	$P2_1/n$	$P2_1/n$	$P2_1/n$
***a*/Å**	13.7803(2)	13.7871(2)	13.7878(2)
***b*/Å**	11.09944(17)	11.07613(20)	11.0735(2)
***c*/Å**	16.7197(3)	16.6653(3)	16.6729(2)
α/°	90	90	90
β/°	93.8200(15)	93.9182(15)	93.8880(10)
γ/°	90	90	90
Volume/Å^3	2551.66(7)	2538.98(8)	2539.75(7)
Z	2	2	2
ρ_{calc}g/cm^3	1.895	1.927	1.906
μ/mm^{-1}	18.353	15.27	17.285
***F*(000)**	1432	1448	1428
Crystal size/mm^3	0.2451 × 0.046 × 0.0251	0.1471 × 0.0303 × 0.021	0.1179 × 0.0437 × 0.0302
Radiation	CuKα (λ = 1.54184)	CuKα (λ = 1.54184)	CuKα (λ = 1.54178)
2Θ range for data collection/°	8.056 to 153.152	8.058 to 152.496	8.058 to 152.324
Data/restraints/parameters	5325/0/335	5268/108/350	5260/1/353
Goodness-of-fit on F^2	1.049	1.034	1.033
Final *R* indexes [I>=2σ (I)]	R_1 = 0.0421, wR_2 = 0.1072	R_1 = 0.0433, wR_2 = 0.1100	R_1 = 0.0450, wR_2 = 0.1144
Final *R* indexes [all data]	R_1 = 0.0441, wR_2 = 0.1094	R_1 = 0.0480, wR_2 = 0.1144	R_1 = 0.0498, wR_2 = 0.1177
Largest diff. peak/hole / eÅ^{-3}	0.82/-1.77	0.93/-1.18	0.97/-1.46

Table S3 Crystallographic details for **8-11**

	8	**9**	**10**	**11**
Empirical formula	$C_{42}H_{48}Gd_2N_{10}Ni_2O_{18}$	$C_{42}H_{48}Dy_2N_{10}Ni_2O_{18}$	$C_{45}H_{46}N_{12}Ni_2O_{18}Y_2$	$C_{46}H_{50}Dy_2N_{11}O_{18}Zn_2$
Formula weight	1412.82	1423.32	1338.18	1500.71
Temperature/ K	120.00(10)	150	120.01(10)	120.01(10)
Crystal system	monoclinic	monoclinic	monoclinic	monoclinic
Space group	*C*2/*c*	*C*2/*c*	*C*2/*c*	*C*2/*c*
***a*/Å**	22.5913(8)	22.647(3)	22.6107(3)	22.7651(12)
***b*/Å**	11.1919(3)	11.1732(12)	11.16180(10)	11.2274(5)
***c*/Å**	21.6244(8)	21.934(2)	21.6064(2)	21.7967(11)
α/°	90	90	90	90
β/°	110.105(4)	110.0250(10)	110.1240(10)	110.380(6)
γ/°	90	90	90	90
Volume/Å^3	5134.3(3)	5214.5(10)	5120.04(10)	5222.4(5)
Z	4	4	4	4
ρ_{calc}g/cm^3	1.828	1.813	1.736	1.909
μ/mm^{-1}	3.353	3.623	4.511	3.821
***F*(000)**	2792	2808	2712	2956
Crystal size/mm^3	0.267 × 0.105 × 0.05	0.132 × 0.095 × 0.055	0.126 × 0.071 × 0.05	0.18 × 0.139 × 0.083
Radiation	MoKα (λ = 0.71073)	MoKα (λ = 0.71073)	CuKα (λ = 1.54184)	MoKα (λ = 0.71073)
2Θ range for data collection/°	6.438 to 59.464	4.274 to 56.584	8.33 to 153.028	6.166 to 58.528
Data/restraints/parameters	6753/0/358	6093/0/337	5333/0/365	6643/0/350
Goodness-of-fit on *F*^{2}	1.113	1.045	1.076	0.953
Final *R* indexes [I>=2σ (I)]	R_1 = 0.0332, wR_2 = 0.0575	R_1 = 0.0403, wR_2 = 0.1017	R_1 = 0.0431, wR_2 = 0.1140	R_1 = 0.0442, wR_2 = 0.0808
Final *R* indexes [all data]	R_1 = 0.0417, wR_2 = 0.0601	R_1 = 0.0635, wR_2 = 0.1112	R_1 = 0.0440, wR_2 = 0.1153	R_1 = 0.0756, wR_2 = 0.0858
Largest diff. peak/hole / eÅ^{-3}	1.06/-0.67	1.78/-1.09	0.71/-1.45	1.87/-1.30

Chapter 4: Heptanuclear disc-like stuctures [$Cd^{II}_4Ln^{III}_3$]

4.1 Introduction

In the previous chapters the effect of 3*d*-4*f* exchange interactions on the SMM behaviour of the 4*f* ions was investigated. These systems showed small U_{eff} values and the J_{LnNi} interaction reduced these further. In an attempt to increase the magnitude of the energy barrier, a different approach was taken. A heterometallic polynuclear system with 4*f* ions and diamagnetic transition metals combined with a structural motif that separates the 4*f* ions to reduce exchange interactions was investigated. The system is a heptanuclear $[Cd_4Dy_3]$, possessing a disc-like (centred hexagon) structure.

There are many examples of homo and heterometallic *d*-block clusters of this structure type, however there are only a few examples containing 4*f* ions.[1-6] These include $[Gd_7(OH)_6(thmeH_2)_5(tpa)_6(MeCN)_2](NO_3)_2$ and $[Dy_7(OH)_6(thmeH_2)_5(tpa)_6(MeCN)_2](NO_3)_2$ complexes reported in 2011, synthesised with the tripodal alcohol tris(hydroxymethyl)ethane ($thmeH_3$) and triphenylacetic acid (tpaH).[4] The $[Dy_7]$ complex exhibits slow relaxation behaviour with out-of-phase ac susceptibility measurements showing frequency dependent behaviour below 28 K. The $[Gd_7]$ complex displayed a significant magnetocaloric effect due to its spin-frustrated topology. Further work afforded insight into the behaviour of infinitely extended frustrated systems, and the presence of orbital degeneracy in the ground state spin.[2] In 2015, hydrazone based $[Ln_7(L)_6(\mu_3\text{-}OH)_8(NO_3)_4(H_2O)](NO_3)_3$ complexes (where: LH = 2-methoxy-6-(pyridine-2-yl-hydrazonomethyl) phenol ; Ln = Gd, Tb, Dy, Ho and Er) were synthesised and their magnetic properties analysed.[3] The $[Dy_7]$ analogue has three distinct Dy geometries. Three of the Dy ions are DyO_9 and two DyO_7N_2 coordination motifs, with both adopting capped square antiprisms, and the final two are DyN_4O_4 with geometries describing a triangular dodecahedra.[3] However, with these distinct geometries no out-of-phase ac susceptibility signals were observed. There are also a few examples of heterometallic complexes with this centred hexagonal architecture, including $[Co^{II}_2Dy^{III}_5(\mu_3\text{-}OH)_6(L)_2(piv)_8(NO_3)_4]$ (**fig. 1**) and $[Co^{II}_3Dy^{III}_4(\mu_3\text{-}OH)_6L_6\text{-}(CF_3SO_3)](ClO_4)_5$ complexes reported in 2015, the latter of which showed frequency dependence below 4 K (where HL = (E)-4-(2-hydroxy-3-methoxybenzylideneamino)-2,3-dimethyl-1-phenyl-1,2-dihydropyrazol-5-one).[1, 6]

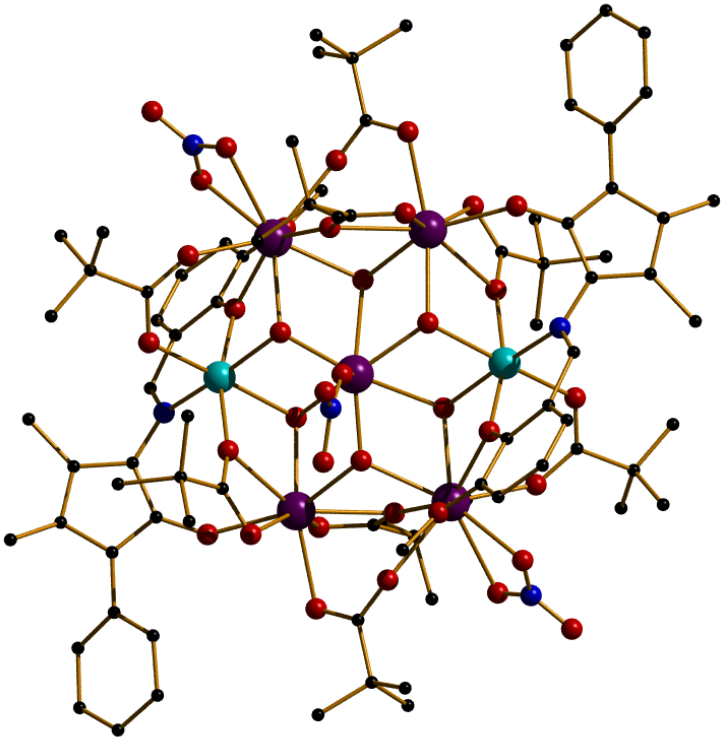

Figure 1 Molecular structure of $[Co^{II}_2Dy^{III}_5(\mu_3\text{-}OH)_6(L)_2(piv)_8(NO_3)_4]$. Colour scheme: Dy, purple; Co, aqua; O, red; N, blue; C, black. H atoms removed for clarity. [1]

The major focus in the field of lanthanide single-molecule magnets has been towards mononuclear 4*f* systems in order to better understand magneto-structural relationships in "simple" systems, since even the exchange between just two Ln^{III} ions results in a drastic increase in complexity.[7-9] A number of examples indicate that even weak interactions between neighbouring lanthanides can dramatically alter, either improving or hindering, the dynamic magnetic properties of the molecule.[7, 10-12] Understanding the nature of 4*f*-4*f* interactions and their effect on relaxation behaviour has improved, but still poses a great challenge due to the complexity stemming from the presence of significant anisotropy and non-negligible crystal field effects.[7]

There are several systems in which the exchange interactions combined with certain topologies can produce unusual magnetic phenomena. 4*f* and 3*d*-4*f* systems with triangular topologies have been studied extensively, showing slow relaxation behaviour, toroidal magnetic moments and spin-frustration effects.[13-20] The tri-dysprosium complex $[\{(thd)_3Dy\}_3HAN]$ of the tritopic ligand hexazaatrinaphthylene (HAN) reported in 2016 is an example of a frustrated system, but it does not display a toroidal magnetic moment (**fig**. **2**).[21]

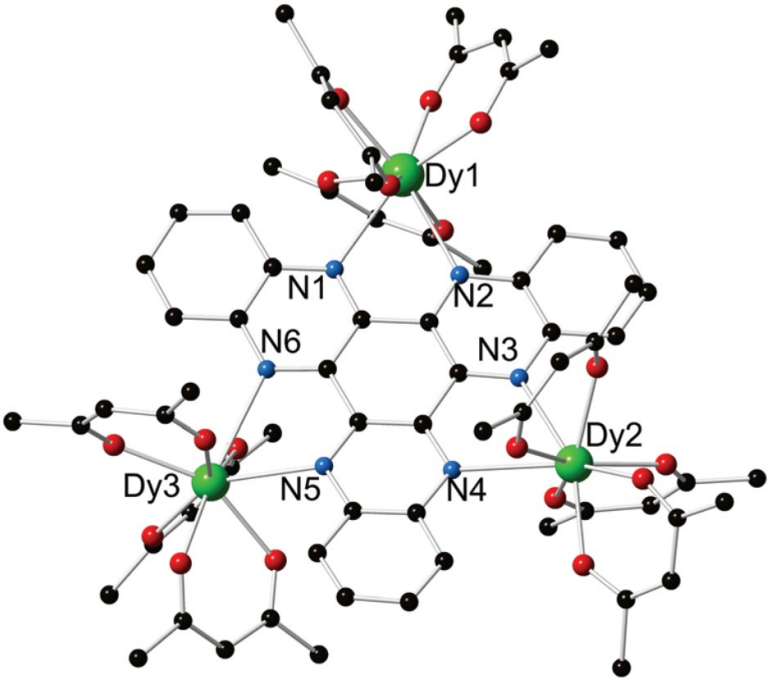

Figure 2 Molecular structure of [{(thd)$_3$Dy}$_3$HAN]. Colour scheme: Dy, green; O, red; N, blue; C, black.[21]

The Dy^{III} ions have two distinct geometries with distorted dodecahedral DyO_6N_2 environments resulting in two different relaxation pathways with U_{eff} = 52 and 42 cm^{-1}. The average intramolecular Dy-Dy distance is 8.122 Å. Frustration effects are common in highly symmetric complexes, particularly extended structures, containing equilateral triangles where the simultaneous presence of AF nearest-neighbour exchange cannot be satisfied. The parent system for such species is the kagomé lattice (**fig**. **3**) whose structure consists of corner (vertex) sharing triangles. An example of this lattice type is the pyrochlore lattice.[22-24]

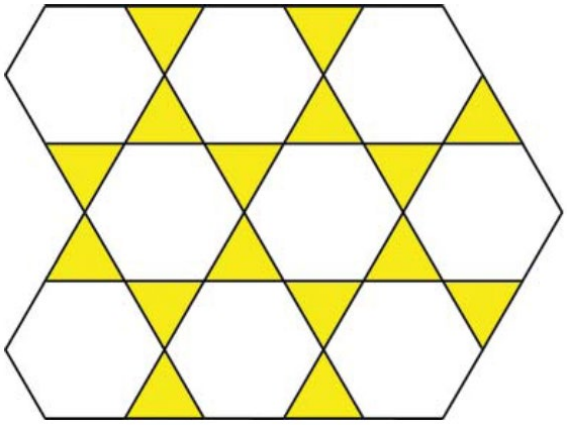

Figure 3 Illustration of a kagomé lattice.[23]

There are only a handful of examples of Cd^{II}-4*f* containing heterometallic complexes, including the phthalocyanine based sandwich complexes.[25-27] Notable examples are $[Tb(obPc)_2]Cd[Tb(obPc)_2]$ and $[Tb(obPc)_2]Cd(obPc)Cd[Tb(obPc)_2]$ complexes (where obPc = dianon of 2,3,9,10,16,17,23,24-octabutoxy-phthalocyanine) reported in 2012, both showing frequency dependent ac susceptibility signals below 40 K, with the Tb^{III} ions well separated in order to reduce the exchange interactions.[26] The advantage of using Cd^{II} in a heterometallic complex is that it is diamagnetic and results in longer M^{II}-ligand bonds compared to other diamagnetic metals such as Zn^{II}. Heterometallic complexes with diamagnetic metals have been shown to improve SMM behaviour of 4*f* based systems as they provide a method of internal dilution. For diamagnetic ions that are directly connected to the lanthanide ions by bridging ligands – the bridging atom is polarized and enhances the charge on the ligand atom. This has been proven to reduce wave function mixing and enhances the ground-state – excited-state energy gap. [28-31]

Certain mononuclear and polynuclear systems have been reported to possess multiple relaxation processes, predominantly accessed through applied magnetic fields and dilute samples.[32-38] In the $[Ln_4K_2O(O^tBu)_{12}]\cdot C_6H_{14}$ compound reported in 2013, site dilution and lattice dilution methods were used to elucidate the origin of relaxation pathways, some of which become uncompetitive due to the reduction in exchange interactions.[36] Recent theoretical work has suggested that multiple relaxation pathways can be of intramolecular origin.[39]

Herein, the synthesis and structural and magnetic characterisation of a series of novel heptanuclear, disc-like complexes of general formula $[Cd^{II}_4(Dy^{III}_{(3-n)}Y^{III}_n)(hmp)_{12}(NO_3)_3](ClO_4)_2\cdot 3MeCN$ (where n = 0, 1, 2 or 3) is shown. These are the first reported examples of heterometallic compounds of this structure-type containing diamagnetic transition metal and 4*f* ions. These molecules have significant spin reversal relaxation barriers and exhibit multiple relaxation processes in the presence of an applied magnetic field when dilute. The three lanthanide ions are arranged in a triangular topology and are separated within the molecule, minimising the exchange interactions. Site dilution, lattice dilution and solution measurements were employed in conjunction with theoretical calculations in order to model the potential relaxation mechanisms.

4.2 Experimental

4.2.1 Materials

All reactions were carried out under aerobic conditions. Chemicals and solvents were obtained from Sigma Aldrich and Alfa Aesar and used without further purification.

4.2.2 Synthetic Procedure

$[Cd^{II}_4Dy^{III}_3(hmp)_{12}(NO_3)_3](ClO_4)_2 \cdot 3MeCN$ (1)

$Cd(ClO_4)_2 \cdot 6H_2O$ (0.420 g, 1 mmol) and $Dy(NO_3)_3 \cdot 6H_2O$ (0.438 g, 1 mmol) were dissolved in a mixture of MeCN (12 mL) and MeOH (8 mL), followed by the addition of hmpH (0.47 mL, 5mmol) and NEt_3 (0.69 mL, 5 mmol). The solution was stirred for 24 hours before being filtered. The solution was then layered with Et_2O via vapour diffusion. After 72 hours large block shaped crystals of **1** had formed. Elemental analysis calculated (found) for **1**: $Cd_4Dy_3C_{72}H_{72}O_{29}N_{15}Cl_2$*: C, 33.01 (33.40); H, 2.77 (2.88); N, 8.02 (8.26); Dy, 18.61 (18.58). Mass spectrometry data are shown in **fig**. **S1**-**4** which shows 100% $[Cd_4Dy_3]$. Powder diffraction is shown in **fig**. **3**.

$[Cd^{II}_4Dy^{III}_2Y^{III}(hmp)_{12}(NO_3)_3](ClO_4)_2 \cdot 3MeCN$ (2)

$Cd(ClO_4)_2 \cdot 6H_2O$ (0.420 g, 1 mmol), $Dy(NO_3)_3 \cdot 6H_2O$ (0.219 g, 0.5 mmol) and $Y(NO_3)_3 \cdot 6H_2O$ (0.958 g, 0.25 mmol) were dissolved in a mixture of MeCN (12 mL) and MeOH (8 mL), followed by the addition of hmpH (0.47 mL, 5mmol) and NEt_3 (0.69 mL, 5 mmol). The solution was stirred for 24 hours before being filtered. The solution was then layered with Et_2O via vapour diffusion. After 72 hours colourless plate shaped crystals of **2** had formed. Elemental analysis calculated (found) for **2**: $Cd_4Dy_2YC_{72}H_{72}O_{29}N_{15}Cl_2$*: C, 33.97 (33.78); H, 2.85 (2.85); N, 8.25 (8.24); Dy, 12.77 (12.75); Y, 3.49 (3.55). Mass spectrometry data are shown in **fig**. **S5**-**9** which shows approx. 78.9% $[Cd_4Dy_2Y]$ and 21.1% $[Cd_4DyY_2]$, with traces of $[Cd_4Dy_3]$ and $[Cd_4Y_3]$. Powder diffraction is shown in **fig**. **3**.

$[Cd^{II}_4Dy^{III}Y^{III}_2(hmp)_{12}(NO_3)_3](ClO_4)_2 \cdot 3MeCN$ (3)

$Cd(ClO_4)_2 \cdot 6H_2O$ (0.420 g, 1 mmol), $Dy(NO_3)_3 \cdot 6H_2O$ (0.109 g, 0.25 mmol) and $Y(NO_3)_3 \cdot 6H_2O$ (0.192 g, 0.5 mmol) were dissolved in mixture of MeCN (12 mL) and MeOH (8 mL), followed by the addition of hmpH (0.47 mL, 5mmol) and NEt_3 (0.69 mL, 5 mmol). The solution was stirred for 24 hours before being filtered. The solution was then layered with Et_2O via vapour diffusion. After 72 hours colourless plate shaped crystals of **3** had formed. Elemental analysis calculated (found) for **3**: $Cd_4DyY_2C_{72}H_{72}O_{29}N_{15}Cl_2$*: C, 34.98 (34.53); H, 2.94 (2.95); N, 8.50

(8.39); Dy, 6.57 (6.20); Y, 7.19 (6.82). Mass spectrometry data are shown in **fig**. **S10**-**14** which shows approx. 58.79% (82.4% of magnetic components) [Cd_4Dy_2Y], 21.1% (17.6% of magnetic components) [Cd_4DyY_2] and 28.65% [Cd_4Y_3] with traces of [Cd_4Dy_3]. Powder diffraction is shown in **fig**. **3**.

[$Cd^{II}_4Y^{III}_3(hmp)_{12}(NO_3)_3$]($ClO_4$)$_2$·3MeCN (4)

$Cd(ClO_4)_2·6H_2O$ (0.420 g, 1 mmol) and $Y(NO_3)_3·6H_2O$ (0.383 g, 1 mmol) were dissolved in a mixture of MeCN (12 mL) and MeOH (8 mL), followed by the addition of hmpH (0.47 mL, 5mmol) and NEt_3 (0.69 mL, 5 mmol). The solution was stirred for 24 hours before being filtered. The solution was then layered with Et_2O via vapour diffusion. After 72 hours colourless plate shaped crystals of **4** had formed. Elemental analysis calculated (found) for **4**: $Cd_4Y_3C_{72}H_{72}O_{29}N_{15}Cl_2$*: C, 36.05 (35.74); H, 3.03 (3.03); N, 8.76 (8.73); Y, 11.12 (11.13). Mass spectrometry data are shown in **fig**. **S15**-**18** which shows 100% [Cd_4Y_3]. Powder diffraction shown in **fig**. **3**.

*assuming the sample had fully desolvated

4.2.3 Magnetic studies

The magnetic susceptibility measurements were carried out on a Quantum Design PPMS magnetometer with the ACMS option, and a MPMS (SQUID) magnetometer, with operating temperatures ranging from 1.8 and 300 K and dc-applied fields ranging from 0 to 7 T. Ac susceptibility frequency measurement ranges for the MPMS and PPMS are 0.5-1000 Hz and 1000-10000 Hz, respectively. In-phase (χ_M') and out-of-phase (χ_M'') ac susceptibility measurements were carried out and plotted as a function of temperature and frequency. Microcrystalline samples were contained in a gelatine capsule and dispersed in eicosane to avoid sample movement. Diamagnetic corrections were applied to the observed paramagnetic susceptibilities using Pascal's constants.

4.2.4 Mass Spectrometry

Mass Spectrometry measurements of **1**-**4** were performed on a Synapt G2 (Waters, Manchester, UK) mass spectrometer, using a direct infusion electrospray ionisation source (ESI), controlled using Masslynx v4.1 software. All of the scans were for positive ions. Samples were dissolved in MeCN:MeOH (9:1) at 100 µM. Prior to analysis, the instrument was calibrated using a solution of sodium iodide (2 mg/mL) in 50:50 water:isopropanol. Capilliary voltages were adjusted between 1.5 and 2.5 kV to optimise spray quality. The sample cone

and the extraction cone voltage were minimised to reduce breakdown of the molecules. Source temperature was set at 8 °C. The data was analysed using the MassLynx v4.1 software.

4.2.5 Crystallography

A suitable crystal of each complex was selected and mounted on a MITIGEN holder in Paratone oil on an Agilent Technologies SuperNova diffractometer. A MoKα source was used for **1**-**4**. The crystals were kept at *T* = 120.0 K for **2**-**4** and at *T* = 293 for **1**. Using Olex2, the structure was solved with the ShelXT structure solution program, using the Direct Methods solution method.[40, 41] The models were refined with ShelXL using Least Squares minimisation.[40] Crystal structures **1**-**4** have disordered MeCN within the unit cell. Crystallographic data and refinement parameters for **1**-**4** are summarised in **Table 1**.

4.2.6 Inductively Couple Plasma-Mass Spectrometry

All samples were prepared in dissolutions of 4-5 mg of sample in 4% aqua regia and ICP was performed on a Perkin Elmer Optima 5300 DV ICP-EOS.

4.2.7 X-ray Powder Diffraction

The X-ray powder diffraction data of capillary loaded powder samples of **1**-**4** were measured on a Bruker D8 Advance, wavelength 1.54056 Å from 5-30° 2θ (0.22° intervals) at room temperature. The experimental X-ray powder diffraction data was compared to the calculated spectrum of **1**, as shown in **fig**. **4**.

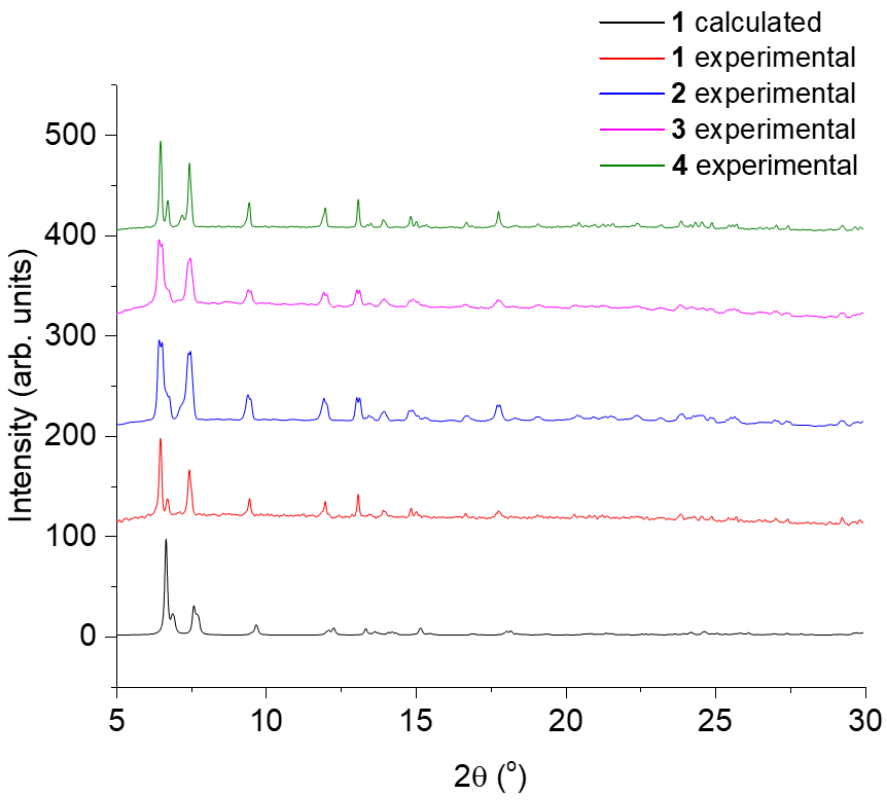

Figure 4 X-ray powder diffraction for **1**-**4**.

4.2.9 Computational details

Ab initio CASSCF[38]+RASSI-SO[39]+SINGLE_ANISO[40] calculations were performed on all Dy^{III} ions of complex **1** individually, using the single-crystal structure data in MOLCAS 8.0[41] suite to substitute all the Dy^{III} ions with diamagnetic La^{III} ions, except the one being calculated. We have used the [C.ANO-RCC...3s2p], [N.ANO-RCC...3s2p1d], [O.ANO-RCC...3s2p1d], [H.ANO-RCC...2s], [Lu.ANO-RCC...7s6p4d2f1g] and [Dy.ANO-RCC...8s7p5d3f2g1h] basis sets for our *ab initio* calculations.[42] For CASSCF calculations on the Dy-mononuclear fragments, we have considered nine electrons in the seven active orbitals the 4*f* ions possess. Additionally, in the RASSI-SO step, 21 roots for sextet spin multiplicity have been considered.[43] The resultant spin-orbit multiplet has been further used to compute local magnetic properties via the SINGLE_ANISO approach. Because of the symmetry of the molecule, we have assumed the same type of magnetic coupling behaviour between all three Dy^{III} ions ($J_{Dy(x)Dy(b)}$). This has been computed by fitting *ab initio* POLY_ANISO with the experimental data.[44]

Table 1 Crystallographic details for **1**-**4**.

	1	**2**	**3**	**4**
Empirical formula	$C_{76}H_{78}Cd_4Cl_2Dy_3N_{17}O_{29}$	$C_{72}H_{72}Cd_4Cl_2Dy_{1.92}N_{15}O_{29}Y_{1.09}$	$C_{76}H_{78}Cd_4Cl_2Dy_{0.91}N_{17}O_{28.97}Y_{2.1}$	$C_{72}H_{72}Cd_4Cl_2N_{15}O_{29}Y_3$
Formula weight	2701.55	2539.6	2547.13	2398.67
Temperature/ K	293(2)	120.00(10)	120.01(10)	120.01(10)
Crystal system	triclinic	monoclinic	monoclinic	monoclinic
Space group	*P*$\bar{1}$	*C*2/c	*C*2/c	*C*2/c
***a*/Å**	14.7171(3)	14.7014(3)	14.7066(7)	14.6812(4)
***b*/Å**	14.8319(3)	25.9408(5)	25.9254(11)	25.8652(7)
***c*/Å**	26.5149(5)	26.3213(5)	26.3216(16)	26.2813(9)
α/°	89.359(2)	90	90	90
β/°	88.744(2)	90.717(2)	90.567(5)	90.169(3)
γ/°	60.895(2)	90	90	90
Volume/Å^3	5055.71(19)	10037.3(3)	10035.3(9)	9979.8(5)
Z	2	4	4	4
ρ_{calc}g/cm^3	1.775	1.681	1.686	1.596
μ/mm^{-1}	3.144	2.986	2.825	2.689
***F*(000)**	2618	4943	5009	4736
Crystal size/mm^3	0.563 × 0.2023 × 0.0755	0.456 × 0.344 × 0.325	0.404 × 0.357 × 0.192	0.488 × 0.312 × 0.051
Radiation	MoKα (λ = 0.71073)	MoKα (λ = 0.71073)	MoKα (λ = 0.71073)	MoKα (λ = 0.71073)
2Θ range for data collection/°	5.644 to 65.946	5.466 to 59.354	6.27 to 59.44	5.616 to 50.7
Data/restraints/parameters	35142/48/1228	13164/216/568	12538/216/597	9121/309/649
Goodness-of-fit on *F*^{2}	1.052	1.231	1.138	1.165
Final *R* indexes [I>=2σ (I)]	R_1 = 0.0556, wR_2 = 0.1042	R_1 = 0.0761, wR_2 = 0.1747	R_1 = 0.1375, wR_2 = 0.3236	R_1 = 0.0911, wR_2 = 0.1904
Final *R* indexes [all data]	R_1 = 0.0778, wR_2 = 0.1095	R_1 = 0.0836, wR_2 = 0.1774	R_1 = 0.1554, wR_2 = 0.3334	R_1 = 0.1029, wR_2 = 0.1950
Largest diff. peak/hole / eÅ^{-3}	2.03/-5.05	2.95/-6.39	4.59/-4.22	2.04/-5.62

4.3 Results and discussion

4.3.1 Structural description

Single-crystal X-ray diffraction measurements reveal that **1** crystallises in the triclinic space group *P*$\bar{1}$. The molecular structure of compound **1** is shown in **fig**. **5**. Complexes **2**-**4** all crystallise in the monoclinic space group *C*2/*c*.

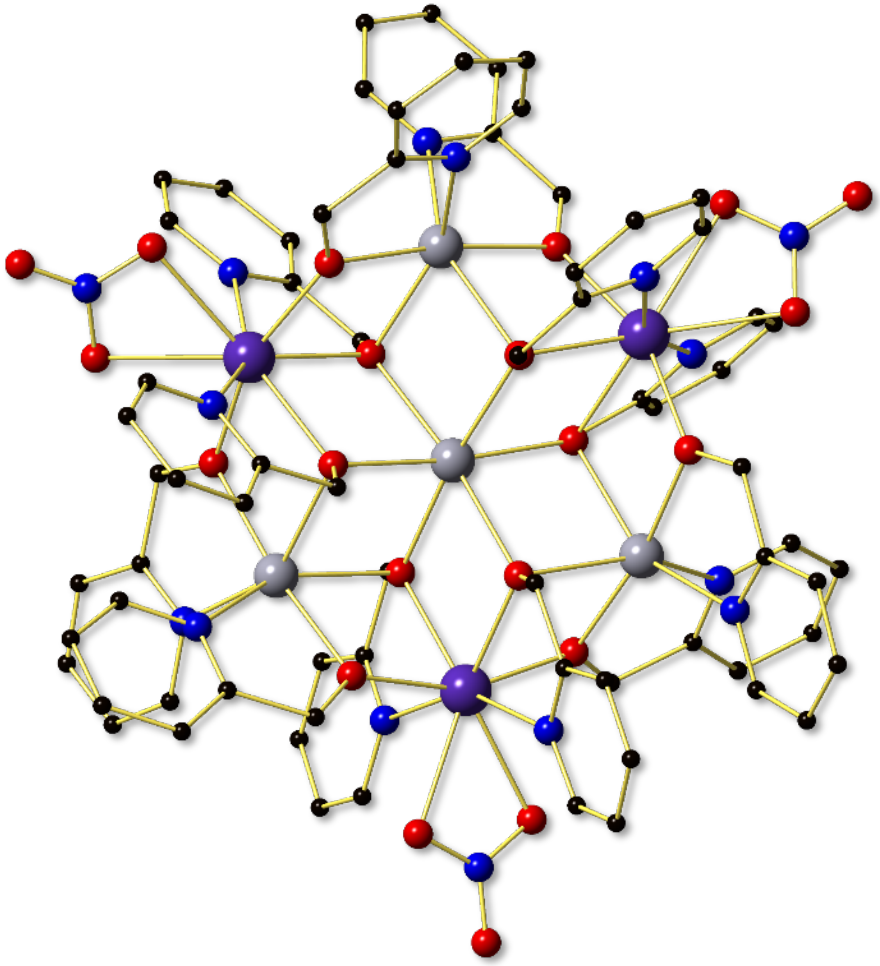

Figure 5 Crystal structure of the cation of **1**. Colour scheme: Dy, purple; Cd, grey; O, red; N, blue; C, black (H atoms, solvent molecules and counter-ions omitted for clarity).

Complexes **1**-**4** were found to be heterometallic heptanuclear clusters containing four Cd^{II} ions and three Ln^{III} ions. Each Cd^{II} ion is in an octahedral geometry with the outer ions each bridged to two Ln^{III} ions and the central Cd^{II} ions. The Cd^{II}-Ln^{III} bridging occurs through a μ-O of an hmp^- ligand, the N of which is coordinated to the Cd^{II} (**fig**. **6**(**a**)), and a μ_3-O of another hmp^- ligand, the N of which is coordinated to an Ln^{III} ion (**fig**. **6**(**b**)). The central Cd^{II} ion is bridged to all other metal ions via μ_3-O atoms of hmp^- ligands. An η^2-NO_3^- anion is coordinated to each Ln^{III} ion.

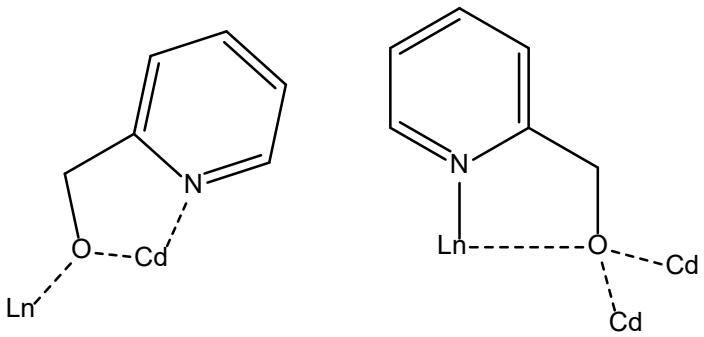

Figure 6 Briding motifs of the hmp^- ligands in **1**-**4**: (**a**) μ-O. (**b**) μ_3-O.

There are two ClO_4^- counter-ions in **1**-**4**. One ClO_4^- in **1** is disordered and part-occupied over two sites (57:43 occupancy). Three disorded MeCN molecules are found between the voids of the clusters. The average intramolecular Ln-Ln distance in **1** is 6.447 Å. In **1** the three Dy^{III} ions are of slightly different geometries (**fig**. **7**). The SHAPE program was used to analyse each of these centres.[42] Dy1 (DyO_6N_2) was found to be a square antiprism, CShM = 3.031 (trangular dodecahedron, CShM = 3.389; Biaugmented trigonal prism, CShM = 3.651). Dy2 (DyO_6N_2) was found to be a biaugmented trigonal prism, CShM = 3.126 (triangular dodecahedron, CShM = 3.314; Square antiprism, CShM = 3.383). Dy3 (DyO_6N_2) was found to be a triangular dodecahedron, CShM = 2.308 (Biaugmented trigonal prism, CShM = 3.634; Square antiprism, CShM = 3.785).

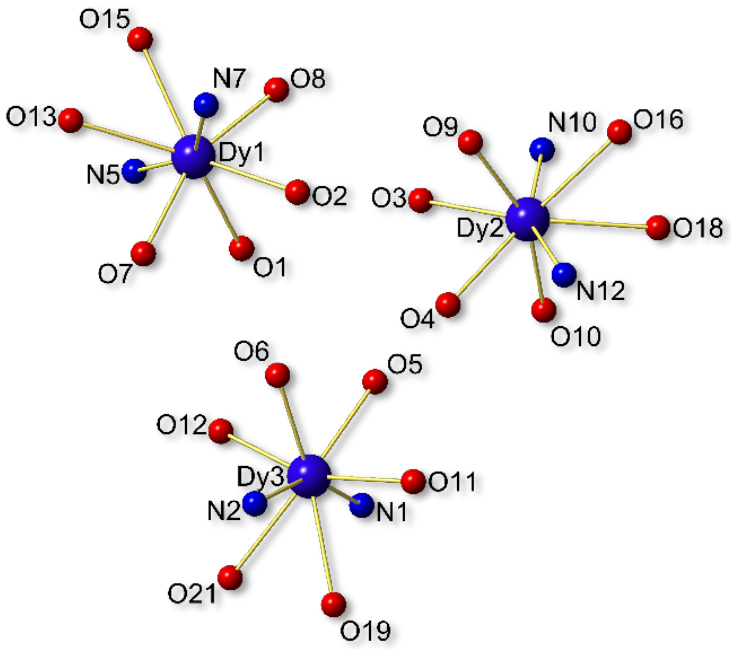

Figure 7 Coordination sphere of the Dy^{III} ions of **1**.

As **2**-**4** are in the monoclinic space group *C*2/*c* there are two different Ln^{III} sites present. As **4** is a pure sample and not a diluted mixture like **2** and **3** the crystallography is more reliable to characterise the geometry of the Ln^{III} sites**.** Samples **2** and **3** have been confirmed by mass spectrometry to be a mixture of $[Cd_4Dy_{3-n}Y_n]$ species (**fig**. **S5**-**14**) and therefore the corresponding single-crystal X-ray data is somewhat unreliable for structural information. In **4** the Y2 (YO_6N_2) site sits on the 2-fold mirror plane and was found to be a square-antiprism, CShM = 3.021 (triangular dodecahedron, CShM = 3.266). Y1 (YO_6N_2), of which there are two related by the 2-fold symmetry, was found to be a triangular dodecahedron, CShM = 2.172 (square-antiprism, CShM = 3.861).

Figs. **8** (**a**) and (**b**) show packing diagrams of the extended structure viewed down the crystallographic *a*-axis and *c*-axis, respectively. Upon close inspection it appears that the intramolecular and intermolecular interactions form a quasi-kagomé lattice with two different non-equilateral triangles, as shown in **fig**. **8** (**b**), where the thick orange lines denote the intramolecular triangular topology and the thin blue lines denote the intermolecular triangular topology. The average intermolecular Ln-Ln distance is 8.688 Å (2.241 Å longer than the intramolecular distance). This distance is similar to that of intramolecular Dy-Dy distances shown in the previously reported frustrated system $[\{(thd)_3Dy\}_3HAN]$ (8.122 Å).[21] **Fig**. **8** (**a**) shows the packing of the sheets of this quasi-kagomé lattice extending along the *ab*-plane.

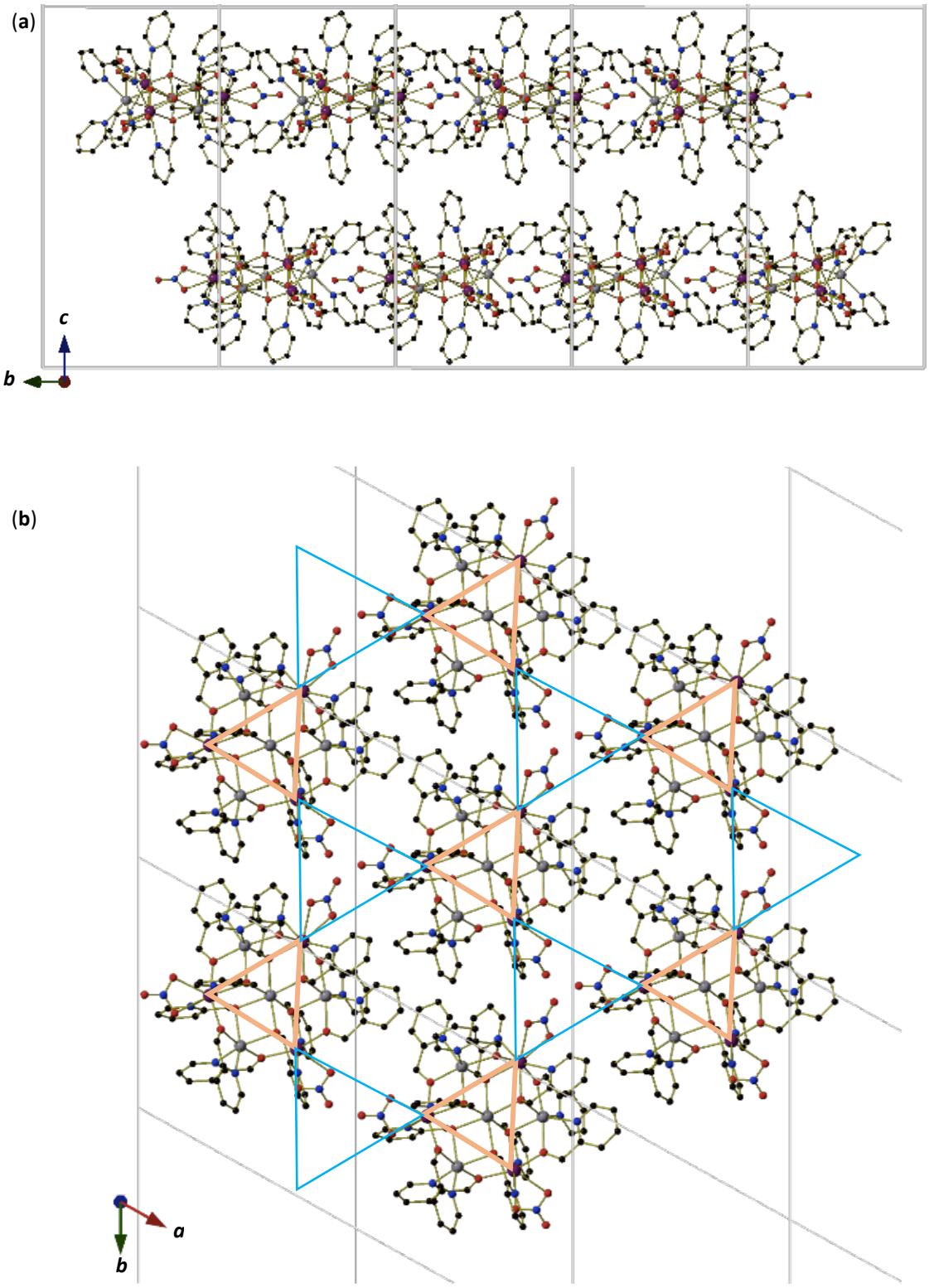

Figure 8 (**a**) Packing viewed along the *a*-axis of **1**. Hydrogen and counter ions/solvent removed for clarity. (**b**) Packing viewed along the *c*-axis of **1**.Thick orange triangle – intramolecular triangular topology. Thin blue triangle – intermolecular triangle. Hydrogen and counter ions/solvent removed for clarity.

4.3.2 Static dc susceptibility measurements

The magnetic properties of **1**-**3** were measured as polycrystalline samples in the 2-300 K temperature range in a 0.1 T applied field. The room temperature $\chi_M T$ value of **1** is 42.6 cm^3 mol^{-1} K, (**fig**. **9**), consistent with three non-interacting Dy^{III} ions, which declines on cooling reaching a minimum of 36.0 cm^3 mol^{-1} K at 2 K due to the depopulation of crystal field states. This is consistent with literature precedent.[7]

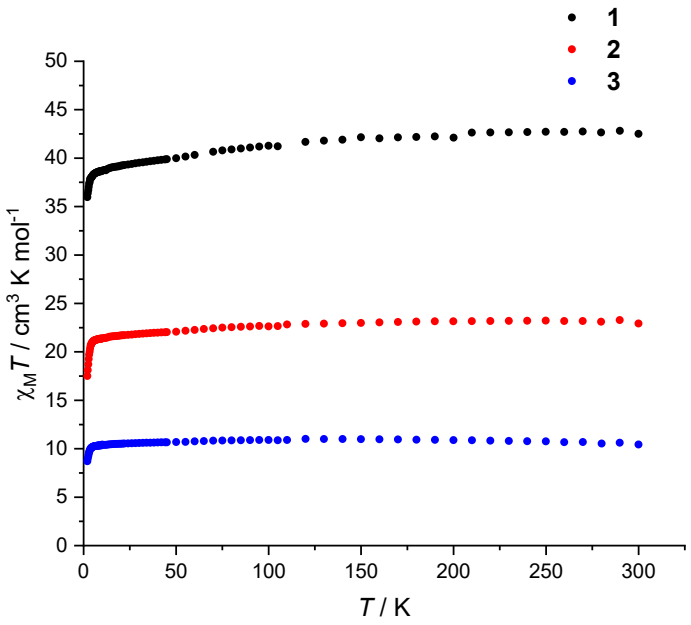

Figure 9 Plots of $\chi_M T$ versus T for **1**-**3** measured in a 0.1 T dc field.

The room temperature value of $\chi_M T$ for **2** (23.2 cm^3 K mol^{-1}) is consistent with an 80% sample of $[Cd_4Dy_2Y]$ in which the Dy^{III} ions are non-interacting, which declines upon cooling to a minimum of 17.50 cm^3 mol^{-1} K at 2 K. The room temperature value of $\chi_M T$ for **3** is 11.0 cm^3 K mol^{-1}, consistent with an 80% sample of $[Cd_4DyY_2]$, which declines upon cooling to a minimum of 8.7 cm^3 mol^{-1} K at 2 K. Due to there being a mixture of $[Cd_4Dy_3]$, $[Cd_4Dy_2Y]$, $[Cd_4DyY_2]$ and $[Cd_4Y_3]$ (see mass spectrometry, **fig**. **S1**-**18**) this data could not be fitted. Magnetisation (M) versus field (H) data of **1**-**3** at T = 2 K saturate at 13.94 μ_B mol^{-1} (15.3 μ_B mol^{-1} expected), ~8.84 μ_B mol^{-1} and 4.36 μ_B mol^{-1}, respectively (**fig**. **10**).

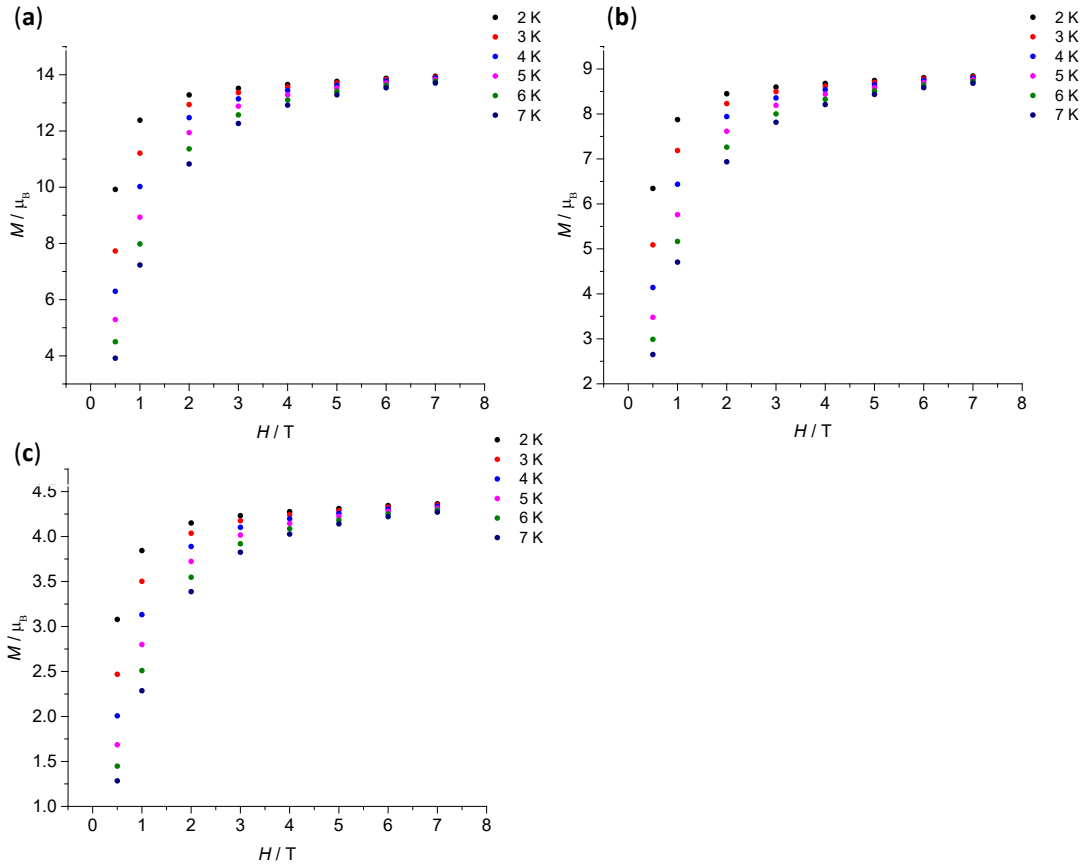

Figure 10 Magnetisation (*M*) as a function of applied magnetic field (*H*) at *T* = 2-7 K for (**a**) **1**, (**b**) **2** and (**c**) **3**.

4.3.3 Ac susceptibility measurements

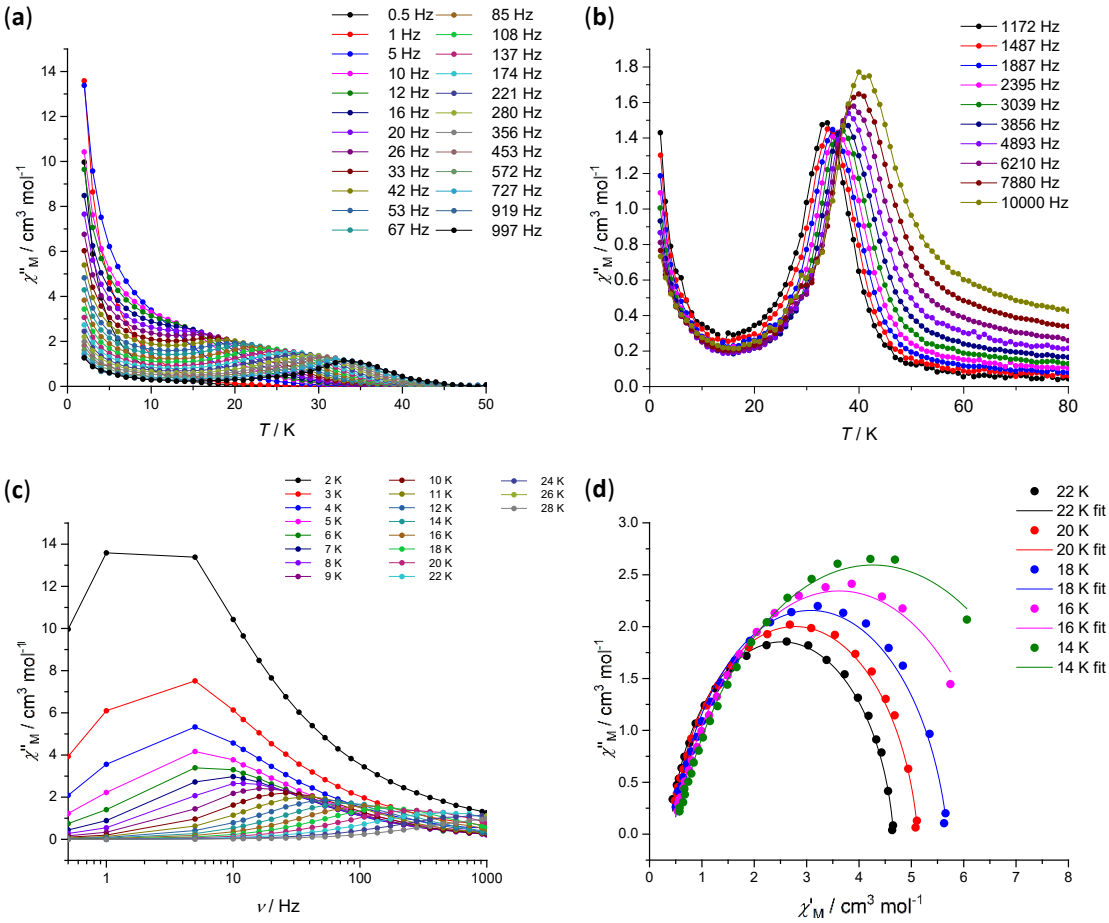

Figure 11 Dynamic behaviour of **1**: (**a**) χ_M'' measured as a function of temperature from 2-50 K. Lines are a visual guide. (**b**) χ_M'' measured as a function of temperature from 2-80 K. Lines are a visual guide. (**c**) χ_M'' measured as a function of frequency from 2-28 K. Lines are a visual guide. (**d**) Variable temperature Cole-Cole plots from 14-22 K with fittings.

Ac magnetic measurements performed on **1** in zero dc field (**fig**. **11**(**a**)-(**c**)) show temperature and frequency dependent behaviour, indicating slow relaxation of the magnetisation. The out-of-phase ac susceptibility measurements with increasing frequencies up to 10000 Hz (**fig**. **11**(**b**)) show maxima below 50 K, with peaks ranging from approximately 30-50 K. **Fig**. **11**(**c**) shows a single peak at each temperature from 2-36 K as a function of frequency between 0.5-1000 Hz. These signals broaden upon decreasing temperature, increasingly so below 14 K, indicating that there is more than one relaxation pathway active.

The Cole-Cole plots for **1** are shown in **fig**. **11**(**d**) from 14-22 K. They were successfully fitted using **equation 1** shown below.

$$\chi''(\chi) = \frac{\chi_T - \chi_S}{2\tan[\frac{(1+\alpha)\pi}{2}]} + \sqrt{(\chi' - \chi_S)(\chi_T - \chi') + \frac{(\chi_T - \chi_S)^2}{4tan^2[\frac{(1+\alpha)\pi}{2}]}} \qquad (1)$$

The corresponding α values for 22 and 14 K are 0.08786 (±0.00582) and 0.18001 (±0.00684) respectively. A full analysis of all temperatures is shown in **Table S1**. These values indicate that only one relaxation pathway is present at 22 K, however upon decreasing temperature below 14 K the increasing α value and the evident shift to a non-semicircular shape, indicates that more than one relaxation pathway is active.

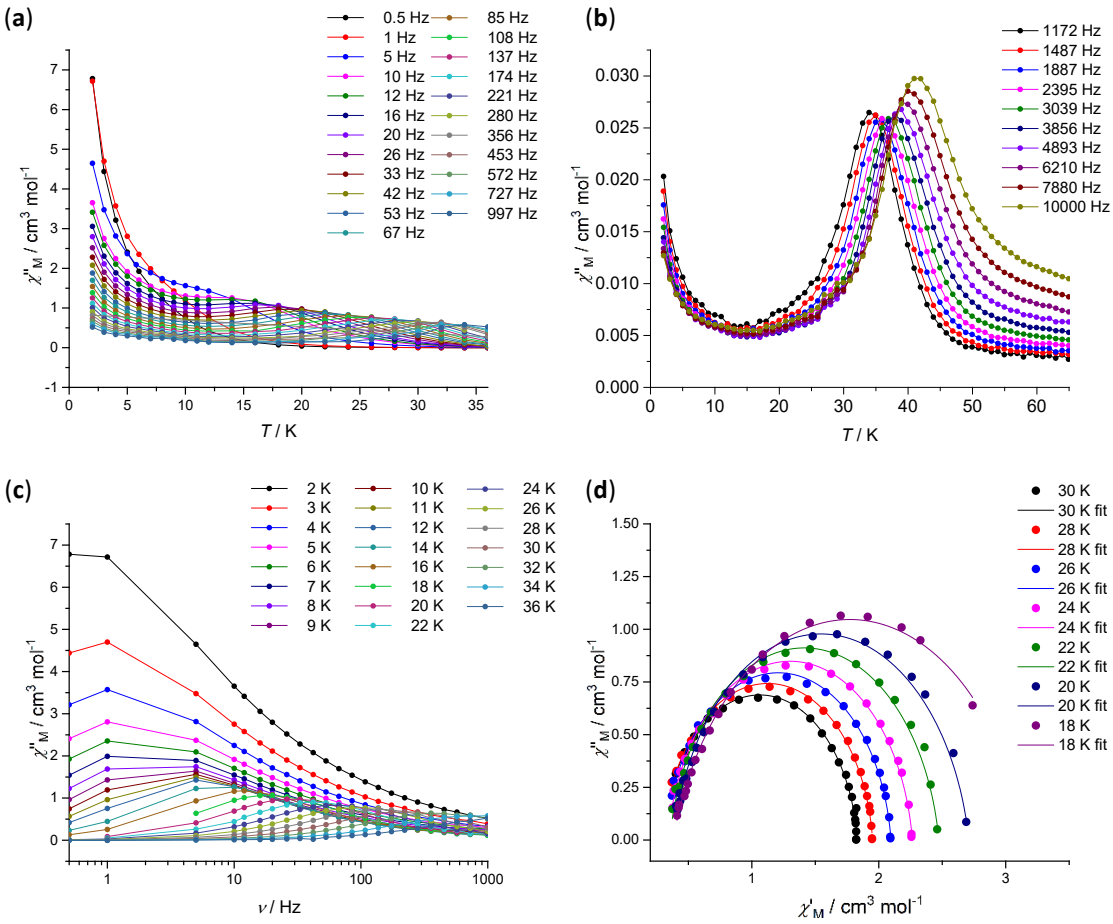

Figure 12 Dynamic Behaviour of **2**: (**a**) Out-of-phase ac susceptibility (χ_M'') measured as a function of temperature from 2-36 K. Lines are a visual guide. (**b**) χ_M'' measured as a function of temperature from 2-65 K. Lines area visual guide. (**c**) χ_M'' measured as a function of frequency from 2-36 K. Lines are a visual guide. (**d**) Variable temperature Cole-Cole plots from 18-30 K with fittings.

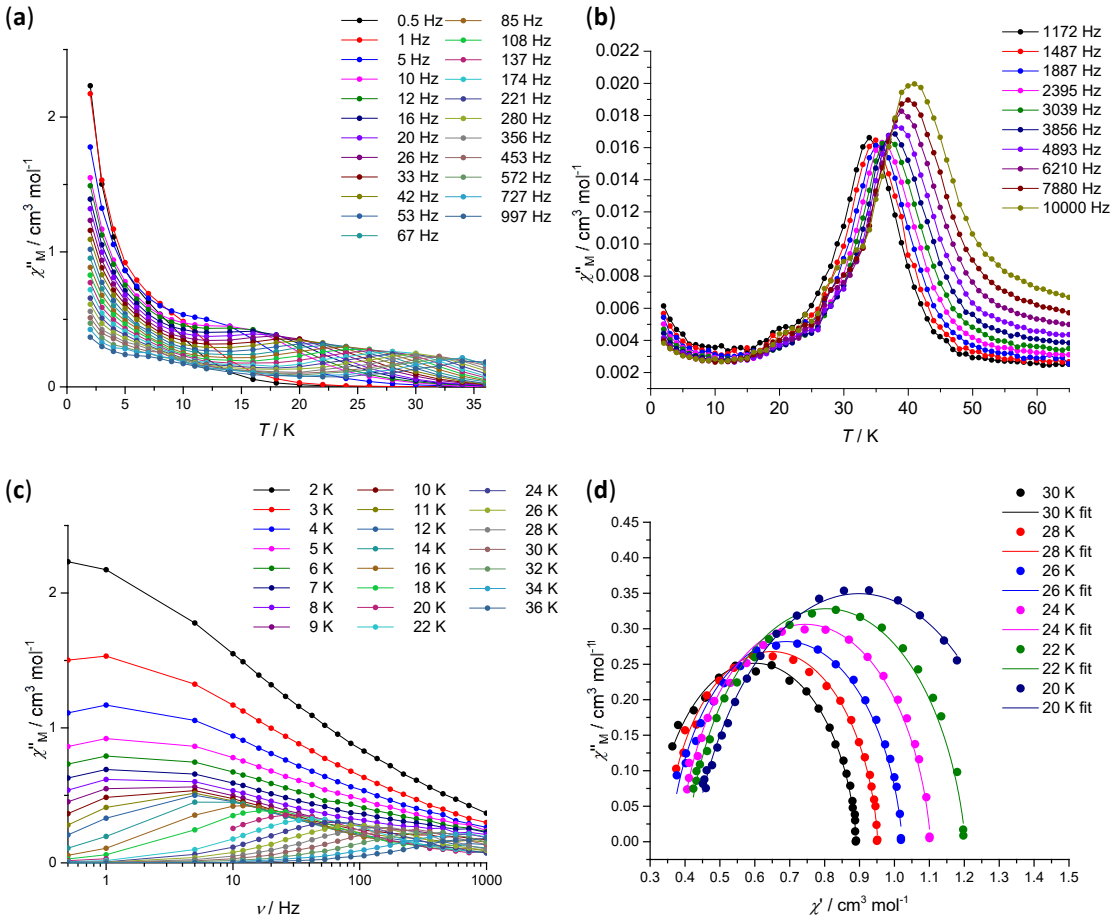

Figure 13 Dynamic Behaviour of **3**: (**a**) Out-of-phase ac susceptibility (χ_M'') measured as a function of temperature from 2-36 K. Lines are a visual guide. (**b**) χ_M'' measured as a function of temperature from 2-80 K. Lines are a visual guide. (**c**) χ_M'' measured as a function of frequency from 2-36 K. Lines are a visual guide. (**d**) Variable temperature Cole-Cole plots from 20-30 K with fittings.

Ac magnetic susceptibility measurements performed on **2** and **3** in zero dc field (**fig**. **12** and **13**) show temperature and frequency dependent behaviour, indicating slow relaxation of the magnetisation similar to that of **1**, but at higher temperatures (**fig**. **11**(**a**)) and frequencies (**fig**. **11**(**c**)), above 22 K and 55 Hz. **Fig**. **12**(**b**) and **13**(**b**) show the 600-10000 Hz out-of-phase ac magnetic susceptibility plots of **2** and **3**, respectively, which show peaks below 41 K at 10000 Hz. These indicate little difference in the high frequency region. On examination of both the lower temperature and frequency regions (less than 22 K and 55 Hz) it is clear that there are other relaxation processes active at different rates in both **2** and **3** in comparison to **1**.

The Cole-Cole plots were fitted using **equation S1**. The resulting fits for **2** (18-30 K) and **3** (20-30 K) are shown in **figs**. **12**(**d**) and **13**(**d**). The corresponding α values for **2** at 30 K and 22 K are 0.06928 (±0.01346) and 0.09514 (±0.00957) with the χ_S values remaining similar from 30-18 K (0.29343 – 0.34223), indicating that at higher temperatures the relaxation is almost exclusively via a thermal energy barrier, whilst at lower temperatures there are other relaxation processes active. The corresponding α values for **3** at 30 K and 22 K are 0.09273 (±0.00995) and 0.12347 (± 0.00888), the χ_S values in this temperature range also increase from 30-20 K (0.31257 – 0.42483). These values indicate that there are a mixture of relaxation processes active in this region. A full analysis of the Cole-Cole fits of **2** and **3** is shown in **Tables S2** and **S3**.

4.3.4 Arrhenius Plots

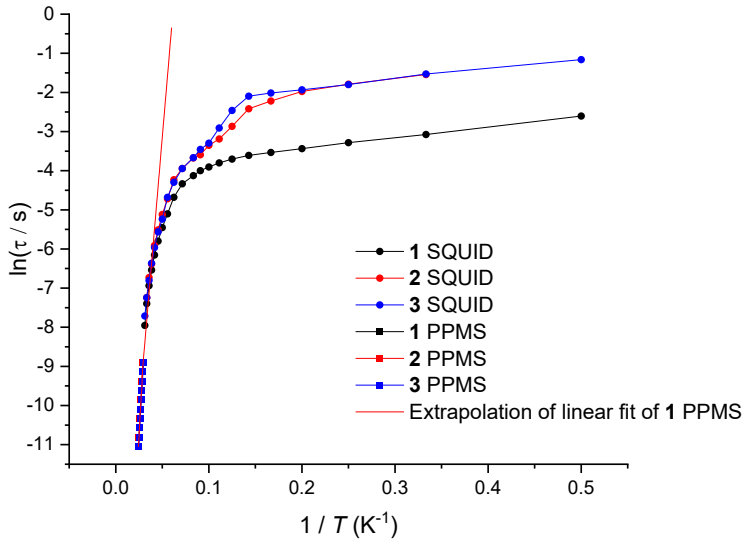

Figure 14 Arrhenius plots for **1** (black), **2** (red) and **3** (blue), constructed from low frequency (filled circles) and high frequency (filled squares) out-of-phase ac susceptibility data. A linear extrapolation of the high frequency region of **1** is shown (red line).

The Arrhenius plots were constructed using the maxima in χ_M'' peaks from the data shown previously using the Arrhenius law, $\tau = \tau_0 \exp(U_{eff}/k_BT)$. A linear Arrhenius fit of the high frequency region (1000-10,000 Hz) was performed and is summarised in **Table 3**.

	1	**2**	**3**
τ_0 (s)	4.940×10^{-10}	4.282×10^{-10}	5.2532×10^{-10}
error (s)	$\pm 1.378 \times 10^{-10}$	$\pm 1.0338 \times 10^{-10}$	$\pm 1.1495 \times 10^{-10}$
U_{eff} (cm^{-1})	295.866	302.22	291.079
error (cm^{-1})	± 8.436	± 7.1895	± 6.2996

Table 3 Arrhenius data for complexes **1**-**3**.

Bearing in mind the high level of error associated with the values used to calculate the U_{eff} values for **1**-**3** they all display similar values with some variability for the high temperature region indicating that the dynamic behaviour is intrinsic to the Dy^{III} ion.[7] Complex **2** appears to have the largest U_{eff}, discounting the error. The low frequency region shows a deviation from the linear regime, indicating that QTM is active. There is a substantial difference shown between **1** and **2** at values of 1/T above 0.1 K^{-1} indicating that QTM has been reduced upon removing one Dy^{III} centre from the molecule. The differences in behaviour between **2** and **3** however is small, and only evident between 10-33 Hz. This could be evidence that with three Dy^{III} centres present (as in **1**) there is an additional effect within the triangular motif that is increasing QTM. This is a weak effect however and is not evident in the higher frequency region (above 174 Hz).

4.3.5 Hysteresis Loops

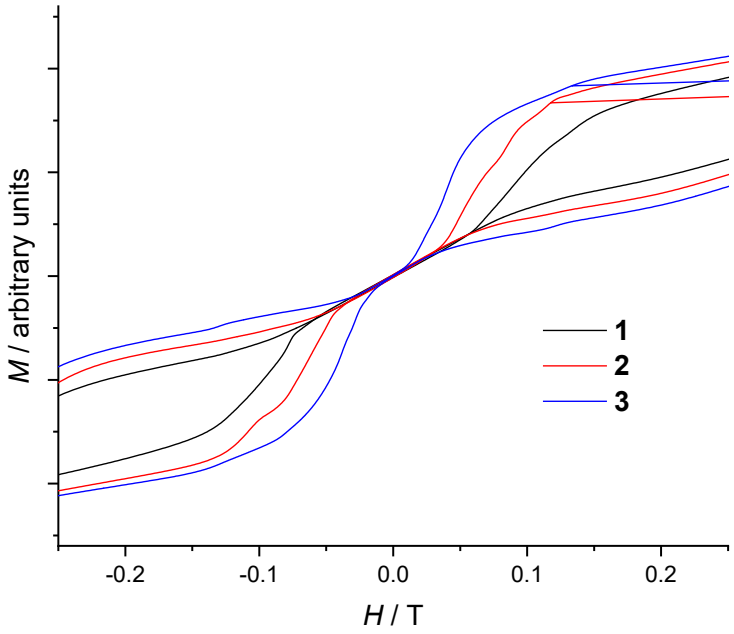

Figure 15 Hysteresis measurements of **1**-**3** at 2 K (0.00264 T/s average sweep rate).

Fig. **15** (**a**) shows the hysteresis measurements of **1**-**3** at 2 K. The magnetisation values have been normalised to allow a comparison of the compounds. Decreasing the number of Dy^{III} centres from three (**1**) to two (**2**) and to one (**3**), there is a clear trend of opening at lower fields. However, they all close at zero due to the QTM rate. The reduction of tunnelling rates observed here coincide with the Arrhenius plots discussed previously (**fig**. **14**). The dipolar interactions, although weak, appear to also increase the QTM rate as seen when comparing **1**-**3**. This results provides a means to understanding the relationship between the 4*f*-4*f*

exchange interactions and the dynamic magnetic behaviour. Computational work was carried out to give further insights into this relationship.

4.4 Computational Work

The relaxation mechanism for each individual Dy^{III} ion has been explored computationally and is described below. This is followed by a discussion of the full polynuclear system where all single-ion anisotropy and magnetic exchange constants are employed to develop the relaxation mechanism for an exchange coupled system.

4.4.1 Single-Ion Magnetic Anisotropy of Complex 1

The anisotropy of all three paramagnetic Dy^{III} ions was calculated individually. The calculated anisotropic *g*-values for complex **1** (KD1, KD2 and KD3 where KD = Kramer Doublets) are listed in **Table 2**, and their orientations are shown in **fig**. **16**. **Table 2** shows the *ab initio* computed ground state *g*-tensors ($g_{xx1,yy1,zz1}$), first excited *g*-tensors ($g_{xx2,yy2,zz2}$) and second excited *g*-tensors ($g_{xx3,yy3,zz3}$) along with the energy separation between ground to first excited state and ground to second excited state (E_{KD1}-E_{KD2} / E_{KD1}-E_{KD3}) for complex **1**. The angle between the ground state to first excited KDs and ground to second excited state for each Dy^{III} centre (A_{KD12}/A_{KD13}).

Table 2 Calculated *ab initio g*, KD energy separations and angles between KD states.

			E_{KD1}-E_{KD2} / E_{KD1}-E_{KD3} (cm^{-1})	**Angle (°) (A_{KD12}/A_{KD13})**
Dy1	g_{xx1}/ g_{xx2}/ g_{xx3}	0.000/0.012/0.921	262.7/511.7	2.0/7.7
	g_{yy1}/ g_{yy2}/ g_{yy3}	0.000/0.020/1.162		
	g_{zz1}/ g_{zz2}/ g_{zz3}	19.879/16.991/12.195		
Dy2	g_{xx1}/ g_{xx2}/ g_{xx3}	0.000/0.015/1.142	262.5/509.8	1.6/6.9
	g_{yy1}/ g_{yy2}/ g_{yy3}	0.000/0.021/1.662		
	g_{zz1}/ g_{zz2}/ g_{zz3}	19.927/17.071/12.646		
Dy3	g_{xx1}/ g_{xx2}/ g_{xx3}	0.000/0.005/0.120	262.5/522.0	1.0/1.9
	g_{yy1}/ g_{yy2}/ g_{yy3}	0.000/0.009/1.055		
	g_{zz1}/ g_{zz2}/ g_{zz3}	19.864/16.991/12.893		

The energy gap between the first-excited state KDs was found to be identical for all three Dy^{III} ions, at 263 cm^{-1}. Since the energy gap is correlated to the crystal-field splitting energy, this suggests strong splitting of the m_J levels in compound **1**.

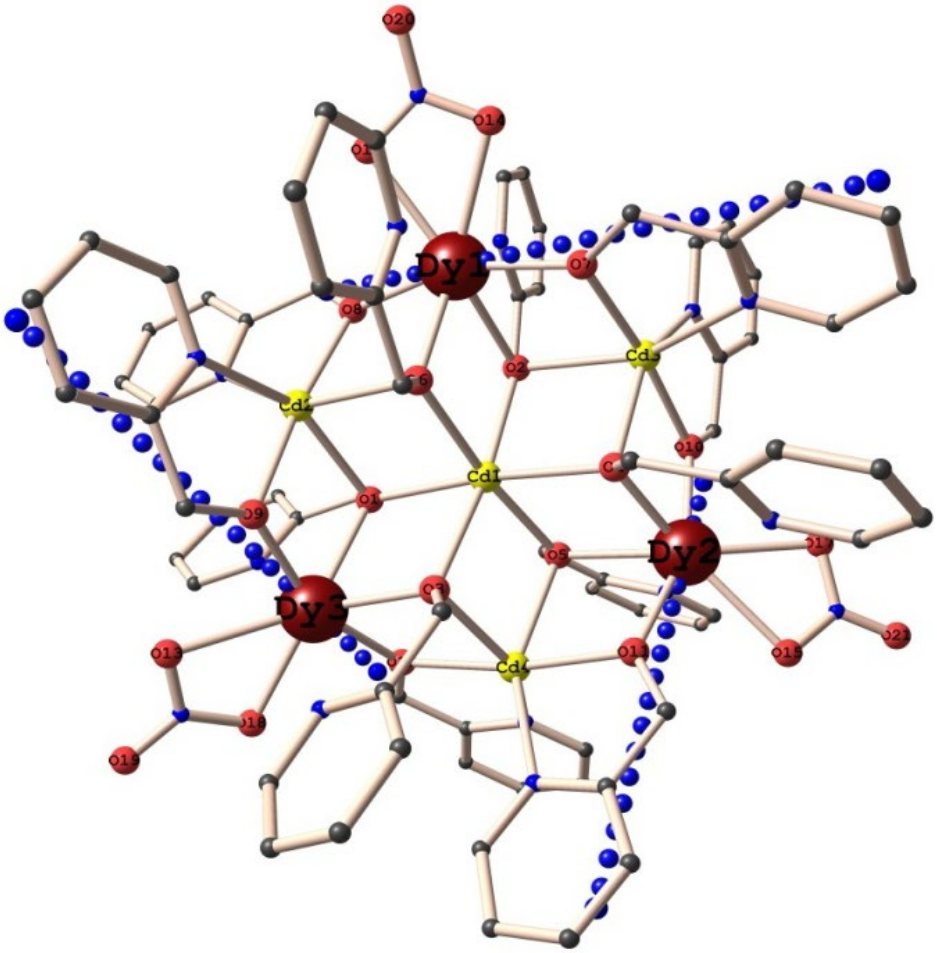

Figure 16 The directions of the local anisotropy axes in the ground Kramers doublet on each paramagnetic metal site (blue dotted line) in **1**.

The g_{zz} axis for all Dy^{III} ions passes along the μ-alkoxo oxygen atom connected to the Cd ion. For all Dy^{III} ions, $m_J = \pm 15/2$ is found to be the ground state and $m_J = \pm 13/2$ is the first excited state (**fig**. **17**). This can be attributed to the stronger axial interactions and weaker transverse interactions. The second excited state for all Dy^{III} ions is transverse in nature, causing relaxation to occur via the second excited state. To determine the various relaxation processes associated with single-ion Dy^{III} anisotropy, the mechanisms of magnetic relaxation were calculated and are shown in **fig**. **18**. The thick black lines indicate the Kramer's doublets as a function of computed magnetic moment. The indigo arrows show the possible pathway via Orbach/Raman relaxation. The dotted red lines represent the presence of QTM/TA-QTM between connecting pairs. The numbers given at each arrow are the mean absolute value for the corresponding matrix element of the transition magnetic moment. The green terms corresponds to the wave function analysis of the m_J levels.

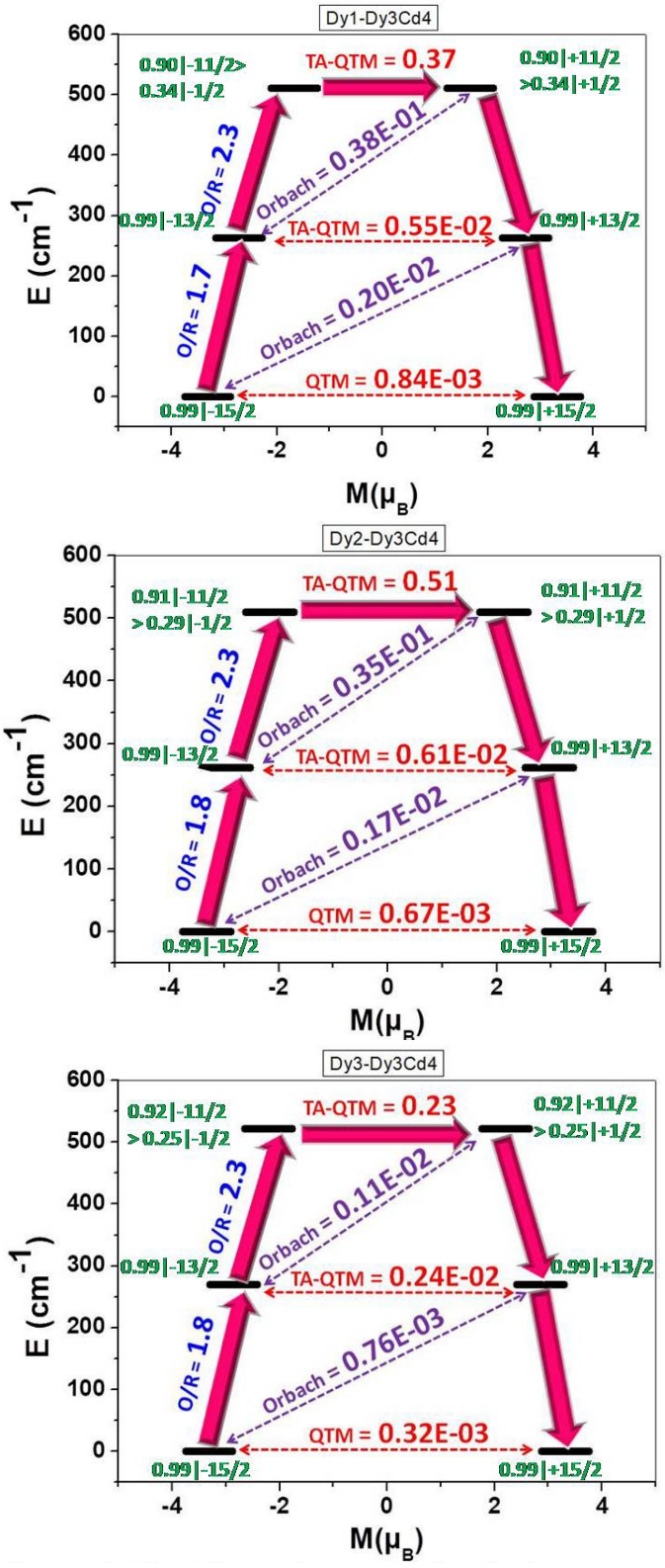

Figure 17 The *ab initio* computed magnetization blocking barrier for the Dy1, Dy2 and Dy3 ions of complex **1**. The x-axis indicates the magnetic moment of each state along main magnetic axis of the Dy ions, while the y-axis denotes the energy of the respective states.

For single ions, wavefunction mixing for the second excited state (±11/2 and ±1/2) is found to be smaller for the Dy3 ions, followed by the Dy2 ions, with maximum mixing found for Dy1. Investigation beyond a single-ion mechanism was undertaken, incorporating Dy^{III}-Dy^{III} exchange interactions as these have shown to quench the observed QTM.

4.4.2 Mechanism of Magnetic Relaxation (Polynuclear Paradigm)

To gain insights into the mechanism(s) of relaxation, a comprehensive model must be developed, incorporating the exchange coupling between the paramagnetic centres. This has been performed using the POLY_ANISO program which employs the Lines model to fit the experimental data using the *ab initio* computed parameters of the Dy^{III} single ions. The best fit obtained using POLY_ANISO for complex **1** is found to be in good agreement with the experimental data (**fig**. **18**).

For complex **1**, the magnetic interaction between Dy^{III} ions (J_{total}) is found to be anti-ferromagnetic in nature. The total exchange interaction was calculated to be J_{total} = -0.13 cm^{-1} ($J_{total} = J_{exc}$ = -0.01 cm^{-1} + $J_{dipolar}$ = -0.12 cm^{-1}, where J_{exc} is the superexchange interaction and $J_{dipolar}$ is the through-space dipolar interaction). This shows that the exchange interaction is essentially dipolar in nature.

(a)

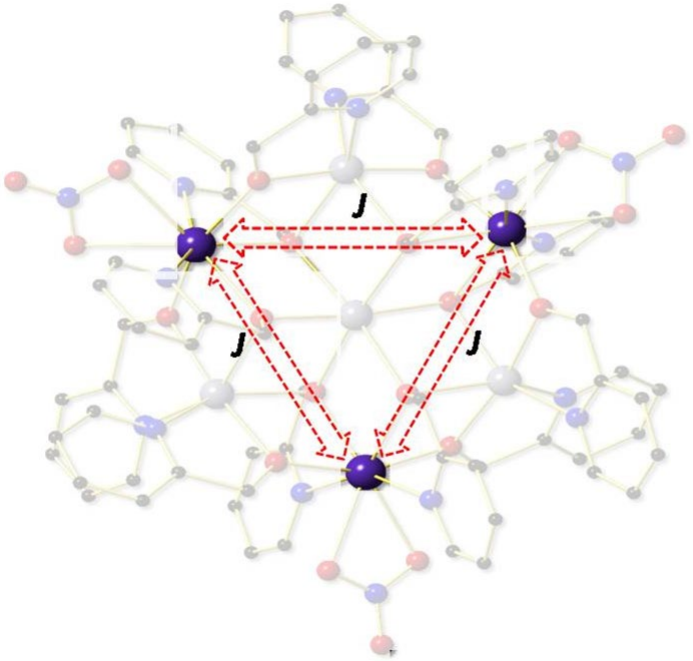

(b)

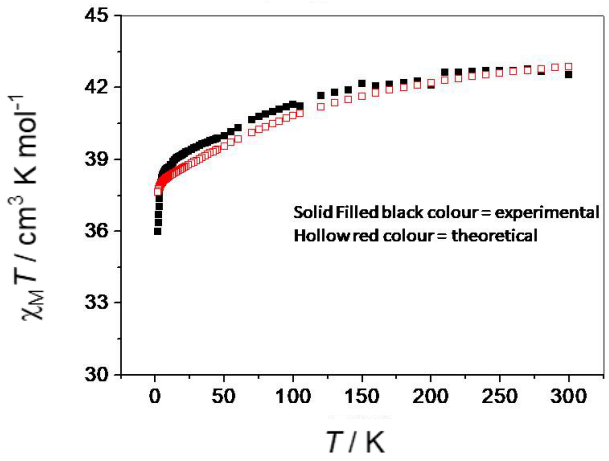

(c)

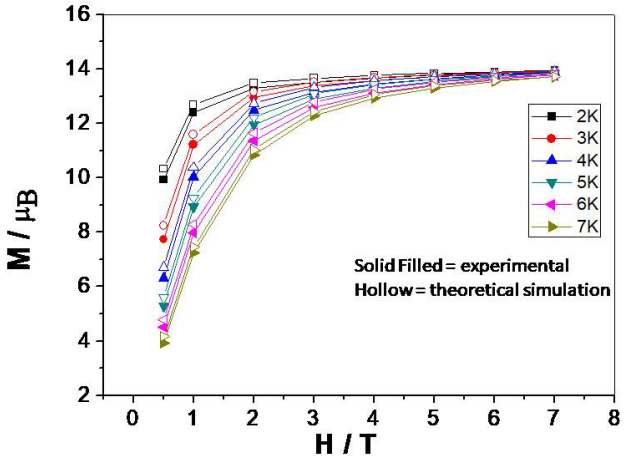

Figure 18 (a) Magnetic exchange coupling in complex **1**. (b) Best fit for $\chi_M T$ vs T obtained using POLY_ANISO for complex **1**. (c) Best fit for M vs H obtained using POLY_ANISO for complex **1**.

The tunnelling parameters (Δ_{tun}) for exchanged coupled states below 262.7 cm^{-1} was calculated to be very small ($\leqslant$ $6.7x10^{-8}$ cm^{-1}, see **fig**. **19**) whereas the tunnelling (Δ_{tun}) parameters for exchange coupled states at 510.3 cm^{-1} is computed to be large enough to cause relaxation via this state ($\leqslant$ $2.2x10^{-5}$ cm^{-1}, see **fig**. **19**). The numbers provided are the mean absolute value for the corresponding matrix element of the transition magnetic moment. The thick black line indicates the Kramer's doublets as a function of computed magnetic moment. The indigo colour shows the possible pathway via Orbach/Raman relaxation. The dotted red lines represent the presence of QTM/TA-QTM between the connecting pairs. The thick pink coloured arrow shows the relaxation pathway.

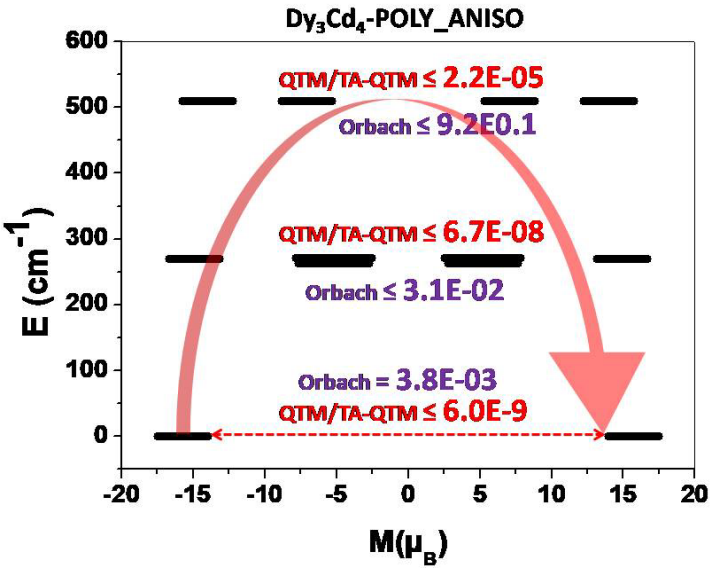

Figure 19 The *ab initio* POLY_ANISO computed magnetization blocking barrier for complex **1**. The x-axis indicates the magnetic moment of each state along the main magnetic axis of the Dy ions, while the y-axis denotes the energy of the respective states.

The experimental data for **1** shows a barrier height of 295.866 ± 8.436 cm^{-1} (U_{eff}). The theoretical data therefore indicates that the experimental U_{eff} value is between the first and second excited state. This deviation in the experimental and theoretically estimated barrier heights is due to additional factors such as intermolecular interactions and hyperfine coupling of the metal ions/nitrogen atoms in the coordination sphere of each Dy^{III} ion, that likely contribute to the overall relaxation process. Discussion of the overall relaxation process and how it is affected by other structural factors is herein restricted to comparison of Arrhenius data between the undiluted and diluted systems.

4.5 Conclusion

The heptanuclear disc-like [Cd_4Dy_3] (**1**) complex was synthesised, along with site-diluted [Cd_4Dy_2Y] (**2**) and [Cd_4DyY_2] (**3**) and diamagnetic [Cd_4Y_3] (**4**). All were characterised using single-crystal X-ray diffraction. The solution stability and ratio of ions within these diluted systems were determined using Mass Spectrometry. These species possess both intramolecular and intermolecular triangles in their extended structures, reminiscent of a kagomé lattice, which may lead to spin-frustration effects. The best fit of the magnetic susceptibility and magnetisation data using POLY_ANISO found that the total exchange interaction between each paramagnetic Dy^{III} ion, J_{total} = -0.13 cm^{-1} where the predominant interaction is dipolar in nature, $J_{dipolar}$ = -0.12 cm^{-1}. Ac susceptibility data measurements for **1**-**3** revealed slow relaxation of the magnetization with U_{eff} = 295.866 cm^{-1}, 302.22 cm^{-1} and 291.079 cm^{-1}, respectively. *Ab initio* computational analysis revealed that the first and second excited states were located approximately 262.7 cm^{-1} and 510 cm^{-1} above the ground state. The experimental U_{eff} values are an intermediate between those values suggesting that both of these excited states are involved in the relaxation process. Hysteresis loop measurements confirmed that **3** had the greatest retention of magnetisation which coincides with the ac susceptibility data. The effect of QTM as seen in the Arhennius plots from the intramolecular triangle being present in **1** to not being present in **2** and **3** shows spin frustration effects but further *ab initio* computational analysis needs to undertaken to clarify this.

4.6 References

1. E. Loukopoulos, B. Berkoff, A. Abdul-Sada, G. J. Tizzard, S. J. Coles, A. Escuer and G. E. Kostakis, *Eur. J. Inorg. Chem.*, 2015, **2015**, 2646-2649.
2. J. W. Sharples, D. Collison, E. J. McInnes, J. Schnack, E. Palacios and M. Evangelisti, *Nature Comm.*, 2014, **5**, 5321.
3. J. Goura, J. P. Walsh, F. Tuna and V. Chandrasekhar, *Dalton Trans.*, 2015, **44**, 1142-1149.
4. J. W. Sharples, Y. Z. Zheng, F. Tuna, E. J. McInnes and D. Collison, *Chemical Comm.*, 2011, **47**, 7650-7652.
5. J. Liu, C. Ma, H. Chen, M. Hu, H. Wen, H. Cui and C. Chen, *Dalton Trans.*, 2013, **42**, 3787-3790.
6. B. Berkoff, K. Griffiths, A. Abdul-Sada, G. J. Tizzard, S. J. Coles, A. Escuer and G. E. Kostakis, *Dalton Trans.*, 2015, **44**, 12788-12795.
7. E. Moreno Pineda, N. F. Chilton, R. Marx, M. Dorfel, D. O. Sells, P. Neugebauer, S. D. Jiang, D. Collison, J. van Slageren, E. J. McInnes and R. E. Winpenny, *Nature Comm.*, 2014, **5**, 5243.
8. F. S. Guo, B. M. Day, Y. C. Chen, M. L. Tong, A. Mansikkamaki and R. A. Layfield, *Angew. Chem. Int. Ed.*, 2017, **56**, 11445-11449.
9. Y.-S. Ding, N. F. Chilton, R. E. P. Winpenny and Y.-Z. Zheng, *Angew. Chem. Int. Ed.*, 2016, **55**, 16071-16074.
10. E. M. Pineda, N. F. Chilton, F. Tuna, R. E. P. Winpenny and E. J. L. McInnes, *Inorg. Chem.*, 2015, **54**, 5930-5941.
11. S. Hill, S. Datta, J. Liu, R. Inglis, C. J. Milios, P. L. Feng, J. J. Henderson, E. del Barco, E. K. Brechin and D. N. Hendrickson, *Dalton Trans.*, 2010, **39**, 4693-4707.
12. Y. Li, Q. Shang, Y. Q. Zhang, E. C. Yang and X. J. Zhao, *Chem. Euro. J*, 2016, **22**, 18840-18849.
13. J. Tang, I. Hewitt, N. T. Madhu, G. Chastanet, W. Wernsdorfer, C. E. Anson, C. Benelli, R. Sessoli and A. K. Powell, *Angew. Chem. Int. Ed.*, 2006, **45**, 1729-1733.
14. L. F. Chibotaru, L. Ungur and A. Soncini, *Angew. Chem. Int. Ed.*, 2008, **47**, 4126-4129.
15. I. J. Hewitt, J. Tang, N. T. Madhu, C. E. Anson, Y. Lan, J. Luzon, M. Etienne, R. Sessoli and A. K. Powell, *Angew. Chem. Int. Ed.*, 2010, **49**, 6352-6356.
16. Z. Salman, S. R. Giblin, Y. Lan, A. K. Powell, R. Scheuermann, R. Tingle and R. Sessoli, *Phys. Rev.*, 2010, **82**, 174427-174431.
17. S. Y. Lin, L. Zhao, Y. N. Guo, P. Zhang, Y. Guo and J. Tang, *Inorg. Chem.*, 2012, **51**, 10522-10528.
18. X. L. Li, H. Li, D. M. Chen, C. Wang, J. Wu, J. Tang, W. Shi and P. Cheng, *Dalton Trans.*, 2015, **44**, 20316-20320.
19. I. F. Diaz-Ortega, J. M. Herrera, T. Gupta, G. Rajaraman, H. Nojiri and E. Colacio, *Inorg. Chem.*, 2017, **56**, 5594-5610.
20. K. R. Vignesh, S. K. Langley, A. Swain, B. Moubaraki, M. Damjanovic, W. Wernsdorfer, G. Rajaraman and K. S. Murray, *Angew. Chem. Int. Ed. Engl.*, 2018, **57**, 779-784.
21. R. Grindell, V. Vieru, T. Pugh, L. F. Chibotaru and R. A. Layfield, *Dalton Trans.*, 2016, **45**, 16556-16560.
22. J. Schnack, *Dalton Trans.*, 2010, **39**, 4677-4686.
23. P. Kogerler, B. Tsukerblat and A. Muller, *Dalton Trans.*, 2010, **1**, 21-36.
24. A.P.Ramirez, *Annu. Rev. Mater. Sci.*, 1994, **24**, 453-480.
25. H. Wang, K. Qian, K. Wang, Y. Bian, J. Jiang and S. Gao, *Chem. Comm.*, 2011, **47**, 9624-9626.

26. K. Katoh, Y. Horii, N. Yasuda, W. Wernsdorfer, K. Toriumi, B. K. Breedlove and M. Yamashita, *Dalton Trans.*, 2012, **41**, 13582-13600.
27. H. Shang, S. Zeng, H. Wang, J. Dou and J. Jiang, *Sci. Rep.*, 2015, **5**, 8838-8843.
28. S. Titos-Padilla, J. Ruiz, J. M. Herrera, E. K. Brechin, W. Wersndorfer, F. Lloret and E. Colacio, *Inorg. Chem.*, 2013, **52**, 9620-9626.
29. J. Ruiz, A. J. Mota, A. Rodríguez-Diéguez, S. Titos, J. M. Herrera, E. Ruiz, E. Cremades, J. P. Costes and E. Colacio, *Chem. Comm.*, 2012, **48**, 7916-7918.
30. E. Colacio, J. Ruiz, E. Ruiz, E. Cremades, J. Krzystek, S. Carretta, J. Cano, T. Guidi, W. Wernsdorfer and E. K. Brechin, *Angew. Chem. Int. Ed.*, 2013, **52**, 9130-9134.
31. A. Chakraborty, J. Goura, P. Kalita, A. Swain, G. Rajaraman and V. Chandrasekhar, *Dalton Trans.*, 2018, **47**, 8841-8864.
32. G. Cosquer, F. Pointillart, S. Golhen, O. Cador and L. Ouahab, *Chem. Euro. J.*, 2013, **19**, 7895-7903.
33. J. Li, Y. Han, F. Cao, R. M. Wei, Y. Q. Zhang and Y. Song, *Dalton Trans.*, 2016, **45**, 9279-9284.
34. M. Jeletic, P. H. Lin, J. J. Le Roy, I. Korobkov, S. I. Gorelsky and M. Murugesu, *J. Am. Chem. Soc.*, 2011, **133**, 19286-19289.
35. J. Miklovic, D. Valigura, R. Boca and J. Titis, *Dalton Trans.*, 2015, **44**, 12484-12487.
36. R. J. Blagg, L. Ungur, F. Tuna, J. Speak, P. Comar, D. Collison, W. Wernsdorfer, E. J. McInnes, L. F. Chibotaru and R. E. Winpenny, *Nature Chem.*, 2013, **5**, 673-678.
37. S. K. Langley, N. F. Chilton, B. Moubaraki and K. S. Murray, *Inorg. Chem.*, 2013, **52**, 7183-7192.
38. A. V. Funes, L. Carrella, E. Rentschler and P. Albores, *Dalton Trans.*, 2014, **43**, 2361-2364.
39. L. T. A. Ho and L. F. Chibotaru, *Phys. Rev. B*, 2016, **94**, 104422-104426.
40. G. M. Sheldrick, *Acta Crys. A*, 2008, **64**, 112-122.
41. O. V. Dolomanov, L. J. Bourhis, R. J. Gildea, J. A. K. Howard and H. Puschmann, *J. App. Crys.*, 2009, **42**, 339-341.
42. M. Llunell, D. Casanova, J. Cirera, P. Alemany and S. Alvarez, *SHAPE, Version 2.0*, 2010.

4.7 Supplementary Information

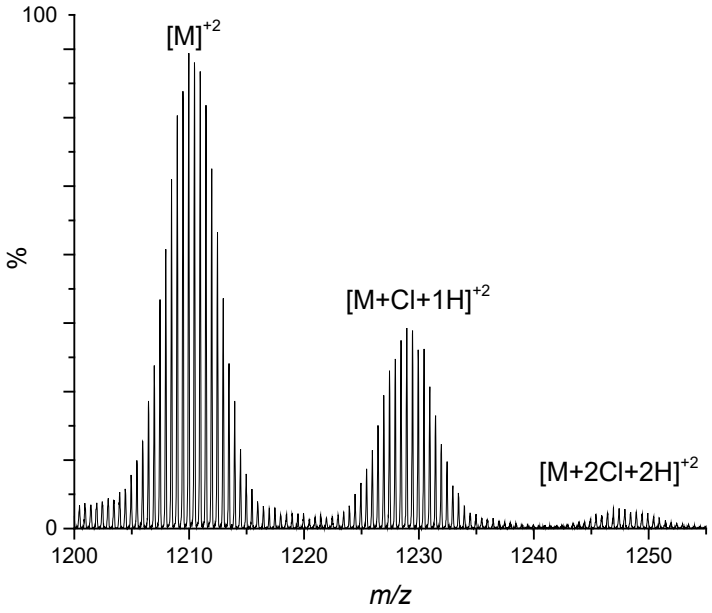

Figure S1 Partial mass spectrum of **1** showing isotopic distributions of $[\mathbf{1}]^{+2}$, $[\mathbf{1} + Cl + H]^{+2}$ and $[\mathbf{1} + 2Cl + 2H]^{+2}$.

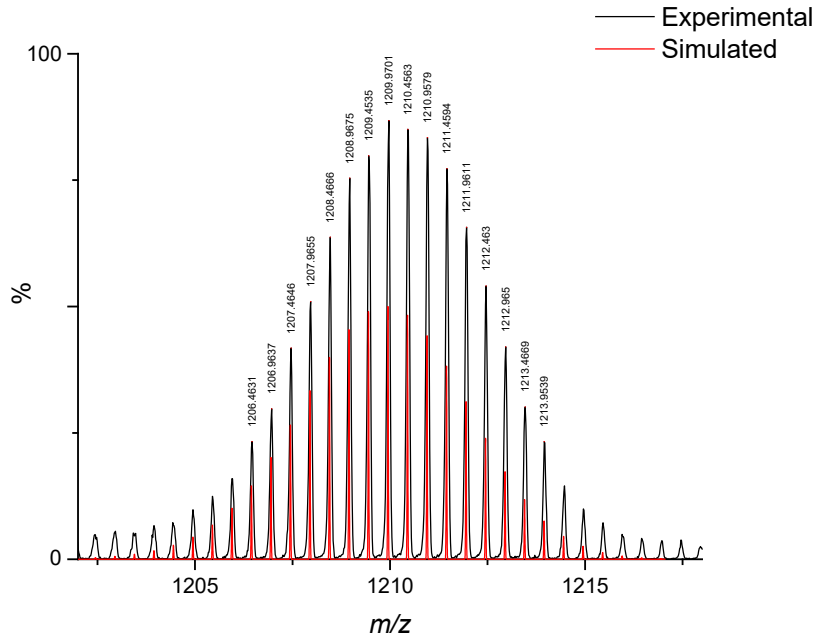

Figure S2 Partial mass spectrum of **1** showing isotopic distributions of $[\mathbf{1}]^{+2}$.

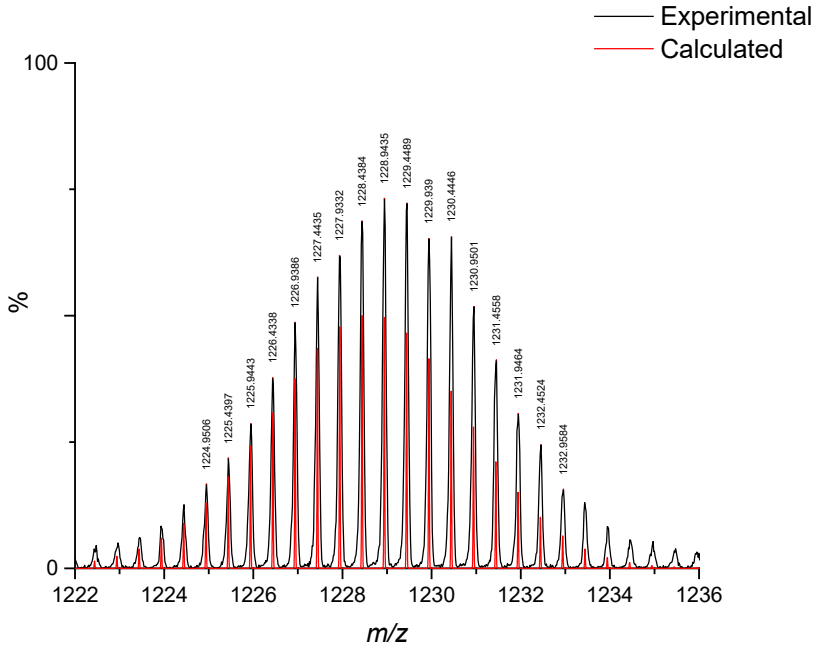

Figure S3 Partial mass spectrum of 1 showing isotopic distributions of [**1** + Cl + H]$^{+2}$.

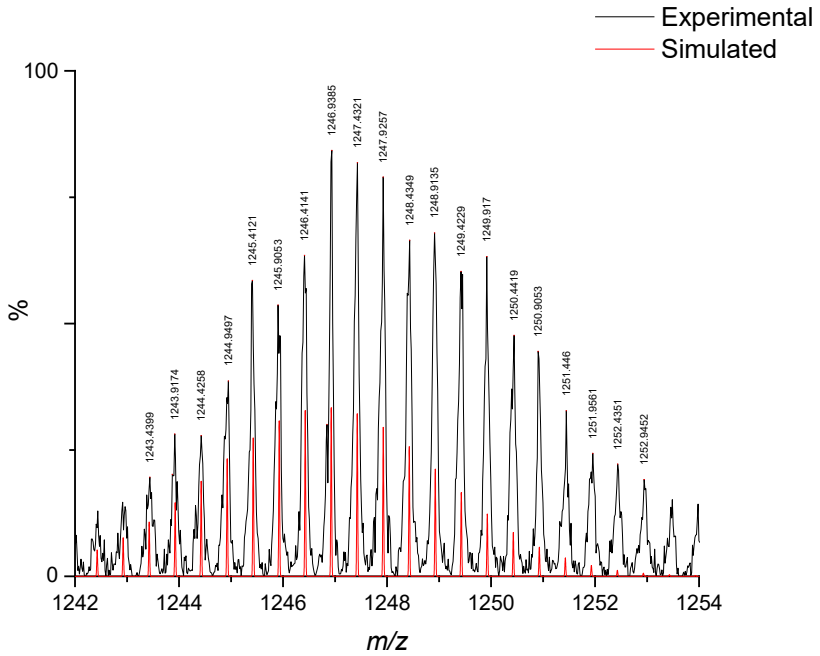

Figure S4 Partial mass spectrum of 1 showing isotopic distributions of [**1** + 2Cl + 2H]$^{+2}$.

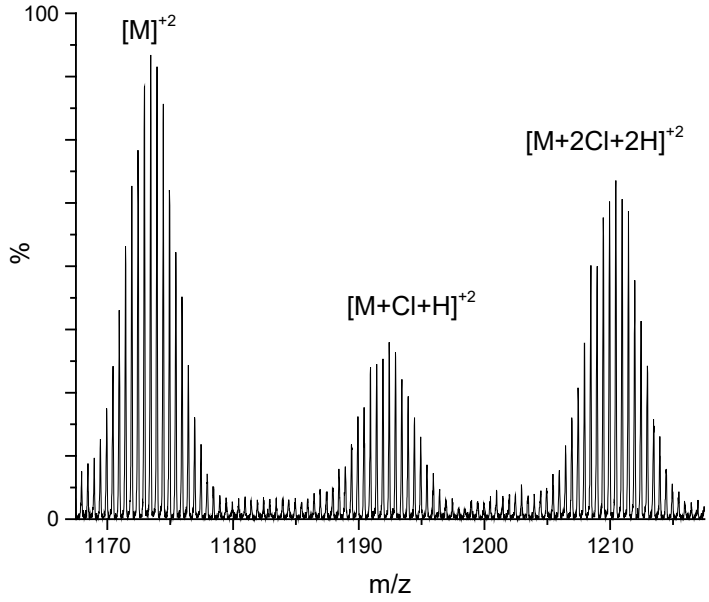

Figure S5 Partial mass spectrum of **2** showing isotopic distributions of [**2**]$^{+2}$, [**2** + Cl + H]$^{+2}$ and [**2** + 2Cl + 2H]$^{+2}$.

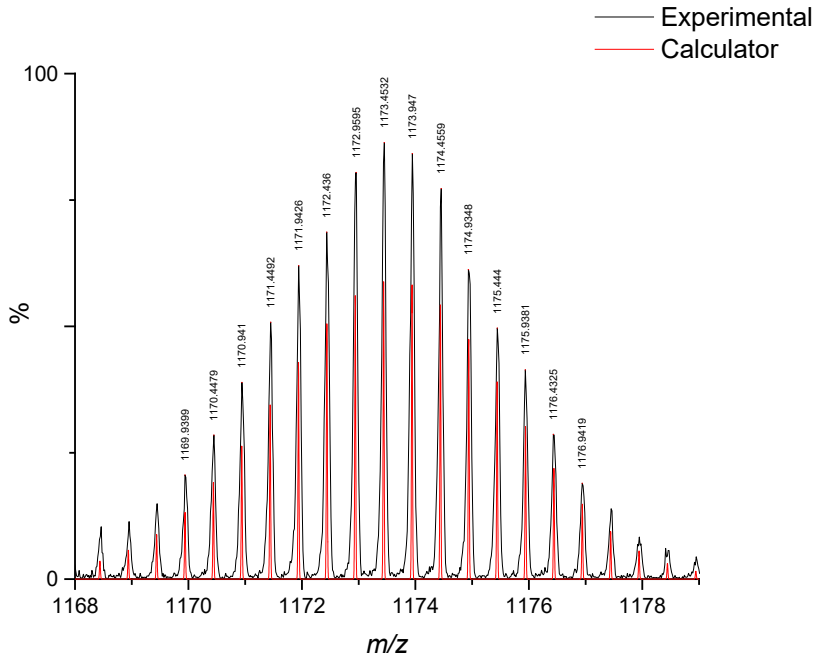

Figure S6 Partial mass spectrum of **2** showing isotopic distributions of [**2**]$^{+2}$.

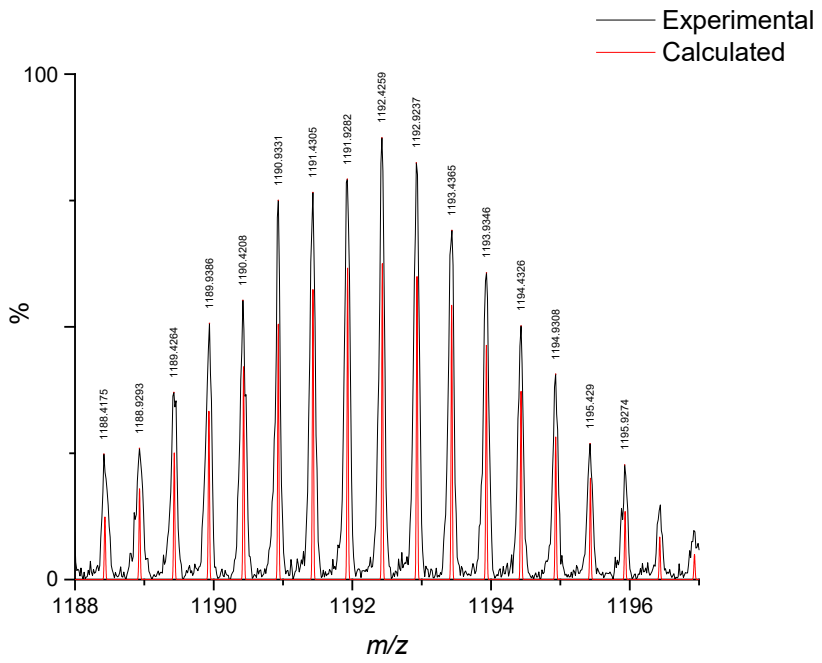

Figure S7 Partial mass spectrum of **2** showing isotopic distributions of [**2** + Cl + H]$^{+2}$.

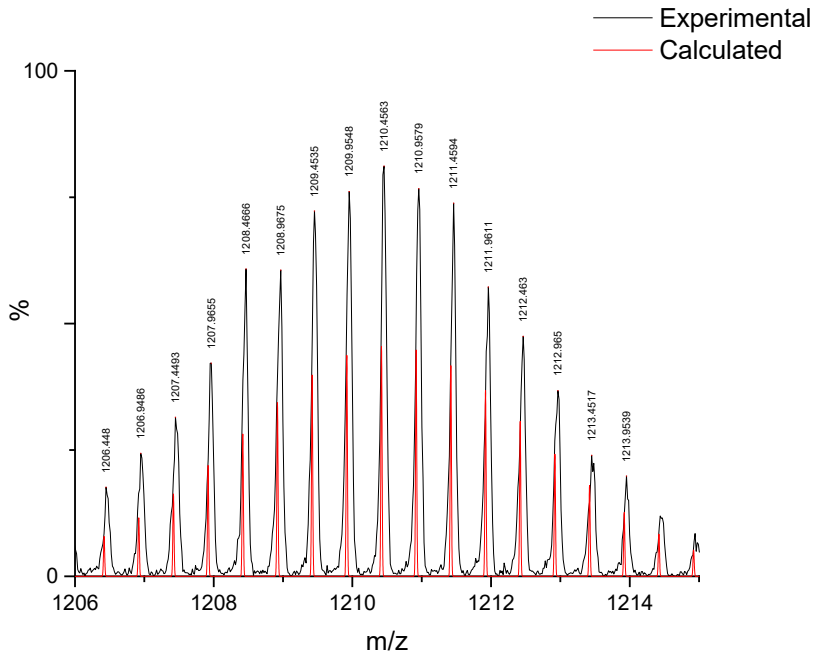

Figure S8 Partial mass spectrum of **2** showing isotopic distributions of [**2** + 2Cl + 2H]$^{+2}$.

	2	3
% abundance	78.9	21.1

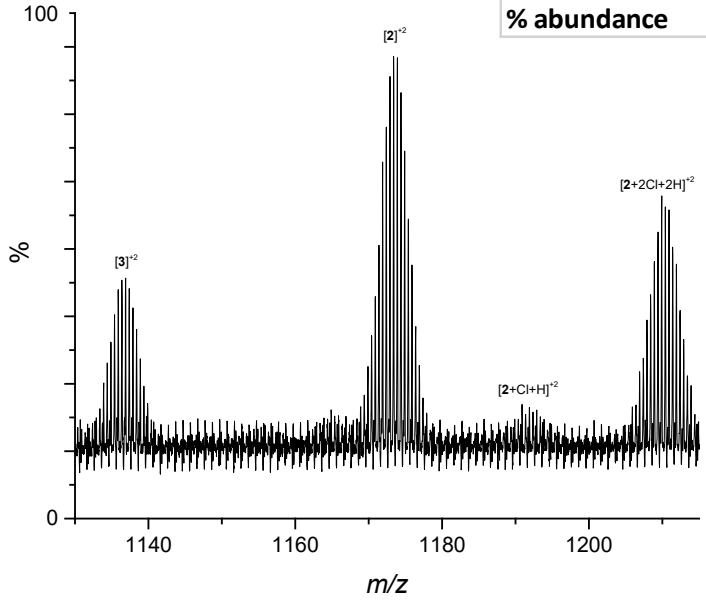

Figure S9 Partial mass spectrum of **2** showing isotopic distributions of the mixture of species with a table showing % abundance (based on total intensity of the different components of each species).

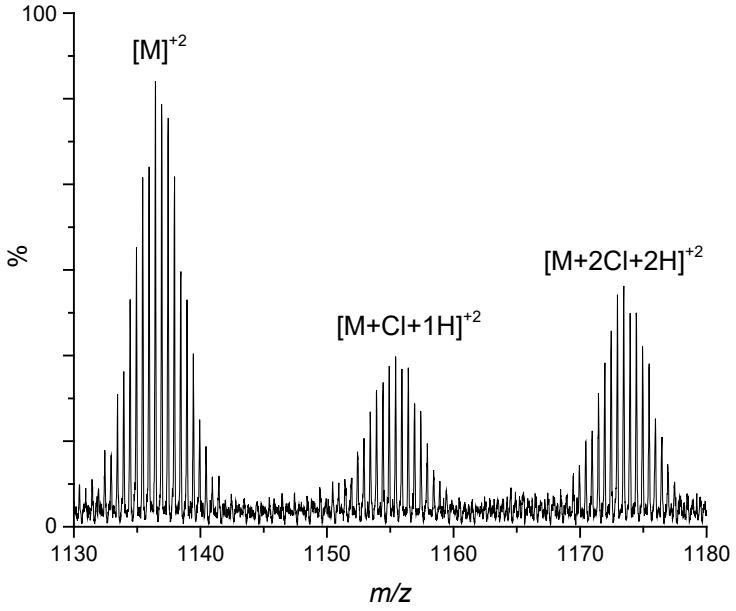

Figure S10 Partial mass spectrum of **3** showing isotopic distributions of [**3**]$^{+2}$, [**3** + Cl + H]$^{+2}$ and [**3** + 2Cl + 2H]$^{+2}$.

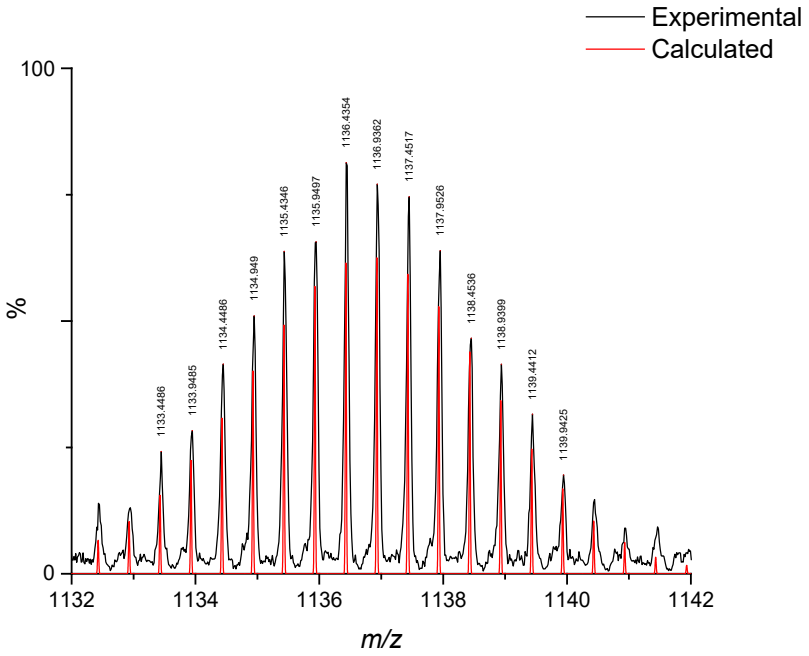

Figure S11 Partial mass spectrum of **3** showing isotopic distributions of [**3**]$^{+2}$.

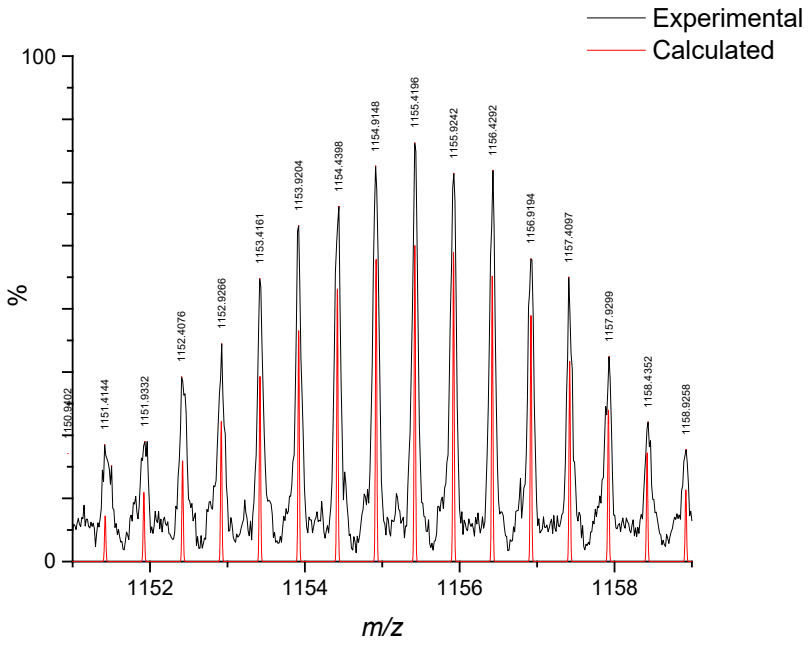

Figure S12 Partial mass spectrum of **3** showing isotopic distributions of [**3** + Cl + H]$^{+2}$.

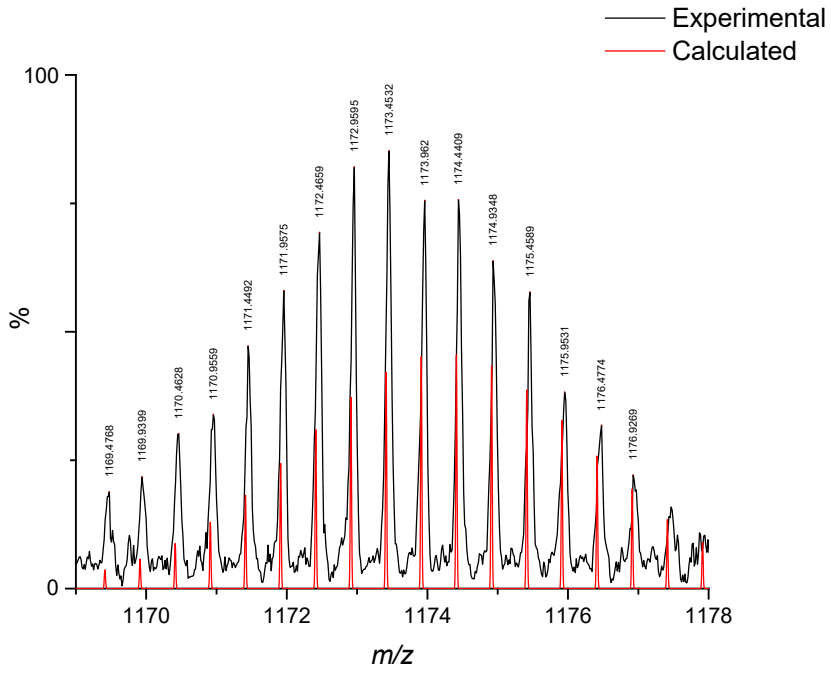

Figure S13 Partial mass spectrum of **3** showing isotopic distributions of [**3** + 2Cl + 2H]$^{+2}$.

	2	3	4
% abundance	12.55	58.79	28.65

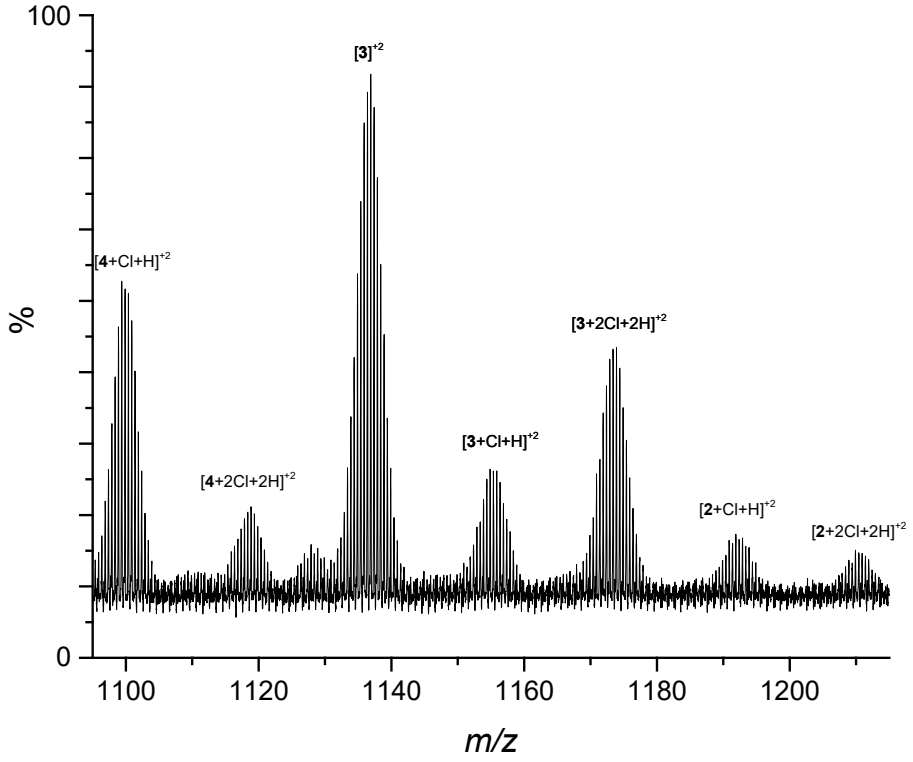

Figure S14 Partial mass spectrum of **3** showing isotopic distributions of the mixture of species with a table showing % abundance (based on total intensity of the different components of each species).

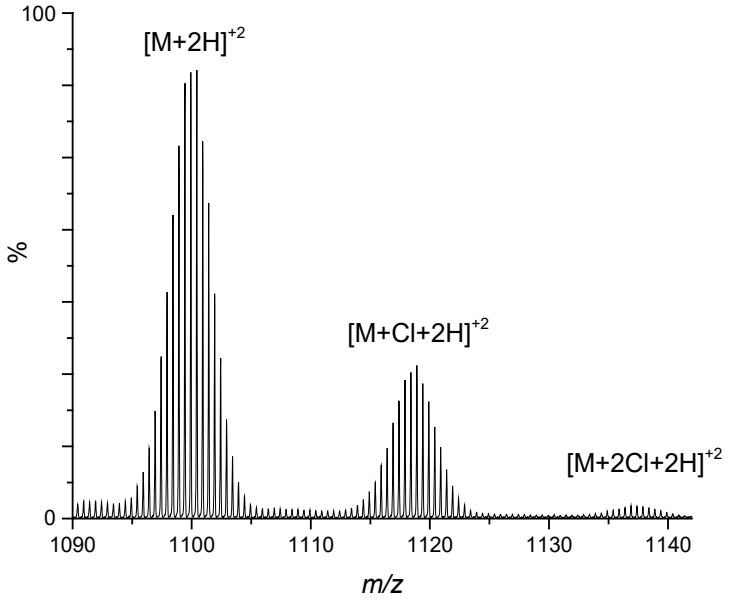

Figure S15 Partial mass spectrum of **2** showing isotopic distributions of $[\mathbf{4}]^{+2}$, $[\mathbf{4} + Cl + H]^{+2}$ and $[\mathbf{4} + 2Cl + 2H]^{+2}$.

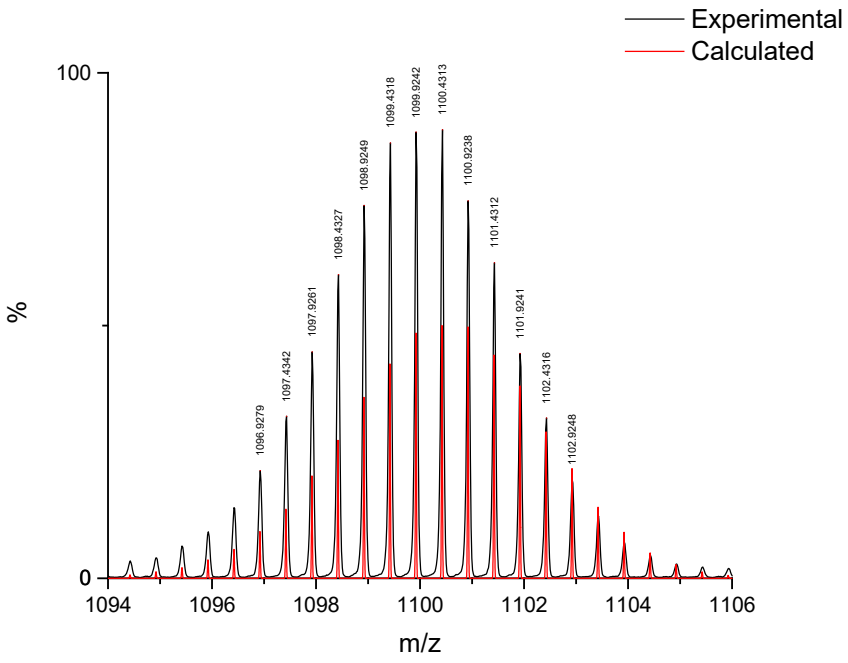

Figure S16 Partial mass spectrum of **4** showing isotopic distributions of $[\mathbf{4}]^{+2}$.

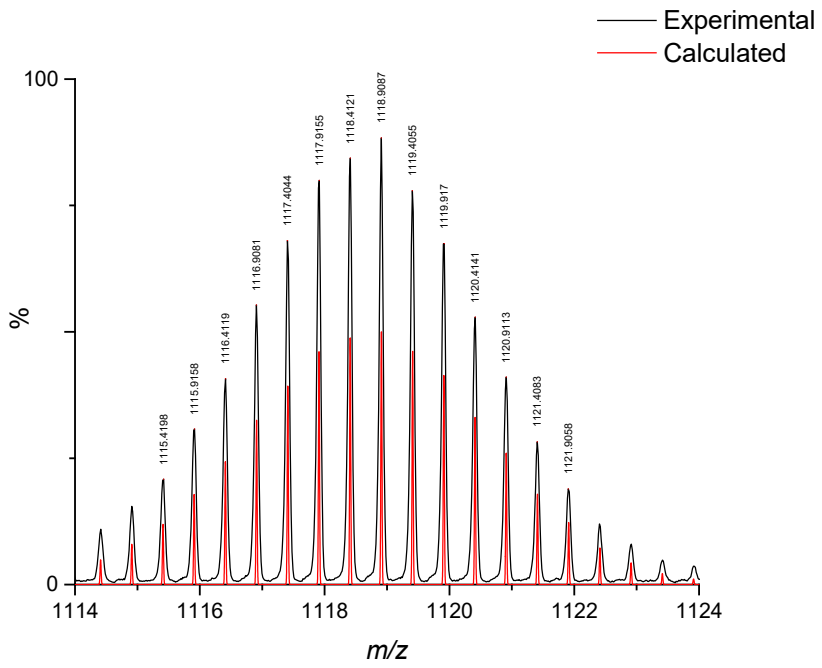

Figure S17 Partial mass spectrum of **4** showing isotopic distributions of [**4** + Cl + H]$^{+2}$.

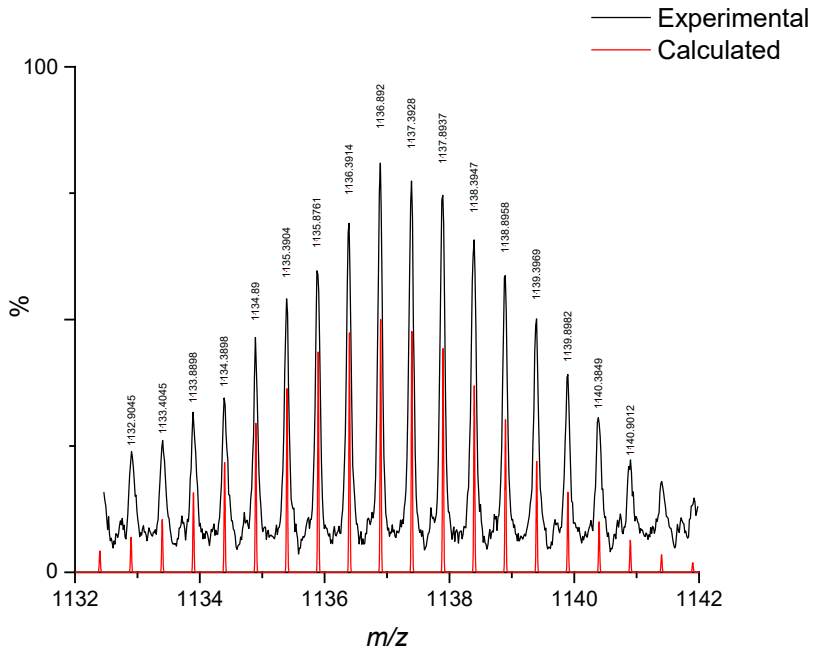

Figure S18 Partial mass spectrum of **4** showing isotopic distributions of [**4** + 2Cl + 2H]$^{+2}$.

Table S1 Alpha (α) values of Cole-Cole fits of **1** at zero-field

	***T* / K**				
	14	**16**	**18**	**20**	**22**
χ_S	0.26373	0.35482	0.42283	0.40891	0.38226
error	0.03065	0.0225	0.01633	0.0121	0.01048
χ_T	8.26716	6.88438	5.73171	5.14579	4.67495
error	0.11944	0.07876	0.02109	0.01225	0.00864
α	0.21999	0.1788	0.12028	0.09967	0.08786
error	0.00684	0.00776	0.00807	0.00649	0.00582

Table S2 Alpha (α) values of Cole-Cole fits of **2** at zero-field

	***T*/ K**						
	18	**20**	**22**	**24**	**26**	**28**	**30**
χ_S	0.34223	0.36771	0.34658	0.33494	0.31733	0.29818	0.29343
error	0.0084	0.00638	0.00797	0.0052	0.00632	0.00754	0.01764
χ_T	3.20142	2.72075	2.47961	2.26849	2.09829	1.95303	1.83221
error	0.02964	0.00717	0.00752	0.00339	0.00289	0.00242	0.00404
α	0.17489	0.11054	0.09514	0.08026	0.07126	0.06698	0.06928
error	0.00732	0.00723	0.00957	0.00597	0.00653	0.00679	0.01346

Table S3 Alpha (α) values of Cole-Cole fits of **3** at zero-field

	***T* / K**					
	20	**22**	**24**	**26**	**28**	**30**
χ_S	0.42483	0.40813	0.38773	0.35996	0.34679	0.31257
error	0.00283	0.00266	0.00258	0.00375	0.00343	0.00481
χ_T	1.37163	1.20132	1.10188	1.02053	0.95093	0.88925
error	0.01107	0.00221	0.00154	0.0017	0.000908298	0.000767853
α	0.19257	0.12347	0.10116	0.1056	0.07996	0.09273
error	0.01031	0.00888	0.00858	0.01157	0.00904	0.00995

Table S4 Alpha (α) values of Cole-Cole fits of **1** at 0.1 T.

	***T* / K**			
	12	**14**	**16**	**18**
χ_S	0.99286	0.81891	0.69378	0.57836
error	0.0154	0.01063	0.00702	0.00672
χ_T	6.75	6	5.15	4.6
error	-	-	-	-
α	0.10533	0.12173	0.11476	0.12754
error	0.00016815	0.000178006	0.000145567	0.00527

Table S5 Alpha (α) values of Cole-Cole fits of **2** at 0.1 T

	***T* / K**			
	12	**14**	**16**	**18**
χ_S	0.21033	0.17617	0.06962	0.08836
error	0.01065	0.00952	0.00736	0.00365
χ_T	6.53316	5.79533	5.13977	4.52723
error	0.12688	0.05746	0.02049	0.0073
α	0.0949	0.1016	0.12959	0.10524
error	0.00192	0.00106	0.00531	0.00305

Table S6 Alpha (α) values of Cole-Cole fits of **1** at 0.1 T

	***T* / K**
	16
χ_S	0.22918
error	0.00457
χ_T	2.91597
error	0.00772
α	0.11084
error	0.00482

Chapter 5: Conclusions and Future Outlook

The aim of this thesis was to synthesise 3*d*/4*d*-4*f* heterometallic complexes that can retain their magnetisation and understand how this behaviour is correlated with their structure.

In **Chapter 2**, synthesis and magnetic characterisation of the three-fold symmetric triangle-in-triangle complex $[Ni^{II}_3Ln^{III}_3(hmp)_{12}](ClO_4)_3$ (Ln = Gd, Tb, Dy, Ho, Er,, Y; hmpH = 2-(hydroxymethyl)pyridine) revealed that the $[Ni_3Tb_3]$ analogue showed tails in the out-of-phase ac susceptibility (χ_M'') data. This indicates that there is a small degree of retention of magnetisation. Fitting of the $[Ni_3Gd_3]$ analogue showed a J_{GdGd} = -0.02 cm^{-1} and J_{GdNi} = -0.32 cm^{-1}, it was hypothesised that within this structure type, these weak interactions resulted in a decrease in retention of magnetisation compared to complexes with the same topology in the literature. However, there is literature precedent to also hypothesise that any magnetic exchange interaction can result in a decrease in their ability to retain their magnetisation due to an increase in additional relaxation pathways such as QTM and TA-QTM. Computational analysis must be undertaken to clarify the role of these parameters in the resulting magnetic behaviour.

Chapter 3 showed the synthesis and magnetic characterisation of the butterfly complexes $[M^{II}_2Ln^{III}_2(hmp)_6(NO_3)_4]\cdot MeOH$ (*BF1*) and $[M^{II}_2Ln^{III}_2(mhmp)_6(NO_3)_4]\cdot MeCN$ (*BF2*) (where M = Ni, Zn; Ln = Gd, Tb, Dy, Y; mhmpH = 6-methyl-2-(hydroxymethyl)pyridine). Fitting of the magnetic susceptibility data collected for the $[Ni_2Gd_2]$ and $[Ni_2Y_2]$ analogues of *BF1* revealed best fit parameters: J_{NiNi} = 1.09 cm^{-1} and J_{GdNi} = 0.7325 cm^{-1}. Analogous measurements for the $[Ni_2Gd_2]$ and $[Ni_2Y_2]$ analogues of *BF2* revealed best fit parameters: J_{NiNi} = -0.32 cm^{-1} and J_{GdNi} = 0.52 cm^{-1}. The $[Zn_2Dy_2]$ analogues of both *BF1* and *BF2* displayed frequency dependent peaks in χ_M'' measurements indicating slow relaxation of magnetisation with U_{eff} = 38.58 cm^{-1} and 72.45 cm^{-1}, respectively. The larger U_{eff} in *BF2* could be a result improved SIM behaviour paired with a weaker J_{LnNi} value. The $[Ni_2Dy_2]$ analogue of *BF2* (**9**) also exhibits frequency dependent behaviour in ac susceptibility measurements with a U_{eff} = 11.957 cm^{-1}, whereas the $[Ni_2Dy_2]$ analogue of *BF1* did not. These results show that the M-Ln exchange interactions either decrease the complexes ability to retain its magnetisation as shown in *BF2* or completely prevent it as shown in *BF1*. Therefore based on this data, to improve the retention of magnetisation the exchange interactions must be reduced.

Chapter 4 showed synthesis and magnetic characterisation of the heptanuclear disc-like $[Cd^{II}_4(Dy^{III}_{(3-n)}Y^{III}_n)(hmp)_{12}(NO_3)_3](ClO_4)_2\cdot 3MeCN$ (where n = 0, 1, 2 or 3) complexes. The Cd^{II} ions act as a diamagnetic spacer between the Dy^{III} ions in order to reduce the J_{DyDy} value.The

best fit of the magnetic susceptibility and magnetisation data using POLY_ANISO found that the total exchange interaction between each paramagnetic Dy^{III} ion, J_{total} = -0.13 cm^{-1} where the predominant interaction is dipolar in nature, $J_{dipolar}$ = -0.12 cm^{-1}. Ac susceptibility data measurements for [Cd_4Dy_3], [Cd_4Dy_2Y] and [Cd_4DyY_2] revealed slow relaxation of the magnetization with U_{eff} = 295.866 cm^{-1}, 302.22 cm^{-1} and 291.079 cm^{-1}, respectively. Hysteresis measurements showed that upon decreasing the number of Dy centres, therefore decreasing the number of possible exchange interactions, there is an increase in the retention of magnetisation. This proves that that the J_{GdGd} exchange interactions increase the degree of ground state QTM and therefore weaken the retention of magnetisation. *Ab initio* computational analysis revealed that the first and second excited states were located approximately 262.7 cm^{-1} and 510 cm^{-1} above the ground state, the experimental values are an intermediate between these values. This suggests that both excited states are involved in the relaxation process. The presence of the triangular motif in [Cd_4Dy_3] and the change in QTM rate when this is removed in [Cd_4Dy_2Y] and [Cd_4DyY_2] illustrates that spin frustration effects are present. Further *ab initio* computational analysis could give clarity to the nature of this.

The ability for a 3*d*/4*d*-4*f* heterometallic molecular system to retain its magnetisation has shown to be improved by tuning or removing 3*d*/4*d*-4*f* exchange interactions. These interactions are complex owing to the additional parameters introduced by the presence of the 4*f* ions but can be fitted using isotropic and diamagnetic analogues of the system. Overall these results show that in order to maximise the retention of magnetisation of systems containing 4*f* ions the 4*f* ion must be treated as a single ion. Therefore, the local crystal field parameters of the 4*f* ions must be of prime focus by controlling the geometry, ligand sphere and all exchange interactions must be reduced.